Spring 1-1-2011

Photoelectron Spectroscopy of Organic Anions

Scott William Wren
University of Colorado at Boulder, swwren@gmail.com

Photoelectron Spectroscopy of Organic Anions

by

Scott William Wren

B.S. University of California at Davis, 2005

A thesis submitted to the Faculty of the Graduate School of the University of Colorado in partial fulfillment of the requirements for the degree of Doctor of Philosophy

Department of Chemistry and Biochemistry

2011

This Thesis entitled:

Photoelectron Spectroscopy of Organic Anions

written by Scott William Wren

has been approved for the Department of Chemistry and Biochemistry

_____

W. Carl Lineberger

_____

Barney Ellison

Date:_____

The final copy of this thesis has been examined by the signatories, and we find that both the content and the form meet acceptable presentation standards of scholarly work in the above mentioned discipline.

Wren, Scott William (Ph.D., Chemistry, Department of Chemistry and Biochemistry)

Photoelectron Spectroscopy of Organic Anions

Thesis directed by Professor W. Carl Linebergera

Negative ion photoelectron spectroscopy is a very useful tool to investigate the properties of anions and their related neutral molecules. The neutral molecules that are formed when an electron is photodetached are often short-lived reactive radicals, which are difficult to study using other optical spectroscopy techniques. This thesis comprises several investigations that I performed on a series of related gas-phase anionic systems; these systems highlight the advantages and challenges associated with negative ion photoelectron spectroscopy. Additionally, a new innovative velocity mass filter was integrated into the existing instrument and its design and performance is described in detail.

The systems studied in this thesis can be coarsely divided into two classes of molecules. First, a series of six-membered aromatic rings are studied, where a nitrogen atom(s) is either inserted into the phenyl ring or is added as a substituent. Anilinide ($C_6H_5NH^-$) offers a straightforward example of a rigid molecular system having a simple photoelectron spectrum where all the spectral features are easily assigned. A series of five azinide anions ($C_nH_nN_n^-$) are then investigated to understand how the number of nitrogen atom(s) inserted into the phenyl ring and their position within the ring affect the thermochemical properties of the anion and neutral molecules. The photoelectron spectra of all five azinide anions have similar structure, though the measured electron affinities strongly depend on the proximity of the deprotonation site relative to the nitrogen atom(s).

The second class of molecules are anions which undergo drastic geometry changes when an electron is photodetached to form the neutral molecule. A series of halocarbene anions (CX_2^- with X =Cl, Br, I) was investigated to definitively determine the energy difference between the ground state singlet and excited triplet state in the neutral carbene. The related dihalomethyl anions (CHX_2^-) are a much more challenging system to understand. The photoelectron spectra display an extended, structured vibrational progression due to the large geometry change between the anion and the neutral. A similar phenomenon is also found in the final two anions

studied, *c*-$C_4F_8^-$ and SF_6^-, where high-level theoretical modeling is required to analyze the photoelectron spectra.

Dedication

To my teachers. I have had many excellent teachers whose dedication and passion for teaching have impacted me more than they could have realized. Their lessons, both academic and general wisdom, have provided me with the foundation necessary to be successful in graduate school.

Acknowledgements

The work presented in this thesis would not have been possible without the help, support, and guidance of many individuals. I first want to thank my thesis advisor, Carl Lineberger, for allowing me to join his talented research group and for the support and guidance he has offered over the past six years. Graduate school can be very challenging and often times becomes an exercise in perseverance. I couldn't have asked for a better advisor than Carl who allowed me to learn from my mistakes and provided encouragement and advice when it was needed. The number of talented scientists that have passed through Carl's labs over the past forty years is quite staggering, and I feel very fortunate to have been able to contribute to the work done in the basement of JILA.

In addition to Carl, there are many individuals in JILA and in the Chemistry department who were instrumental in my success in graduate school. I feel very privileged to work alongside such talented coworkers and learn from very gifted teachers. The facilities and staff within JILA are certainly among the best in world. Specifically, the technical staff in the electronic and machine shops have been critical in fixing and improving the instrumentation used in this thesis work. The new Wien filter was designed and constructed entirely within JILA by the machine shop and I need to thank Kim Hagen, Blaine Horner, David Alchenberger and Ariel Paul for their contributions to the project.

I also need to thank several professors that have had a lasting influence on me while both in graduate school. Mathias Weber started his career in JILA roughly the same time I started working in Carl's lab and I have appreciated all his suggestions and advice. Veronica Bierbaum has taught me the subtle but important aspects of ion thermochemistry, which was very important in our joint work presented in Chapter 5. Barney Ellison has been a constant source of

support and inspiration over my six years in graduate school. I never left Barney's office without a smile on my face and a head filled with new ideas and projects to work on. Lastly, I wanted to thank Casey Hynes for his dedication and patience in teaching the two graduate courses I took from him. I don't know many professors who put as much work and care in teaching as Casey.

There have also been a large number of visiting scientists that I have had the chance to work with who I owe a large debt of gratitude. Kent Ervin worked as a visiting scientist for six months in JILA and taught me much of what I know about how to theoretically model photoelectron spectra and the details of data analysis. Bob McMahon was also a visiting scientist and helped motivate much of the work currently being performed on in the lab as well as providing a physical organic chemist's point of view on several of the projects in this thesis. David Osborn was the most recent visiting scientist and worked *in the lab* for over six months. It was a great privilege to work with such a knowledgeable individual who is so humble and giving of his time. While David was in lab, he contributed to several lasting improvements to the instrumentation and the methods we use to take data and analyze our results. I also need to thank both John Stanton and Anne McCoy for all their theoretical help on various projects over the years. Though I don't necessarily always understand everything they say, both John and Anne have come to the rescue many times to help understand our results when challenging problems arise.

However the group of individuals that influenced and helped me the most in graduate school are the former and present members of the Lineberger, Ellison, Bierbaum, Weber and Nesbitt groups. There have been so many individuals whom have help me in one way or another in these groups, and I feel it would be impossible to list everyone. I do want to thank a few

individuals whom I interacted with the most. I first need to thank Kristen Lemke, who worked alongside me in lab for the past four years and significantly contributed to much of the work presented in this thesis. I also want to acknowledge Elisa Miller who has been very supportive and helpful over the last six year while becoming a great friend and scientist. Adam Gianola trained me on the PES instrument when I first started working in the lab and has continued to answer my questions long after leaving the lab. He has become a great friend and has offered me support and encouragement in the dark periods when the ions were lost and the laser was broken. I spent several summers working with Stephanie Villano, who patiently taught me about ion chemistry and is one of the most efficient researchers I know. I also want to thank Leonid Sheps. Leonid challenged me to become a better scientist while constantly answering all my questions and helping me with any problems I brought him. I feel Leonid made all of the scientists he worked with better and I owe much of what I learned in graduate school to him.

Finally, I need to thank my family, whom without I would surely not be where I am today. My parents have been very supportive throughout my extended educational journey and taught me many of the skills necessary to survive graduate school. I need to thank my Father in particular in shaping my interest in chemistry. Not only did I have the fortunate opportunity to have him as my general chemistry professor in college, it was in this class that I met my wife. I also need to thank my brother David for his support over the year. Being identical twins who both went to graduate school studying chemistry has resulted in a constant partner in science classes, someone to commiserate with, and a lasting friendship I am very thankful for. However, above everyone else listed in this section, I need to thank two important women in my life. My dog Ona has been thoroughly neglected over large parts of my time in graduate school, but has always been a wonderful companion and happy to see me when I get home. My wife Rachelle

has been by my side for over ten years and has provided an endless supply of encouragement and support throughout undergraduate and graduate school. I can say, without hesitation, I would not be in the position I am today without Rachelle. I cannot thank her enough for the sacrifices she has made which have allowed me to pursue my goals. Rachelle is one of the most talented and caring people I have ever met and I feel so lucky to have her in my life.

Contents

List of Tables

List of Figures

1 Introduction

1.1 Anion Photoelectron Spectroscopy

Photoelectron spectroscopy is a very powerful spectroscopic technique to study the physical and chemical properties of both neutral molecules and ions. Neutral photoelectron spectroscopy is generally more common than its negative ion counterpart, and though both techniques share many similarities, each has its own unique advantages. The following discussion attempts to highlight the differences between these two techniques and the distinct advantages of negative ion photoelectron spectroscopy. Additionally, a brief introduction to negative ion photoelectron spectroscopy is given below in order to better understand the experimental results presented in later chapters.

Photoelectron spectroscopy is a special case of electronic spectroscopy, namely the spectroscopy of bound-free electronic transitions. Electronic spectroscopy is the study of transitions of electrons from one electronic state to another, induced by the emission or absorption of a quantum of electromagnetic radiation.[1] In order to induce a transition between two states, the energy of the photon satisfies resonance condition,

Equation 1.1

$$E_2 - E_1 = h\nu = \frac{hc}{\lambda}$$

where E_1 and E_2 are the energies of the states involved in the transition and λ is the wavelength of the light used to probe the system. Photoelectron spectroscopy differs from conventional electronic spectroscopy in that the photon energy is sufficiently great to eject an electron following photoabsorbtion. The resonance condition stated in Equation 1.1 is still met (hence

energy is still conserved), but the ejected electron carries away with it any energy in excess of ionization following photoabsorption in the form of electron kinetic energy (eKE). In other words, the photon energy is partitioned between the energy required for the transitions from the initial to final state and the kinetic energy of the departing electron. So, unlike conventional electronic absorption spectroscopy where photon energies are measured, the electron kinetic energies are recorded in photoelectron spectroscopy.

Negative ion photoelectron spectroscopy is analogous to neutral photoelectron spectroscopy, except that the initial state is an anion instead of a neutral molecule. When an electron is photodetached from an anion, a neutral molecule is formed. Since the anion valence electrons are weakly bound relative to their counterparts in neutral molecules, the minimum amount of energy required to remove an electron from an anion is correspondingly lower than what is required to ionize a neutral molecule. Thus, by measuring the kinetic energy of the photodetached electron, one obtains a vibrational and electronic spectrum of the transitions between the anion and the final neutral state(s).[2]

Before discussing the complexities of anion photoelectron spectroscopy, it is useful to overview the basics of the technique using a diatomic molecule as an example. Figure 1.1 is a schematic that illustrates the photodetachment process for a simple diatomic anion (AB^-), forming a neutral (AB). The potential energy curves shown are for the ground state of AB^- and AB, as well as the first excited state of AB, and are represented by Morse oscillators. In this figure, photons with fixed energy (E_{hv}) induce transitions from the ground vibrational state of the AB^- anion to a virtual level in the [AB + e^-] continuum. Electrons are then ejected with kinetic energies equal to the difference in energy between the laser photon energy and various vibrational energy levels in the neutral, illustrated as blue arrows in Figure 1.1. The

corresponding photoelectron spectrum is displayed on the right vertical axis, which is on the same energy axis as the potential energy curves. This model diatomic example is useful in understanding negative ion photoelectron spectroscopy and the spectroscopic quantities which can be experimentally measured. It is now convenient to introduce the concept of binding energies, which is defined as

Equation 1.2

$$\mathrm{eBE} = \mathrm{h}\nu - \mathrm{eKE}$$

Though we measure electron kinetic energies (eKE), the photoelectron spectra present in this thesis are plotted in terms of electron binding energies (eBE), as this quantity is independent of the photon energy used.

One of the most useful and important spectroscopic quantities measured in negative ion photoelectron spectroscopy is the energy difference between the ground vibrational and rotational state of the anion ($v'' = 0$, $J'' = 0$) and the neutral ($v' = 0$, $J' = 0$); this energy difference is defined as the adiabatic electron affinity (EA) and is schematically shown in Figure 1.1 as the red vertical arrow. Physically, this is the minimum amount of energy required to remove an electron from the lowest energy state of the anion and is analogous to the ionization energy in neutral photoelectron spectroscopy.

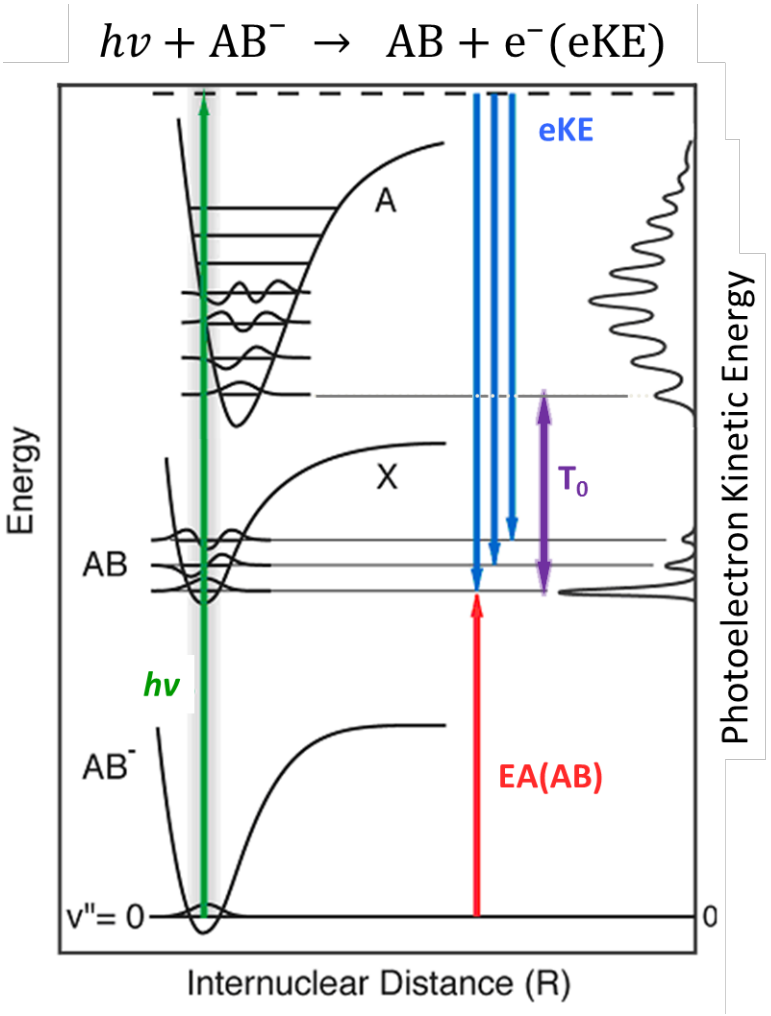

Figure 1.1 Diagram of the photodetachment process for a diatomic anion (AB^-) and the resulting photoelectron spectrum. Potential energy curves are represented by a Morse oscillator and are a function of the internuclear bond distance. Figure is adapted from previous figure by Dr. Leonid Sheps.

It is also possible to determine the energy difference between electronic states of the neutral, if both excited states are low enough in energy to be accessed by the photon energy used. In Figure 1.1, the energy difference between the lowest vibrational and rotational levels of the ground and first excited neutral states is designated as the term energy (T_0). Furthermore, since the spin selection rule for a photodetachment process is $\Delta S = \pm 1/2$, neutral states of different spin multiplicities can be observed in the photoelectron spectrum. For example, many of the anions studied are doublet states, which when an electron is removed, can form either a singlet or a triplet state. The term energy between the singlet and triplet states is known as the singlet – triplet splitting (E_{ST}) and is an important quantity to measure (as will be highlighted in Chapter 6). Transitions between states of different spin multiplicity are strongly forbidden in optical spectroscopy, leading to a unique advantage of anion photoelectron spectroscopy.

The position and relative intensities of the vibrational transitions in the photoelectron spectrum offer additional information about both the anion and the corresponding neutral photodetachment product molecule. As Figure 1.1 illustrates, the peak spacing in a photoelectron spectrum corresponds to the difference in energy between vibrational energy levels in the neutral. This vibrational structure leads directly to determination of the vibrational frequencies and often anharmonicities of active modes in the neutral molecule. Additionally, as will be discussed more in Section 1.4, the intensities of peaks in photoelectron spectra are governed by the Franck-Condon overlap of the vibrational wavefunctions of the anion and the neutral. If there is a large geometry change between the anion and the neutral, as in the neutral excited state A in Figure 1.1, an extended vibrational progression will be observed. This occurs because the best overlap with the anion ground state vibrational wavefunction is with higher vibrational levels in the neutral, which shifts spectral intensity away from the origin. Therefore,

the observed vibrational structure directly relates to the relative geometry changes between the anion and the neutral.

Lastly, the inherent advantage of using an anion as our initial state is that we can select a specific ion of interest by mass filtering our ion beam. This identifies the signal carrier in the photoelectron spectrum. Furthermore, the anion is a chemically distinct species from the neutral that is formed after photodetaching an electron. Therefore, many stable anions have very reactive and unstable neutral counterparts which are very difficult to study by other experimental methods.

1.2 Atomic Species

Photodetachment of electrons from atomic anions is the simplest case of negative anion spectroscopy. Energy is conserved in the photodetachment process and can be represented by

Equation 1.3

$$A^-(E_{elec''}) + h\nu \longrightarrow A(E_{elec'}) + e^-(eKE)$$

where A^- is an atomic anion, A is the neutral, E_{elec} is the electronic energy, and the double prime denotes the initial state (anion) and the single prime denotes the final state (neutral).

For atomic species, the only transitions available are between different electronic states; therefore, all the peaks in the photoelectron spectrum correspond to different states of the neutral atom within the photon energy. As an example, Figure 1.2 shows the photoelectron spectrum of atomic oxygen anion (O^-) taken both at 300 K (solid black line) and 150 K (dotted blue line). The inset energy level diagram represents the different transitions possible between the ground states of the anion ($^2P_{3/2,1/2}$) and neutral ($^3P_{2,1,0}$). Due to spin–orbit coupling, electronic fine structure splittings are present and five of the six known transitions are resolved under experimental conditions optimized for best energy resolution (~ 5 meV).[3] The line width in

atomic spectra is determined by the instrumental resolution. In Figure 1.2 the energy resolution is approximately 8 meV, which is typical for normal operation and representative of the conditions of the experiments in this thesis. The energies of the spin–orbit transitions, represented by red sticks in Figure 1.2, are placed at the known experimental values.[4, 5] Peak (c) corresponds to the EA for oxygen atom (1.461112 eV)[6], which is the transition from the ground state of O^- ($^2P_{3/2}$) to the ground state of O neutral ($^3P_2$). When the O^- anions are cooled to 150 K, there is a reduced population in the higher energy $^2P_{1/2}$ state in the anion, which causes a decrease in the relative intensity of peak (a) and a slight narrowing of peak (c).

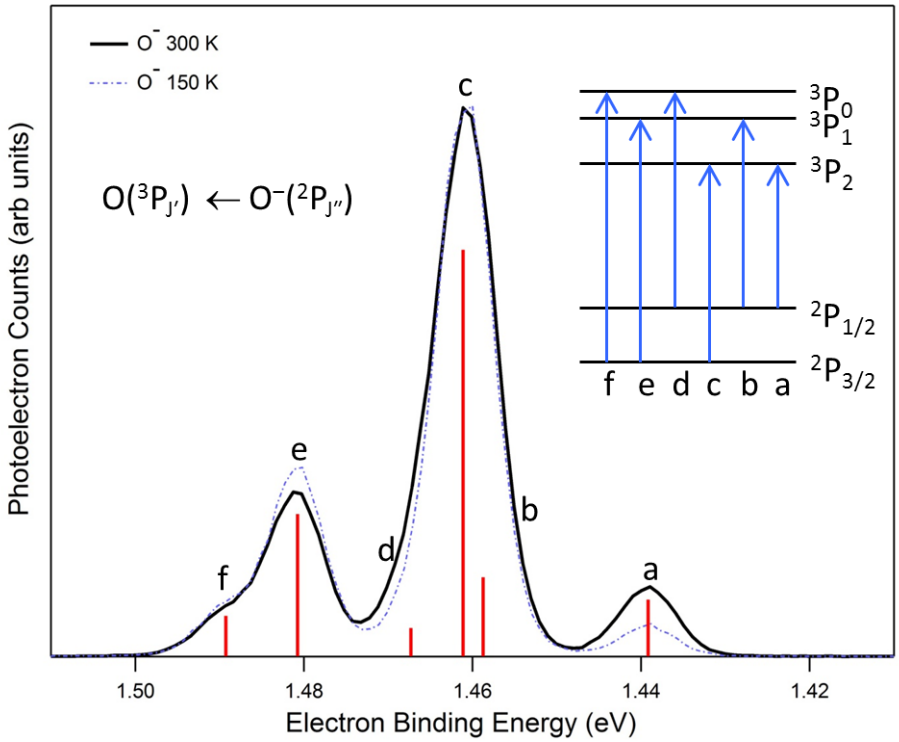

Figure 1.2 Photoelectron spectrum of atomic oxygen anion (O^-) taken both at 300 K and 150 K. Inset energy level diagram is a schematic illustrating the possible transitions from the different spin-orbit energy levels in the anion and neutral. The red sticks indicate the positions of the experimentally measured energy levels of the transitions in the inset diagram.

1.3 Molecular Anion Photodetachment

Electron photodetachment from molecular species is much more complicated than from atoms due to the presence of vibrational and rotational degrees of freedom. Both anions and neutral molecules have vibrational and rotational energy levels accessible, which dramatically increases the number of allowed transitions and the complexity of the photoelectron spectra. Equation 1.3 can be rewritten to include the molecular vibrational and rotational energy levels, $E_{vib}(v)$ and $E_{rot}(J)$, respectively:

Equation 1.4

$$\mathbf{AB}^{-}\left[E_{elec''} + E_{vib}(v'') + E_{rot}(J'')\right] + h\nu \longrightarrow \mathbf{AB}\left[E_{elec'} + E_{vib}(v') + E_{rot}(J')\right] + e^{-}(eKE)$$

However, as mentioned above, our experimental resolution is ≥ 5 meV (40 cm^{-1}), and thus we are unable to resolve individual rotational transitions. In our final analysis (determining the EA) and in spectral simulations we do account for unresolved rotational transitions, which broaden the experimental peak shapes. However we will omit the rotational energy contribution in Equation 1.4, to obtain

Equation 1.5

$$\mathbf{AB}^{-}\left[E_{elec''} + E_{vib}(v'')\right] + h\nu \longrightarrow \mathbf{AB}\left[E_{elec'} + E_{vib}(v')\right] + e^{-}(eKE)$$

We can solve for e^{-}(eKE) in Equation 1.5 obtain an expression that reflects what is actually measured in our photoelectron spectra

Equation 1.6

$$e^{-}(eKE) = h\nu + \mathbf{AB}\left[E_{elec'} + E_{vib}(v')\right] - \mathbf{AB}^{-}\left[E_{elec''} + E_{vib}(v'')\right]$$

Mathematically, this restates what the blue arrows illustrate in Figure 1.1 where the energy of the measured photodetached electrons correspond to the energy difference between the final and

initial states less the photon energy. For example, the transition corresponding to the EA, where v' and v'' are both zero, would be

Equation 1.7

$$e^{-}(eKE) = h\nu + EA$$

where $EA = E_{elec'} - E_{elec''}$.

The flowing afterglow anion source used in our experiments produces anions with a near-thermal (300 K) distribution of vibrational levels in the ground electronic state of the anion. If additional vibrational levels of the anion are populated, we will observe further transitions from excited vibrational states of the anion to the neutral. These vibrational progressions, called "hot bands", are located at smaller binding energies than the origin peak.

1.4 Selection Rules and Photoelectron Intensities

Before carrying out a more complete analysis of a photoelectron spectrum, we need to develop an expression for the intensity of any particular transition in a photoelectron spectrum. The total photodetachment cross section can be written as

Equation 1.8

$$\sigma = \frac{32\pi^4 m_e{}^2 e^2 v_e h\nu}{3hc^2} |\mathbf{M}|^2$$

where m_e and e is the mass and charge of the electron, v_e is the electron velocity, $h\nu$ is the photon energy, h is Planck's constant, c is the speed of light.[2] However, by far the most important component in the expression for the photodetachment cross section is the transition dipole moment, **M**, which is defined as

Equation 1.9

$$\mathbf{M} = \left\langle \psi''(r,q) \middle| \boldsymbol{\mu}(r,q) \middle| \psi'(r,q) \right\rangle$$

where ψ'' and ψ' are the initial (anion) and final state (neutral plus e^-) wavefunctions, which are a function of nuclear (q) and electronic (r) coordinates. The vector quantity **μ** is the electronic transition dipole moment operator between the initial and final wavefunctions. In general, the total intensity of an electronic transition is given by **M,** which is obtained by summing over all initial and final state energy levels. A transition is allowed under the electric–dipole approximation if the transition dipole moment in Equation 1.9 is non-zero. We invoke the Born–Oppenheimer approximation and factor the total wavefunction into electronic, vibrational, and rotational parts

Equation 1.10

$$\psi(r,q) = \psi_{elec}(r)\psi_{vib}(q)\psi_{rot}(q)$$

For fixed nuclear coordinates, the rotational wavefunction, ψ_{rot}, is only dependent on the orientation of the molecule relative to arbitrary laboratory coordinates and the rotational overlap integrals will be the same for all vibrational states.[1, 2] Therefore, the rotational wavefunction in Equation 1.10 will be ignored for this treatment. Inserting the partitioned wavefunction from Equation 1.10 into Equation 1.9, we obtain

Equation 1.11

$$\mathbf{M} = \left\langle \psi''_{elec}(r)\psi''_{vib}(q) \middle| \boldsymbol{\mu}_{elec}(r) + \boldsymbol{\mu}_{nuc}(q) \middle| \psi'_{elec}(r)\psi'_{vib}(q) \right\rangle$$

where the transition moment operator is expressed as the sum of the electronic and nuclear parts. We can further separate Equation 1.11 into two expressions that are solely a function of either nuclear or electronic coordinates. However, the term that includes μ_{nuc} is zero because it involves two electronic wavefunctions that are orthogonal; this requires the overlap integral to be zero. Thus, we are left with the following simplified expression for **M**

Equation 1.12

$$\mathbf{M} = \left\langle \psi''_{elec}(r) \middle| \mu_{elec} \middle| \psi'_{elec}(r) \right\rangle \cdot \left\langle \psi''_{vib}(q) \middle| \psi'_{vib}(q) \right\rangle$$

where, using the Condon approximation, the electronic transition moment is assumed to be constant over the range of vibrational coordinates sampled.[2] Equation 1.12, the product of two terms, is very useful as the first term is the basis for electronic selection rules and the second term is the basis for vibrational intensities. Using Equation 1.12, we obtain an expression that is proportional to the cross section for photodetachment

Equation 1.13

$$\sigma \propto \nu_e \cdot |\mathbf{M}|^2 = \nu_e \cdot \left|\left\langle \psi''_{elec}(r)\middle|\mu_{elec}\middle|\psi'_{elec}(r)\right\rangle \cdot \left\langle \psi''_{vib}(q)\middle|\psi'_{vib}(q)\right\rangle\right|^2$$

where the constant common factors in Equation 1.8 have been dropped. The integral that includes the electronic wavefunctions in Equation 1.13 is very similar for all vibrational transitions of a given electronic transition.[7] It is therefore the second integral that determines the relative intensities of the band features for a particular electronic transition.

The overlap integral of the vibrational wavefunctions in Equation 1.13 is better known as the Franck–Condon Factor (FCF) for a $v'' \rightarrow v'$ transition

Equation 1.14

$$\mathrm{FCF} = \left|\left\langle \psi''_{vib}(q)\middle|\psi'_{vib}(q)\right\rangle\right|^2$$

which determines the vibrational contribution to the transition probability, $|\mathbf{M}|^2$. The overlap of the anion and neutral vibrational wavefunctions is governed by the Franck–Condon principle, which states that an electronic transition is so fast, compared to nuclear motion, that the nuclei still have nearly the same position and momentum immediately before and after the transition.[7]

The simple diatomic example in Figure 1.1 illustrates how the Franck–Condon overlap affects the band structure and peak intensities observed in photoelectron spectroscopy. In this example, there are two neutral states accessible, which have very different bond lengths (R). The ground state (X) has a very similar equilibrium bond length to the anion, which leads to both

similar potential energy curves and vibrational wavefunctions. The best overlap of vibrational wavefunctions in Figure 1.1 is between the v "= 0 and the ν'= 0 wavefunctions, which will produce a relatively large Franck–Condon factor and corresponds to the most intense peak in the photoelectron spectrum. However, the excited neutral state (A) has a different equilibrium bond length compared to the anion, which shifts the potential energy curve. Thus, the best vertical overlap with the anion wavefunction will be at much higher vibrational energy levels of the neutral. Mathematically, if the amplitude and phase of two wavefunctions are very different, the positive and negative contributions to the overlap will tend to cancel in the integral in Equation 1.14, yielding very small Franck–Condon factors.

Polyatomic molecules have many more degrees of freedom than a diatomic and the vibrations cannot be described in a simple two-dimensional picture. In the harmonic oscillator limit, the vibrational motion of polyatomic molecules can be reduced to a superposition of vibrations in 3N – 6 normal modes (3N – 5 for linear molecules).[1] The total vibrational wavefunction can then be expressed as a product of individual normal mode wavefunctions

Equation 1.15

$$\psi_{\mathrm{vib}}(\mathrm{Q}) = \prod_{3\mathrm{N}-6} \psi_1(\mathrm{Q}_1)\psi_2(\mathrm{Q}_2)\cdots\psi_{3\mathrm{N}-6}(\mathrm{Q}_{3\mathrm{N}-6})$$

where Q_i is the normal mode coordinate for vibrational mode ν_i. For polyatomic molecules, the total vibrational wavefunction represented by Equation 1.15 for the anion and neutral is inserted into Equation 1.14. Therefore, instead of having one vibrational overlap integral, there is a product of overlap integrals, one for each normal mode. In this approach, each vibrational mode is assumed to be independent and uncoupled from the other modes, though in later chapters it will be shown that this is not always the case.

If all the vibrations in a molecule had non-negligible FCFs, or are active, the photoelectron spectrum of even a small molecule would quickly become very difficult to analyze. Fortunately, not all vibrations are active. In contrast, *only totally symmetric vibrational modes*[‡] *generally dominate the photoelectron spectra*. However, unlike diatomic wavefunctions, polyatomic vibrational wavefunctions can be either totally symmetric or non-totally symmetric depending on the symmetry of the normal coordinates and the vibrational quantum number. Additionally, non-totally symmetric normal coordinates will have a vibrational wavefunction that will alternate between being totally symmetric and non-totally symmetric as ν changes from even to odd. The consequence of this alternating symmetry of the vibrational wavefunction is that non-totally symmetric modes can be active, but only $\Delta v = 0, \pm 2, \pm 4, \pm 6, \cdots$ transitions are allowed. However, under most circumstances only the $\Delta v = 0$ (0–0) transition will have any appreciable intensity.

Using the ideas presented above, we can make some general conclusions about vibrational selection rules. In general, totally symmetric vibrational modes will tend to have the only significant intensity in a photoelectron spectrum. Furthermore, totally symmetric vibrations that reflect the geometry change between the anion and neutral will carry most of the signal strength and dominate the photoelectron spectrum. For example, if the bond angle in a nonlinear triatomic molecule has a dramatic change from the anion to the neutral, one would expect the symmetric bend vibration to be active in the photoelectron spectrum. Lastly, modes that are non-totally symmetric can be active, but only if certain conditions are met.

As mentioned previously, traditional electronic spectroscopy has the strict spin selection rule that only transitions between states of the same multiplicity are allowed; therefore $\Delta S = 0$. Photoelectron spectroscopy still has the constraint that the total spin of the system must be

[‡] totally symmetric vibrations maintain the same point group symmetry throughout the entire vibration

conserved; however the detached electron departs with a spin of $\pm 1/2\,\hbar$ and the spin of the neutral molecule change by the same amount. Since only one electron is involved in a transition, the general spin selection rule for photodetachment is $\Delta S = \pm 1/2$. The consequence of this selection rule is that the spin multiplicity *must* change for a transition to occur. It also allows for the possibility to make transitions to both singlet and triplet states of the neutral if the ground state of the anion is a doublet state.

1.5 Photoelectron Angular Distributions

The intensity of the photoelectron signal varies with the angle between the laser polarization vector and the electron collection direction; the orientation of the laser polarization can be manipulated by rotating a half-waveplate in the laser beam. In the electric dipole approximation for one photon photoabsorption, the angular dependence of the photodetached intensity is given by the well-known relation[8]

Equation 1.16

$$I(\theta) = \frac{\sigma_{total}}{4\pi}(1 + \beta \cdot P_2(\cos\theta))$$

where θ is the angle between the electric field vector of the laser light and the direction of the ejected electron, β is the asymmetry parameter ($-1 < \beta \leq +2$), σ is the total photodetachment cross section, and P_2 (cos θ) is the second associated Legendre polynomial given by

Equation 1.17

$$P_2(\cos\theta) = \frac{1}{2}(3\cos^2\theta - 1)$$

When the laser polarization is adjusted such that θ = 54.7°, referred to as the "magic" angle, the second associated Legendre polynomial vanishes and the photoelectron signal is proportional to the total cross section, independent of the value of β. Therefore, at the magic angle, the

photoelectron signal is independent of β and corresponds to the total detachment cross section (σ_{total}).

The anisotropy parameter β is an especially useful physical property to determine. Measurement of β is achieved by rotating a half waveplate in small (5°) increments through at least 180° (which corresponds to 360° rotation of the laser polarization) while collecting photoelectrons from a narrow kinetic energy range corresponding to a single peak/feature. Then, a least squares fit of the data to Equation 1.16 extracts the β parameter. A less accurate method (but generally sufficient for determining the anion orbital from which photodetachment occurred) for determining β employs measuring photoelectron intensities at two angles, 0° and 90°, and using the relationship

Equation 1.18

$$\beta = \frac{I_0 - I_{90}}{(1/2)\, I_0 + I_{90}}$$

Angular distribution measurements provide qualitative insight about the angular momentum state from which the electron was detached. When an electron is detached from an atom, β is dependent on the momentum contained by the photoelectron. This is because the total angular momentum must be conserved by the system. The angular momentum selection rule for atomic photodetachment is $\Delta\ell = \pm 1$, as the photon imparts one unit of angular momentum to the electron. Therefore, an electron detached from an s orbital ($\ell = 0$) departs as a pure p-wave ($\ell = 1$) which corresponds to a $\beta \approx 2$. In this situation, the maximum photoelectron intensity is along the electric field vector of the light ($\theta = 0°$). On the other hand, if an electron is detached from a p orbital ($\ell = 1$), the electron will depart as both s-wave ($\ell = 0$) and d-waves ($\ell = 2$), where partial-wave interference will influence the measured β value. Close to the detachment threshold, the lower angular momentum state will dominate and only s-wave detachment will be

observed, producing isotropic angular distribution of ejected electrons ($\beta \approx 0$). Away from threshold (1 eV or higher), both angular momentum states with be present and the partial waves will interfere which will tend to produce negative β values.[9]

The photoelectron angular distributions arising from molecular photodetachment are much more complicated. Atomic systems have inherent spherical symmetry so the atom's orientation does not affect the angular distribution. However, this is not the case for molecules, where random orientation leads to averaging of the observed photoelectron angular distribution over molecular orientations. It is possible to measure *molecular frame* photoelectron angular distributions, but this procedure is complex and generally involves dissociative photodetachment and requires using coincident detection of molecular fragments and photodetached elections.[10] The mathematical treatment is beyond the scope of this work,[8, 11] but we can still obtain valuable qualitative anion orbital information from the β values in molecular photodetachment. It has been shown from previous negative ion photoelectron studies[12-14] that each electronic state of a particular neutral is expected to have a characteristic value for β. Therefore, the peaks in a vibrational progression belonging to transitions to a single neutral state will have very similar β values, though these values will vary slightly over extended energy ranges. Furthermore, past results have indicated that detachment from σ-type orbitals typically have large positive β (> 1), while detachment producing 0.5 – 1.5 eV photoelectrons arising from π-type orbitals will have a negative β, indicating interference between s- and d-partial waves.[9, 12, 14] Therefore, the β value can be used as an indicator of the symmetry of the orbital from which the electron is detached.

1.6 Thermodynamics

As mentioned earlier, the primary result from a photoelectron spectrum of a molecular anion is the electron affinity of the corresponding neutral radical, EA(R). The EA can be

combined with the measured enthalpy of deprotonation ($\Delta_{acid}H_{298}$(RH)) and the known ionization energy of the hydrogen atom[15] in a thermochemical cycle[16, 17] to determine the bond dissociation energy D_{298}(RH). This negative ion cycle is shown schematically below in Figure 1.3

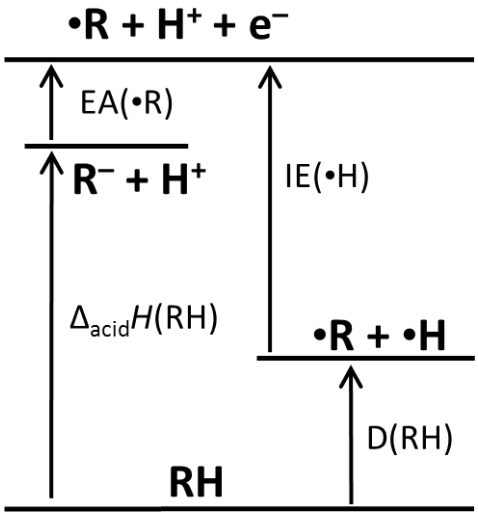

Figure 1.3 Negative ion thermochemistry cycle that can be used to determine the bond dissociation energy of a R–H bond. In the figure, EA(R) is the electron affinity of the radical, $\Delta_{acid}H$(RH) is the enthalpy of deprotonation of the hydrogenated neutral, IE(H) is the well-known ionization energy of hydrogen atom, and D(RH) is the homolytic bond dissociation energy. In order to obtain information from this thermochemical cycle, two of the three unknown values need to be experimentally determined.

We can employ this thermochemical cycle with our measured EA(R) to determine either the ($\Delta_{acid}H$(RH) or the D(RH) if either is already known. Fortunately, many of the enthalpies of deprotonation of the systems presented in this thesis have been measured,[18-23] which allows for determination of many previously unknown C–H bond strengths using the following relationship:

Equation 1.19

$$\mathrm{D(RH)} = \mathrm{EA(R)} + \Delta_{\mathrm{acid}}\mathrm{H(RH)} - \mathrm{IE(H)}$$

The enthalpies of deprotonation are based on experiments typically measured at 300 K[17, 18, 23] and the electron affinity and ionization energy are 0 K measurements; therefore, a small thermal correction is needed when using Equation 1.19 to associate the bond dissociation energy with a temperature (either 0 or 300 K). However, this thermal correction is always smaller than 0.3 kcal mol^{-1} so it is commonly ignored.[24] Alternatively, D(RH) can be measured with very accurate spectroscopic techniques,[25] which when combined with our EA, lead to very accurate values for the enthalpy of deprotonation (and the related gas phase acidity).

1.7 Survey of Thesis Topics

I have had the opportunity to be involved in many different projects as a graduate student, many of which are contained within this dissertation. The molecular systems presented here are collected into chapters which share similar themes and properties. Chapters 2 and 3 focus on the instrumentation and experimental techniques used to collect the photoelectron spectra presented in the following chapters. Chapter 2 presents a comprehensive overview of the critical components of the apparatus including the ion source, ion optics and mass filter, the laser system, electron analyzer, and detection method. Chapter 3 goes into detail on the new velocity mass filter that was recently installed in our instrument along with an overview of how such filters operate. Figure 1.4 illustrates the organic ions which are studied using photoelectron spectroscopy in Chapters 4 – 7. A short summary of these experimental chapters are given below.

Chapter 4 reports the photoelectron spectra of anilinide. This photoelectron spectrum is very simple and easily analyzed compared to the other molecular species in this thesis. A regular vibrational progression with a clear origin is observed in the photoelectron spectrum, which readily allows for the determination of the electron affinity of the anilino radical. Additionally,

the anilino radical is isoelectronic with previously studied benzyl and phenoxyl radicals and the structures in the photoelectron spectra are very similar with the analogous active vibrations.

Chapter 5 investigates the thermochemistry of a series of five azine anions: pyridinide, 1,2-diazinide, 1,3-diazinide, 1,4-diazininde, and 1,3,5-triazinide. Studying six-membered rings with one, two, and three inserted nitrogen atoms allows for an understanding of how the nitrogen affects the energetics and structure of the azinide anions and azinyl radicals. The structure in the five photoelectron spectra is very similar with only two dominant active modes contributing to the majority of the spectral features. Using recent gas-phase acidity measurements, the C–H bond strengths in all five azines are determined.

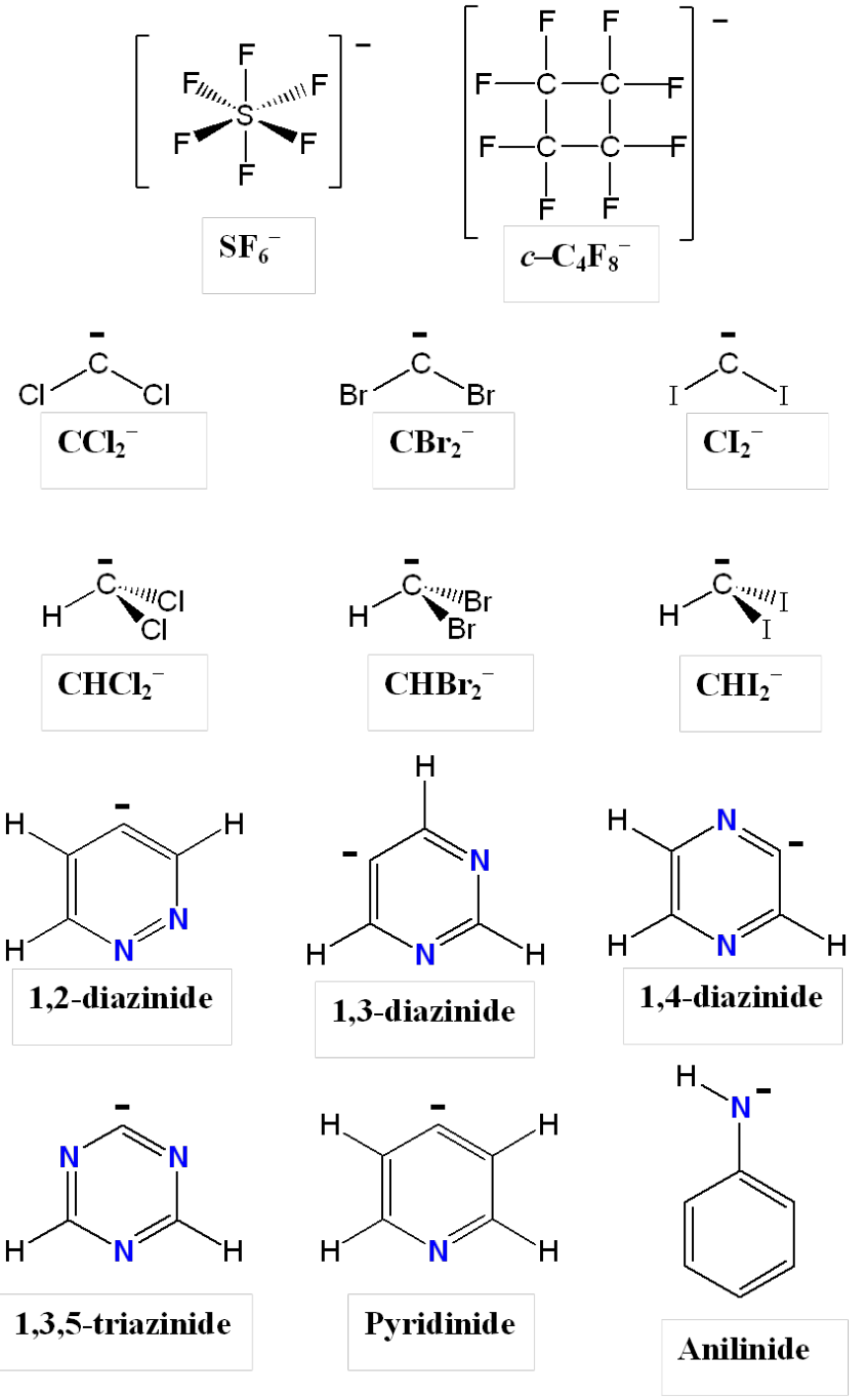

Figure 1.4 Organic anions which have been studied using photoelectron spectroscopy in this thesis. Chapter 4: Anilinide. Chapter 5: Pyridinide, 1,2-diazinide, 1,3-diazinide, 1,4-diazinide, 1,3,5-triazinide. Chapter 6: CCl_2^-, CBr_2^-, CI_2^-, $CHCl_2^-$, $CHBr_2^-$, CHI_2^-. Chapter 7: SF_6^-, *c*–C_4F_8.

Chapter 6 focuses on a series of small halogen-containing molecules, which present unique experimental and theoretical challenges. The dihalocarbenes (CX_2 with X = Cl, Br, I) had been previously studied and singlet-triplet energy splittings determined in our laboratory, but recently high-level calculations called these results into question and prompted our reinvestigation. The neutral carbenes formed from the doublet state of the anion can have either singlet or triplet multiplicity, which have very different chemical and energetic properties. The singlet-triplet splitting in these dihalocarbenes was the source of the discrepancy, and we were able to determine the limited mass resolution in the earlier experiment had allowed previously undetected dihalomethyl anions (CHX_2) to contaminate the earlier data. We were able to make the CHX_2^- cleanly and subtract their contribution from the CX_2^- spectra. In an independent study, we investigated the previously unknown CHX_2^- photoelectron spectra. These spectra display a broad, structured vibrational progression due to a large geometry change between the anion and corresponding neutral. Sophisticated calculations are necessary to understand the origins of the vibrational structure observed in the photoelectron spectra.

Finally, Chapter 7 describes the photoelectron spectra of $C_4F_8^-$ and SF_6^-, obtained in a joint experimental effort between two research labs.[26] The photoelectron spectra for these systems illustrate broad vibrational progressions which have very harmonic peak spacing. This extended progression is due to a large relative geometry change from the equilibrium structure of the anion to the corresponding neutral. This large geometry change makes determination of the origin experimentally unfeasible and provides a challenge in our ability to theoretically model the photoelectron spectrum. As in Chapter 6, we rely on the assistance of high-level calculations to better understand the experimental results.

1.8 References

1. Ellis, A.M., M. Feher, and T.G. Wright, *Electronic and Photoelectron Spectroscopy* 2005, Cambridge: Cambridge University Press.
2. Ervin, K.M. and W.C. Lineberger, *Advances in Gas Phase Ion Chemistry*, in *Advances in Gas Phase Ion Chemistry*, N.G. Adams and L.M. Babcock, Editors. 1992, JAI: Greenwich. p. 121.
3. Ervin, K.M., et al., *The Only Stable State of O_2^- Is the $X\,^2\Pi_g$ Ground State and It (Still!) Has an Adiabatic Electron Detachment Energy of 0.45 eV.* J. Phys. Chem. A, 2003. **107**(41): p. 8521.
4. Andersen, T., H.K. Haugen, and H. Hotop, *Binding energies in atomic negative ions: III.* Journal of Physical and Chemical Reference Data, 1999. **28**(6): p. 1511-1533.
5. Kelleher, D.E., et al., *The new NIST Atomic Spectra Database.* Physica Scripta, 1999. **T83**: p. 158-161.
6. Neumark, D.M., et al., *Laser photodetachment measurement of the electron-affinity of atomic oxygen.* Phys. Rev. A, 1985. **32**(3): p. 1890.
7. Herzberg, G., *Electronic Spectra and Electronic Structure of Polyatomic Molecules*. 2 ed. Molecular Spectra and Molecular Structure. Vol. 1. 1966, New York: Van Nostrand Reinhold. Chaps. 4 and 5.
8. Cooper, J. and R.N. Zare, *Angular Distribution Of Photoelectrons.* J. Chem. Phys., 1968. **48**(2): p. 942.
9. Hanstorp, D., C. Bengtsson, and D.J. Larson, *Angular-distributions in photodetachment from O.* Physical Review A, 1989. **40**(2): p. 670-675.
10. Continetti, R.E., *Coincidence Spectroscopy.* Annual Review of Physical Chemistry, 2001. **52**(1): p. 165-192.
11. Mabbs, R., et al., *Photoelectron imaging: an experimental window into electronic structure.* Chemical Society Reviews, 2009. **38**(8): p. 2169-2177.
12. Gunion, R.F., et al., *Ultraviolet photoelectron-spectroscopy of the phenide, benzyl and phenoxide anions, with ab initio calculations.* International Journal of Mass Spectrometry and Ion Processes, 1992. **117**(1-3): p. 601-620.
13. Vogelhuber, K.M., et al., *The C-H bond dissociation energy of furan: Photoelectron spectroscopy of the furanide anion.* Journal of Chemical Physics, 2011. **134**(6).
14. Surber, E., R. Mabbs, and A. Sanov, *Probing the Electronic Structure of Small Molecular Anions by Photoelectron Imaging†.* The Journal of Physical Chemistry A, 2003. **107**(40): p. 8215-8224.
15. WebBook, N.C., *NIST Standard Reference Database*.
16. Brauman, J.I. and L.K. Blair, *Gas-phase acidities of alcohols.* Journal of the American Chemical Society, 1970. **92**(20): p. 5986.

17. Davico, G.E., et al., *The C-H bond-energy of benzene.* Journal of the American Chemical Society, 1995. **117**(9): p. 2590-2599.

18. DePuy, C.H., V.M. Bierbaum, and R. Damrauer, *Relative gas-phase acidities of the alkanes.* Journal of the American Chemical Society, 1984. **106**(14): p. 4051-4053.

19. DePuy, C.H., S.R. Kass, and G.P. Bean, *Formation and Reactions of Heteroaromatic Anions in the Gas-Phase.* J. Org. Chem., 1988. **53**(19): p. 4427.

20. Ellison, G.B., et al., *Thermochemistry of the benzyl and allyl radicals and ions.* International Journal of Mass Spectrometry and Ion Processes, 1996. **156**(1-2): p. 109-131.

21. Robinson, M.S., et al., *Experimental studies of allene, methylacetylene, and the propargyl radical- Bond-dissociation energies, gas-phase acidities, and ion-molecule chemistry.* Journal of the American Chemical Society, 1995. **117**(25): p. 6766-6778.

22. Villano, S.M., et al., *Photoelectron Spectroscopy and Thermochemistry of the Peroxyformate Anion.* Journal of Physical Chemistry A, 2010. **114**(1): p. 191-200.

23. Eyet, N., S.M. Villano, and V.M. Bierbaum, *Anchoring the gas-phase acidity scale: From formic acid to methanethiol.* International Journal of Mass Spectrometry, 2009. **283**(1-3): p. 26-29.

24. Berkowitz, J., G.B. Ellison, and D. Gutman, *3 methods to measure RH bond-energies.* Journal of Physical Chemistry, 1994. **98**(11): p. 2744-2765.

25. King, G.A., T.A.A. Oliver, and M.N.R. Ashfold, *Dynamical insights into (1)pi sigma* state mediated photodissociation of aniline.* Journal of Chemical Physics, 2010. **132**(21).

26. Bopp, J.C., et al., *Spectroscopic characterization of the isolated SF_6^- and $C_4F_8^-$ anions: Observation of very long harmonic progressions in symmetric deformation modes upon photodetachment.* Journal of Physical Chemistry A, 2007. **111**(7): p. 1214-1221.

2 Experimental Methods

2.1 Introduction

The photoelectron spectrometer used for the experiment described in this thesis has been in operation, in one form or another, since 1967.[1] Many changes, improvements, and additions have occurred over the past 40 years, but the basic technique of negative ion photoelectron spectroscopy was born in the basement of JILA on our apparatus. The current instrument can be summarized in five main sections, which are illustrated in Figure 2.1. Ions are formed using a flowing afterglow in the ion source region. Following formation, ions are accelerated and focused using a series of ion optics, and then pass through a Wien velocity filter. The ions that pass through the filter undeflected intersect a fixed frequency laser beam in the interaction region. Photodetached electrons are collected using a hemispherical energy analyzer and then imaged onto a position sensitive detector.

Each of the sections mentioned above are described in detail in this chapter. For more detailed and exhaustive descriptions of this apparatus, readers are referred to previous accounts.[2-5]

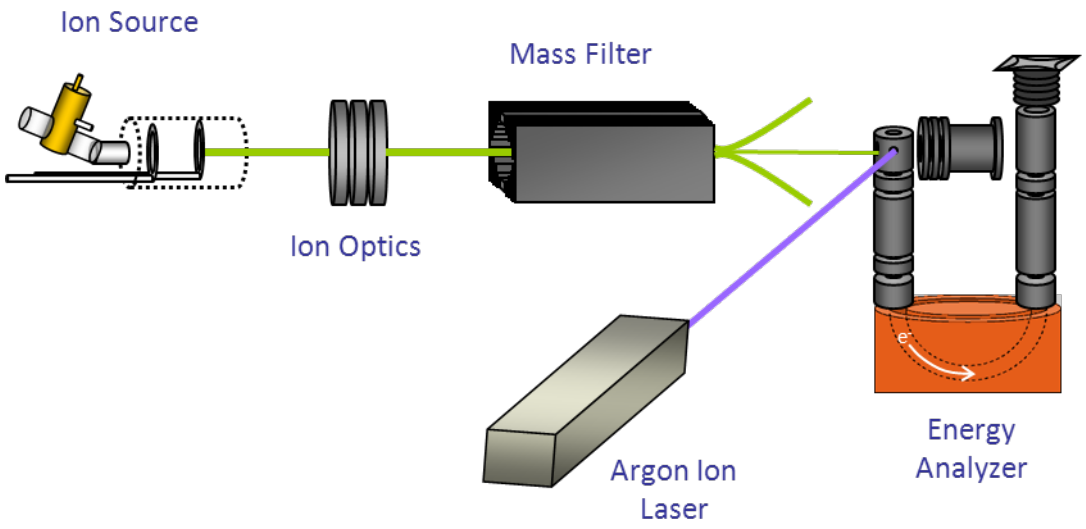

Figure 2.1 Schematic illustrating the main components of the negative ion photoelectron spectrometer

2.2 Ion Source

Though several ion sources have previously been used on this apparatus[6, 7], all of the experiments presented here were conducted using a microwave discharge flowing afterglow ion source.[8, 9] There are several advantages of this type of ion source. First, we can generate continuous and stable ion beams of a single target anion with nanoampere ion currents. Second, we can perform rational stepwise gas-phase reactions in our flow tube to synthesize anions that are difficult or challenging to make otherwise. Third, we use high densities (~ 1 Torr) of helium buffer gas which will, on average, collide with the anions formed $10^4 - 10^5$ times to rotationally and vibrationally thermalize the ions. The rotational temperature of ions made in the source, without external cooling, has been measured to be ~ 300 K.[2] An external liquid nitrogen jacket ,which surrounds the flow tube, can additionally cool the ions in the synthesis region to ~ 150 K. Finally, the flowing afterglow is very versatile; we can easily

extend or shorten the flow reactor tube and the entire source region can be easily disassembled and cleaned.

The microwave discharge is composed of two main parts: a brass 2.45 GHz Evenson-type microwave cavity[8] and a quartz discharge cylinder that is inserted through the cavity. A schematic of the microwave discharge is shown in Figure 2.2. Helium buffer gas, which has first been purified by passage through a molecular sieve trap cooled with liquid nitrogen, is introduced into the discharge cylinder. The gas flow rate of helium (3–10 atm L sec^{-1}) is controlled by a feedback-stabilized mass flow controller (Tylan FC 262) to maintain a constant pressure in the source region of approximately 0.5 Torr. Trace amounts of oxygen (2–5 cm^3 min^{-1}) is seeded in the helium. The microwave discharge is operated by a microwave power generator (Opthos, MPG 4). To form the plasma, ~ 70 W of forward power is applied to cavity with a Tesla coil used to initiate the plasma in the discharge cylinder. Once a stable discharge plasma is obtained, the forward power is reduced to ~ 10 W. Reducing the power of the generator minimizes the reflected power and limits any excess heating of the ions created in the plasma. The plasma absorbs almost all of the forward power under these conditions leading to the low reflected power.

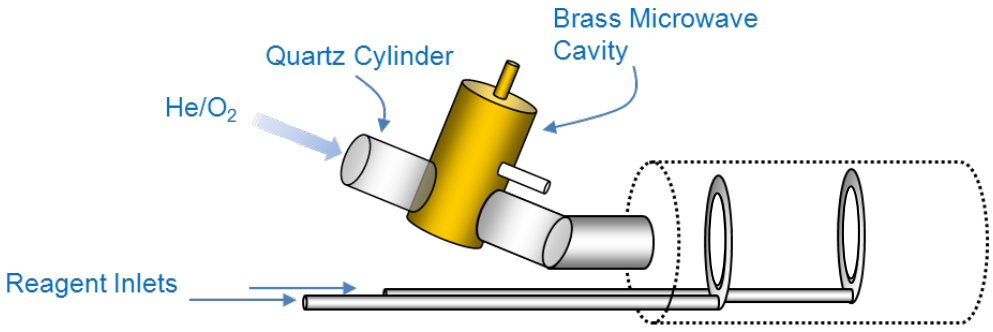

Figure 2.2 Schematic of the flowing afterglow microwave discharge. The position of the reaction inlets can be adjusted independently.

A number of different species are formed in a pure helium discharge including He, He^+, He_2^+, electrons, and metastable He atoms (2 ^{3}S and 2 ^{1}S).[8] Ions are produced by addition of neutral gas reagents directly into or after the helium plasma. One mechanism by which negative ions are formed in the discharge is by dissociative electron attachment in the microwave discharge region.[10] Oxygen radical anion (O^-), which is used extensively in our experiments, is formed using this mechanism and is shown in the reaction below

Scheme 2.1

$$O_2 + e^- \rightarrow (O_2^*)^- \rightarrow O^- + O$$

where e^- is a low energy electron produced in the plasma that attaches to an oxygen atom, which then dissociates to form O^- and a neutral oxygen radical.[11]

In order to produce the ion of interest, a neutral precursor molecule is added downstream of the discharge through a ring reagent inlet, illustrated in Figure 2.2. The reaction of O^- with organic molecules (RH_2) has been studied in great detail[10, 12] but the general product channels are:

Scheme 2.2

$$O^- + RH_2 \rightarrow R^- + H_2O$$

$$O^- + RH_2 \rightarrow RH^- + OH$$

$$O^- + RH_2 \rightarrow RH + OH^-$$

$$O^- + RH_2 \rightarrow RHO^- + H$$

The first two reactions are the dominant channels observed in our ion source: the abstraction of either H_2^+ or H^+. In the first reaction, where a net H_2^+ is abstracted from RH_2, the hydrogen atoms can either be on the same carbon center or on different carbon atoms in the molecule. Often, only the removal of one proton is desired. In this case, methane (CH_4) is introduced downstream of O^-, forming hydroxide (OH^-) by the following reaction:

Scheme 2.3

$$O^- + CH_4 \rightarrow OH^- + CH_3$$

Following OH^- formation, the organic precursor is added through a reagent inlet downstream of the methane inlet and the following reaction occurs

Scheme 2.4

$$OH^- + RH_2 \rightarrow H_2O + RH^-$$

In order to make sure all the O^- has been removed through Scheme 2.3, excess methane is added until all the measurable O^- signal (both ion current and photoelectron counts) is depleted. The flow rates of helium, oxygen, and the precursor molecules are optimized to maximize ion current at the interaction region. The reagent inlet positions can also be varied during the course of an experiment to optimize ion signal.

Under typical experimental conditions, ions are thermalized in the ion source to approximately room temperature. A jacket that surrounds the flow tube can be filled with liquid nitrogen to further cool the ions to approximately ~ 150 K. As will be shown in later chapters, cooling the ions suppresses hot bands, which often results in a less congested and cleaner photoelectron spectrum with an unambiguous origin peak. Cooling the flow tube can reduce the ion current and is best used for experiments with appreciable ion signal at room temperature (> 100 pA) or for ions with large photodetachment cross sections.

The ion source region is maintained at a constant pressure of ~ 0.5 Torr by a Stokes roots blower pump is used to pump away the helium, which provides 330 L sec-1 of pumping speed. A skimmer nosecone (1-mm diameter) is placed at the end of the flow tube, which serves two purposes: to gently extract the ions with a small potential bias (0–3 V), and to create a pressure differential between the source region and the remainder of the apparatus.

The potential bias is kept relatively low to avoid heating the thermalized ions in the extraction process.[13]

2.3 Ion Optics and Mass Selection

Figure 2.3 is a schematic overview of the instrument illustrating the relative position of all the ion optics and major components of the apparatus. After extraction from the flow tube through the nosecone, the ions pass through a series of adjustable ion lenses used to focus, accelerate, and steer the ion beam. The first set of lenses (L1–6) accelerates the ion beam from the nosecone extraction voltage to the beam voltage of 735 V. Elements L1–4 and are independently controlled, while L5 and L6 have constant applied potentials (400 and 735 V

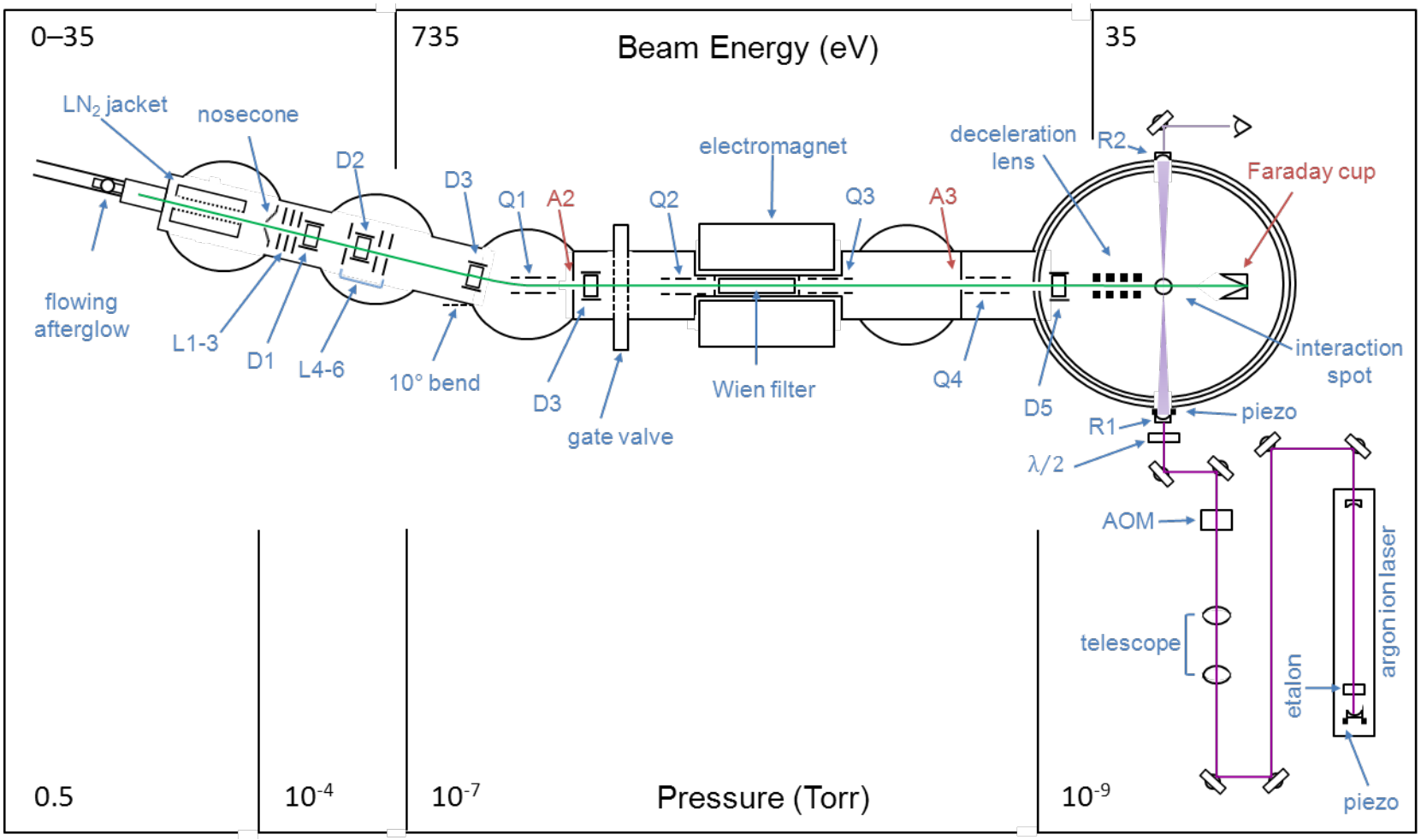

Figure 2.3 Schematic overview of the major components of the photoelectron spectrometer. The different regions of pressure and ion beam energy are label on the bottom and top axis, respectively.

respectively). The first deflector (D1) has independent horizontal and vertical deflectors and is referenced to the voltage of L3, while D2 is referenced to the voltage of L4. The third deflector (D3) horizontally steers the ions through a 10° bend in the ion beam flight path, while any neutral molecules or photons generated in the source region continue undeflected and collide with the chamber walls. This region of the instrument is pumped with a 2000 L sec^{-1} six-inch diffusion pump that maintains a pressure of 10^{-4} Torr.

After the 10° bend, the ions encounter the first of four quadrupole lenses (Q1–Q4) which are used to focus and steer the ion beam. The purpose of the quadrupoles is to focus and deflect the ion beam using static electric potentials[**]. Each quadrupole lens unit is made of 12 elements which are divided into three separate quadrupole elements, shown in Figure 2.4.[14] The middle element also acts primarily as an independent vertical and horizontal deflectors used to steer the ion beam. The three quadrupole lens elements also are used to spatially focus the ion beam. The quadrupole lenses are designed to spatially flatten the ion beam in a two-dimensional plane. Q1 and Q3 shape the ion beam in a horizontal plane and Q2 and Q4 shape the ion beam into a vertical plane. The net result of paired quadrupole focusing is a highly focused ion beam at the entrance of the Wien filter (Q1 and Q2) and at the interaction region (Q3 and Q4). Recently, Q1, Q2 and Q3 were refurbished; the pole elements were not changed, but the connecting wire and spacers between the poles were replaced with vacuum compatible insulated wire and Ultem spacers, respectively (see Section 3.4). Directly after Q1 is a 1.5 mm skimmer aperture (A2) used to measure the current of the ion beam produced in the source region. A2 is biased to the ion beam voltage (735 V) and electrically isolated from the rest of the instrument, where typical

[**] this mode of operation is very different from quadrupoles used as a mass filter, which use both dc electric fields and radio frequencies to control the trajectory of ion beams

ion currents of 10 nA are measured. The voltages of the ion optics preceding A2 can be optimized by monitoring and maximizing the ion current while maintaining a “dip” signal created by ions passing through the aperture.

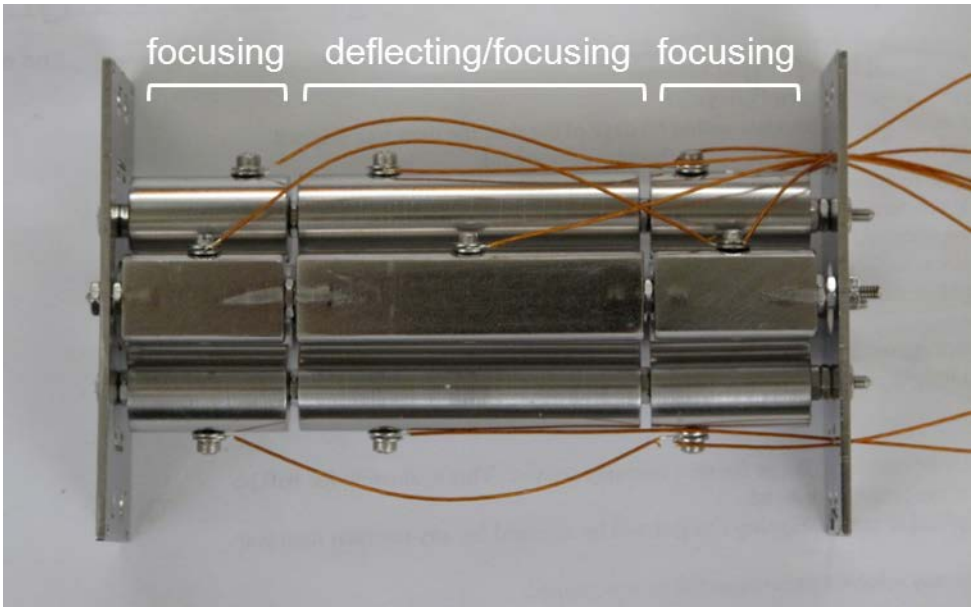

Figure 2.4 Side-view picture of refurbished Q2 quadrupole. The middle elements, which deflect the ion beam, are twice as long as the first and third elements used for focusing ions. The four horizontal poles on the first and third elements share a common voltage, as do the four vertical poles. The four middle deflecting poles each are supplied independent voltages. Therefore, there are six independent voltages used in each quadrupole assembly.

After the A2 aperture, the ions pass through the third set of deflectors (D3) which steer the ions into the Wien filter assembly. This assembly consists of the Wien filter and two quadrupoles (Q2 and Q3), pictured in Section 3.4. The Wien filter consists of perpendicular magnetic and electric fields, which are both orthogonal to the ion beam. Only ions with a unique velocity, where the forces of the electric and magnetic field balance, will pass through the filter undeflected. The current redesigned Wien filter was recently installed (early 2010), replacing the original filter that had been in use for nearly 40 years. Data presented in Chapters 6 and 7

used the new Wien filter, which has an improved mass resolution of approximately $m/\Delta m = 80$. The new Wien filter has two isolated faceplates with 5 mm apertures used to measure ion current entering and exiting the filter. Total ion current on the exit aperture (maximum current when ions are deflected onto plate) is typically between 5–10 nA. The details of the theory and function of the original and new Wien filters is presented in Chapter 3.

Ions undeflected by the Wien filter pass through the third quadrupole (Q3) and travel through a field free region before encountering a 2 mm aperture (A3). This aperture serves two functions: to separate ions that have been spatially dispersed by the Wien filter and to measure the ion current. The ability to measure ion current (typically 1–3 nA) on A3 is crucial to forming a focused ion beam in the interaction region and for troubleshooting when the ions are unstable or misguided. Selected ions pass through A3 and are focused and steered first by Q4 and then deflected by the last set of deflectors (D5) into the deceleration lens stack. Ions are decelerated to 35 V to both reduce the effects of Doppler broadening – which degrades the resolution of our electron energy analyzer – and to increase the anion residence time in the photodetachment region. The first and last lens elements in the deceleration lenses (D1 and D4) are maintained at a constant potential; D1 is at the ion beam voltage (735 V) and D4 is at the final decelerated potential (35 V). The second and third elements can be varied between 35 and 400 V to optimize the ion current at the interaction region as well as the photoelectron counts.

Once the ions are decelerated, they enter the interaction region where the ion beam is crossed perpendicularly with a laser beam. The ion current is measured on a carefully isolated Faraday cup, placed after the interaction region. The Faraday cup is sensitive enough to measure ion currents down to 1 pA, with typical O^- ion signals ranging between 500–1000 pA. Ion currents at A2, A3, and the Faraday cup are simultaneously measured (Keithley 600A and 602

electrometers) to provide information on the magnitude and focusing of the ion beam at difference points in the instrument. Operational pressures in the interaction region of ~10^{-9} Torr are maintained by two turbomolecular pumps (Varian 6 and 8 inch turbo pumps; 250 L sec^{-1} and 280 L sec^{-1}, respectively).

2.4 Ultraviolet Laser System

The decelerated ion beam is intersected by a fixed frequency laser beam in the interaction region. The design and operation of the laser system used has been described in great detail previously,[3, 5, 6, 15] and will be summarized below. Figure 2.5 illustrates the major components of the current laser system. We use an argon ion laser (Spectra Physics 2085-25) to obtain roughly 1 W of continuous fixed-frequency laser light at wavelengths of either 351 or 364 nm. The current laser recently replaced the previous laser (Spectra Physics 2045), but very few major changes were made between the new and previous systems and they will be treated as the same for this description.[††]

Our experiment requires a fixed frequency laser to determine the appropriate energy of the photodetached electrons, as shown in Equation 1.3. However, there are several lines of the argon ion laser that can lase, which span several hundred nanometers.[13] To produce light at a single frequency (of a single line in the laser), special attention much be paid to the optics used in the laser cavity. A custom high-reflective optic (0.25 in CVI Y3 mirror) is used as the back mirror; this optic has a coating that is highly reflective for light in a narrow range (80 nm bandwidth center around 355 nm). The other cavity mirror (a wavelength-selective output coupler) has a 10 nm bandwidth so only one line of the argon ion laser will be able to lase.

[††] The etalon now uses an automated heater unit to obtain single frequency operation, and a position-stabilizing feedback system was added to the output coupler mirror (which we deactivate when using our servo).

Different output couplers are used to select the specific UV line in the argon ion laser we wish to use, either 364 nm or 351 nm. Finally, an etalon is used to select one longitudinal mode in the gain profile of the selected laser line. We use a spectrum analyzer (Coherent, 300 MHz FSR) to ensure that only one mode is present in the output of the laser beam.

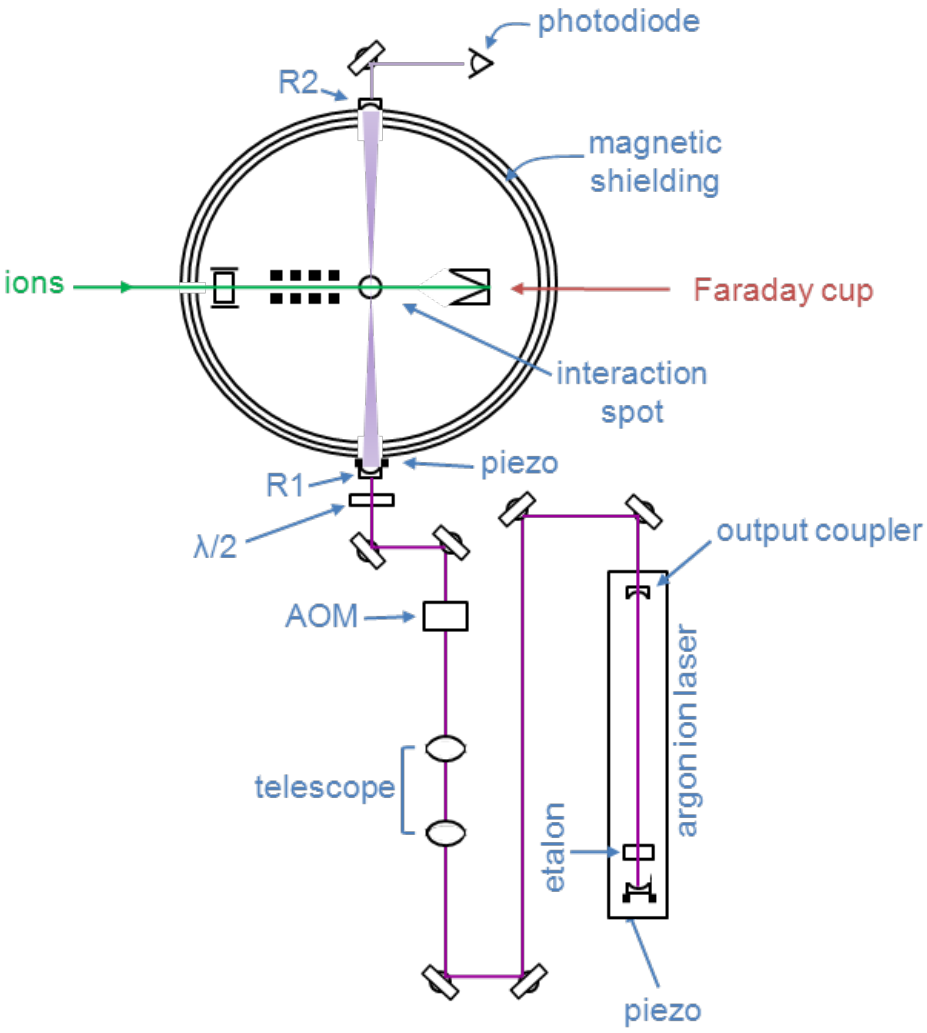

Figure 2.5 Schematic of the laser system illustrating the major components. The light from an argon ion laser is steered, focused, and manipulated before entering the vacuum chapter, which serves as an external build-up cavity. An AOM is used to shift and modulate the laser frequency while the half-waveplate rotates the laser polarization.

The laser light is coupled into an external build-up cavity that amplifies the power inside the interaction region by a factor of ~ 100. High circulating laser powers are necessary due to the low number density of ions in the interaction region and the small collection efficiency of our electron energy analyzer (see Section 2.5). The external build-up cavity is essentially a Fabry-Perot interferometer that is locked to resonance.[15] The condition for build up inside the vacuum chamber is that the resonant frequency of the laser and build-up cavity be exactly matched. However, the resonant frequencies of both the laser and build-up cavities will vary over the course of a day due to variables such as thermal drift, mechanical vibrations, and fluctuations in the laser plasma density. In order to keep the resonant frequencies matched, a custom servoamplifier system adjusts the lengths of both the laser and build-up cavities with piezoelectric discs mounted to the cavity mirrors.

A major component of the laser/servoamplifier system is an acousto-optic modulator (AOM) which is used to modulate the laser light. The AOM (Inter-Action model AOM 704) serves several important purposes. First, the AOM shifts the laser light by 50–80 MHz, which isolates the laser and build-up cavities and prevents light reflected off the build-up cavity mirror from returning to the laser cavity and causing interference. Second, the AOM can make very fast (> 5 kHz) adjustments to the laser frequency which the piezos cannot handle. Lastly, the AOM adds a 1 MHz dither onto the laser light which provides an error signal for the servoamplifier. Using this error signal, the servoamplifier can adjust the build-up cavity piezo, the laser cavity piezo, or the AOM frequency shift to maintain resonance conditions between the two cavities.[6]

Two other critical components in the laser system are the telescope and half-waveplate. The telescope is used to adjust the spatial mode parameters of the laser beam in order to match the diameter of the wave-front curvature of the build-up cavity TEM_{00} mode.[16] The half-

waveplate is used to rotate the polarization of the laser beam, which is required to obtain angular-dependent photoelectron spectra.

2.5 Photoelectron Energy Analysis and Detection

The laser and ion beams cross in the interaction region, where electrons are photodetached in all directions. Only the electrons that pass through a 5° solid angle cone (0.065" circular aperture, 3/8" away from the interaction spot) are collected; this represents less than 0.2% of the ejected electrons. Figure 2.6 shows a cross-sectional view of the electron energy analyzer and the interaction region. Electrons that pass through the acceptance aperture are then accelerated and focused into the hemispherical energy analyzer. The hemispherical analyzer is made of two concentric hemispheres, which provides a radial electric field that disperses the electrons spatially at the analyzer's output according to the electron's kinetic energy.[4] The analyzer is operated at constant transmission energy (presently ~ 4 eV), which defines the energy an electron must have to successfully pass through the hemispheres. Photodetached electrons will have kinetic energies ranging from 0 eV to the photon energy (~ 3.5 eV). Therefore, in order to pass through the analyzer and be detected, the electrons must be accelerated to the transmission energy. This is accomplished by a series of cylindrical input lenses (V_{IR}, V_1, V_2, V_{HC}). The first three lenses (V_{IR}, V_1, and V_2) together form a zoom lens which accelerates the ions. A second zoom lens is formed by V_2, V_3, and V_{HC}, which serves to focus and accelerate the electrons to the transmission energy. The lenses at the entrance and exit of the hemispheres are Herzog correction lenses (V_{HC}), which help prevent any fringe fields from entering the hemispheres. The voltages applied to the input lenses, and the inner and outer hemispheres are determined by simple relationships to the kinetic energy of electrons that are

selected to be transmitted through the analyzer and the transmission energy; this is described in detail in Feigerle's thesis.[4]

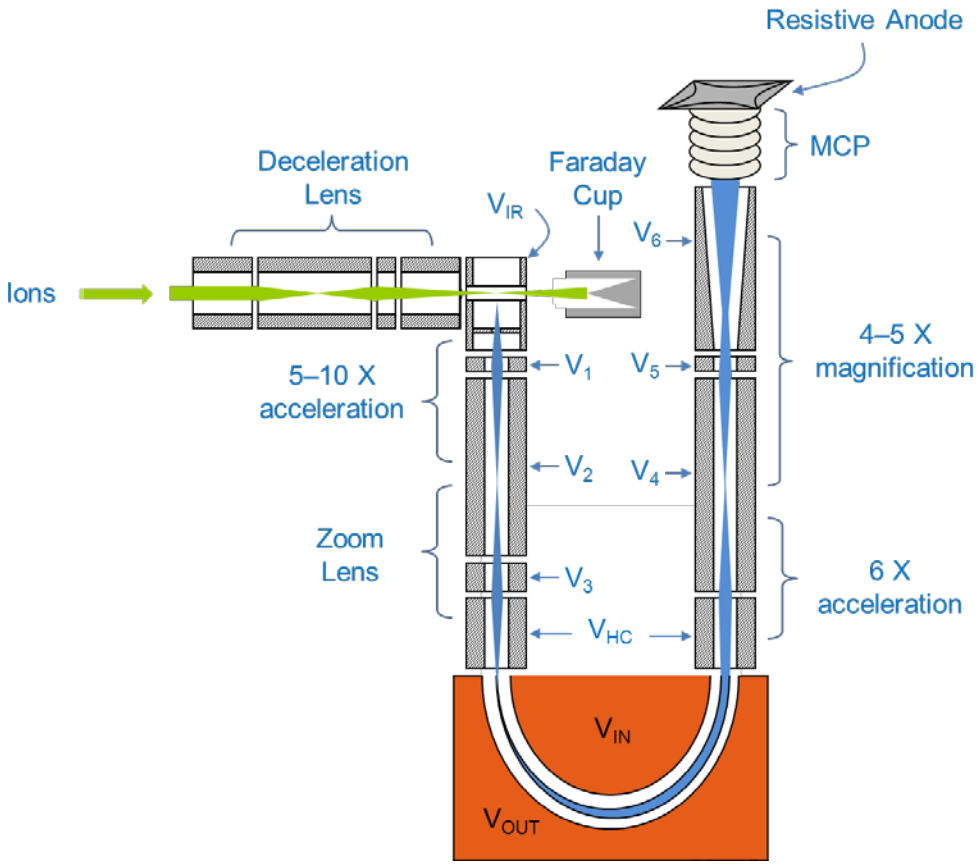

Figure 2.6 Cross-sectional view of the electron energy analyzer and the interaction region.

Electrons that enter the hemispheres will experience different forces depending on their energy and spread out spatially, with high-energy electrons passing near the outer hemisphere and low-energy electrons traveling near the inner hemisphere. If the electron kinetic energy is too little or high, it will have a trajectory that will cause it to collide with the hemispheres, and will not be detected. Electrons within 2% of the transmission energy will be transmitted through the analyzer, which is ~ 100 meV for the current transmission energy. In this manner, the

photoelectron spectrum is obtained by collecting overlapping 100 meV segments of electrons at a time by varying the voltages on the input lens stack and allowing electrons of different energies to be transmitted. The energy dispersed electrons are then accelerated and focused onto a position sensitive detector that includes a stack of five mircochannel plates coupled to a resistive anode. The position sensitive detector is a two-dimensional array that correlates the electron impact position with a specific kinetic energy. The detector is divided into 256 channels in the energy dispersion direction, the x-axis, and 16 channels in the y-axis, which corresponds to electron counts (or impact events). The data in the 16 channels that correspond to counts are simply integrated to produce an integer number of counts per channel in the x-direction. Electrons with kinetic energies less than about 0.3 eV are not detected very efficiently due to the effects of stray fields and degraded resolution.

2.6 Data Acquisition and Analysis

The position sensitive detector is coupled to an external position analyzer (Quantar Technology 2401B), which analyzes the raw data from the resistive anode and determines the position of the detected electron. The position analyzer sends the processed signals to a PC computer which collects and stores the data. The analyzer is also connected to an oscilloscope where real-time signals of the electron impact position on the detector can be monitored. Details of how the position analyzer interfaces with the position sensitive detector and the PC computer is outlined in Ramond's thesis.[7] A custom LabVIEW program is used to interface and coordinate with the position analyzer to collect data. This program also communicates with a voltage programmer (JILA L036), which controls the voltages in the hemispherical analyzer assembly.

The raw data that are stored in the computer (counts versus detector channel) must be calibrated and converted from detector position into an absolute electron kinetic energy scale. This is done by measuring the photoelectron spectrum of an atomic system with well-known energy transitions. In our case, it is convenient to use O^- because it is present as a precursor in our ion source and the electron affinity of neutral oxygen atom, EA(O) = 1.46111 eV, is precisely known.[17] This calibration is performed several times throughout the day, generally before and after acquiring data sets. There is also a slight nonlinearity of the kinetic energy analyzer scale that must be corrected for; this is typically performed whenever there are major adjustments of the laser beam position. A kinetic energy compression factor, which is an empirical correction to the relative energy scale, is made by measuring energy of well-known transitions of either tungsten (W^-) or oxygen (O_2^-) anions.[3] A correction, which is dependent on the transmission energy, of less than 1% is generally observed.

2.7 Ab initio Calculation and Franck-Condon Simulation

Electronic structure calculations have proven to be a valuable, and often necessary, component of assigning and interpreting photoelectron spectra. Most of the calculations presented in this thesis use the B3LYP method of density functional theory (DFT)[18, 19] with basis sets ranging from modest (6-311++G(d,p)) to more sophisticated (aug-cc-pVTZ). We often use this DFT method as it has been shown to yield reliable frequencies and is computationally efficient for large molecules.[20, 21] The GAUSSIAN 03 program package[22] is used to obtain optimized equilibrium molecular geometries, harmonic vibrational frequencies, and vibrational normal coordinates for both the anion and corresponding neutral.

In order to simulate the photoelectron spectrum of an anion, the Franck-Condon factors (FCF) for all allowed vibronic transitions must be determined. The expression for determining the FCF, derived in Chapter 1, is

Equation 2.1

$$\mathrm{FCF} = \left|\left\langle \psi_{v''}(Q'') \middle| \psi_{v'}\left(Q'\right)\right\rangle\right|^2$$

where $\psi_{v''}\left(Q''\right)$ is the multidimensional wavefunction in quantum state v'' ($v'' = v_1'', v_2'', \ldots, v_n''$) as a function of the normal coordinates of the anion Q'', and $\psi_{v'}\left(Q'\right)$ is the corresponding vibrational wavefunction of the neutral in terms of its normal coordinates Q'.[2] In order to complete the integration in Equation 2.1, the wavefunctions must be expressed in terms of the same coordinates for both states. This can be accomplished by using the Duschinsky transformation[23], which expresses the normal mode coordinates of the neutral in the basis set of the normal mode coordinates of the anion. The transformation between the normal coordinates ($Q''$and Q') is given by

Equation 2.2

$$\mathbf{Q}'' = \mathbf{J}''\mathbf{Q}' + \mathbf{K}''$$

where $\mathbf{J}''$is the Duschinsky rotation matrix and $\mathbf{K}''$is a vector of geometry displacements given in the basis of the normal coordinates of the anion.[2] The Duschinsky rotation matrix accounts for the vibrational mixing of the normal modes that result from a relative rotation of the normal coordinates between the anion and neutral states.[24] In order to determine $\mathbf{J}''$and $\mathbf{K}''$, a Fortran program (FCFGAUS) is used to extract the calculated normal coordinate vectors and geometries from the electronic structure calculations. Another Fortran program (PESCAL[25]) uses the output files from FCFGAUS to calculate the Franck-Condon factors. PESCAL uses the Sharp-

Rosenstock-Chen method in the harmonic oscillator approximation including Duschinsky rotations.[26] The raw FCFs are sorted according to their energies and then convoluted with a Gaussian lineshape representative of the experimental resolution (~ 10 meV).

Using only the results from the electronic structure calculation, one can simulate the photoelectron spectrum that is independent of experimental observations. However, it is often the case that some experimental data has previously been determined (vibrational frequencies, vibrational anharmonicities, electron affinity, and geometries), which can be inputted into PESCAL when simulating the spectrum. We generally include the experimental vibrational frequencies of active modes and the position of the origin peak (the EA) in the simulation if they can be determined from the photoelectron spectrum. PESCAL also has a nonlinear least-squares optimization procedure that can be used to fit the experimental spectrum. The values for the anion and neutral vibrational constants, geometries, the electron affinity, the anion vibrational temperature, and a scaling factor for the relative intensity are used as adjustable parameters which are optimized to minimize the differences between the simulated and experimental spectra.

Many molecular systems studied in our lab have excellent agreement between experiment and simulated spectra.[2, 27-31] However, the type of normal mode analysis described above can be insufficient for systems that have a large change in geometry between the anion and neutral states or when there are non-adiabatic effects present.[32-35] In these cases, a more tailored and sophisticated treatment is required, with several examples presented in Chapters 6 and 7 in this thesis.

2.8 References

1. Brehm, B., M.A. Gusinow, and J.L. Hall, *Electron affinity of helium via laser photodetachment of its negative ion.* Physical Review Letters, 1967. **19**(13): p. 737-&.
2. Ervin, K.M., J. Ho, and W.C. Lineberger, *Ultraviolet Photoelectron-Spectrum of NO_2.* J. Phys. Chem., 1988. **92**(19): p. 5405-5412.
3. Ervin, K.M. and W.C. Lineberger, in *Advances in Gas Phase Ion Chemistry*, N.G. Adams and L.M. Babcock, Editors. 1992, JAI: Greenwich. p. 121.
4. Feigerle, C.S., in *JILA* 1983, University of Colorado: Boulder.
5. Ho, J., in *Chemistry* 1992, University of Colorado: Boulder.
6. Gunion, R.F., *Ultraviolet Photoelectron Spectroscopy of Molecular Anions*, in *Department of Chemistry* 1995, Boulder: Boulder. p. 275.
7. Ramond, T.M., *Negative Ion Photoelectron Spectroscopy of Alkyl Peroxides, Alkoxides, and Group VIII Transition Metal Oxides*, in *Chemistry*2001, University of Colorado: Boulder.
8. Fehsenfe.Fc, K.M. Evenson, and H.P. Broida, *Microwave discharge cavities operating at 2450 MHz.* Review of Scientific Instruments, 1965. **36**(3): p. 294.
9. Leopold, D.G., et al., *Methylene: A study of the $X\ ^3B_1$ and $a\ ^1A_1$ states by photoelectron spectroscopy of CH_2^- and CD_2^-.* J. Chem. Phys., 1985. **83**(10): p. 4849.
10. Lee, J. and J.J. Grabowski, *Reactions of the Atomic Oxygen Radical Anion and the Synthesis of Organic Reactive Intermediates.* Chem. Rev., 1992. **92**(7): p. 1611.
11. Jennings, K.R., *Negative Ions.* Philosophical Transactions of the Royal Society of London. Series A, Mathematical and Physical Sciences, 1979. **293**(1400): p. 125-133.
12. DePuy, C.H., V.M. Bierbaum, and R. Damrauer, *Relative gas-phase acidities of the alkanes.* Journal of the American Chemical Society, 1984. **106**(14): p. 4051-4053.
13. Moore, J.H., C.C. Davis, and M.A. Coplan, *Building Scientific Apparatus*. Third ed2003, Boulder: Westview Press. 654.
14. Marynowski, M., W. Franzen, and M. Elbatanouny, *Analysis of the properties of an electrostatic triplet quadrupole lens used as an electron-beam transport device E.* Review of Scientific Instruments, 1994. **65**(12): p. 3718-3723.
15. Ervin, K.M., J. Ho, and W.C. Lineberger, *A Study of the Singlet and Triplet-States of Vinylidene by Photoelectron-Spectroscopy of $H_2C{=}C^-$, $D_2C{=}C^-$, and $HDC{=}C^-$ - Vinylidene Acetylene Isomerization.* J. Chem. Phys., 1989. **91**(10): p. 5974-5992.
16. Kogelnik, H. and T. Li, *Laser beams and resonators.* Applied Optics, 1966. **5**(10): p. 1550.
17. Neumark, D.M., et al., *Laser photodetachment measurement of the electron-affinity of atomic oxygen.* Phys. Rev. A, 1985. **32**(3): p. 1890.
18. Becke, A.D., *Density-functional thermochemistry. III. The role of exact exchange.* Journal of Chemical Physics, 1993. **98**(7): p. 5648-5652.

19. Lee, C.T., W.T. Yang, and R.G. Parr, *Development of the colle-salvetti correlation-energy formula into a functional of the electron density.* Physical Review B, 1988. **37**(2): p. 785-789.

20. Wong, M.W., *Vibrational frequency prediction using density functional theory.* Chemical Physics Letters, 1996. **256**(4-5): p. 391-399.

21. Halls, M.D., J. Velkovski, and H.B. Schlegel, *Harmonic frequency scaling factors for Hartree-Fock, S-VWN, B-LYP, B3-LYP, B3-PW91 and MP2 with the Sadlej pVTZ electric property basis set.* Theoretical Chemistry Accounts, 2001. **105**(6): p. 413-421.

22. Frisch, M.J., et al., *Gaussian 03, Revision B.05*2003, Pittsburgh: Gaussian, Inc.

23. Duschinsky, F., *The importance of the electron spectrum in multi atomic molecules. concerning the Franck-Condon principle.* Acta Physicochimica Urss, 1937. **7**(4): p. 551-566.

24. Muller, C.W., et al., *Duschinsky mixing between four non-totally symmetric normal coordinates in the S-1-S-0 vibronic structure of (E)-phenylvinylacetylene: a quantitative analysis.* Physical Chemistry Chemical Physics, 2010. **12**(10): p. 2331-2343.

25. Ervin, K.M., *PESCAL, Fortran program.* PESCAL, Fortran program, 2010.

26. Sharp, T.E. and H.M. Rosenstock, *Franck-condon factors for polyatomic molecules.* Journal of Chemical Physics, 1964. **41**(11): p. 3453.

27. Ervin, K.M., et al., *The Only Stable State of O_2^- Is the $X\ ^2P_g$ Ground State and It (Still!) Has an Adiabatic Electron Detachment Energy of 0.45 eV.* J. Phys. Chem. A, 2003. **107**(41): p. 8521.

28. Ervin, K.M., et al., *Naphthyl radical: Negative ion photoelectron spectroscopy, Franck-Condon simulation, and thermochemistry.* J. Phys. Chem. A, 2001. **105**(48): p. 10822.

29. Villano, S.M., et al., *Photoelectron Spectroscopy and Thermochemistry of the Peroxyformate Anion.* Journal of Physical Chemistry A, 2010. **114**(1): p. 191-200.

30. Wren, S.W., et al., *The photoelectron spectrum of CCl_2^-: the convergence of theory and experiment after a decade of debate.* Physical Chemistry Chemical Physics, 2009. **11**(23): p. 4745-4753.

31. Vogelhuber, K.M., et al., *The C-H bond dissociation energy of furan: Photoelectron spectroscopy of the furanide anion.* Journal of Chemical Physics, 2011. **134**(6).

32. Bopp, J.C., et al., *Spectroscopic characterization of the isolated SF_6^- and $C_4F_8^-$ anions: Observation of very long harmonic progressions in symmetric deformation modes upon photodetachment.* Journal of Physical Chemistry A, 2007. **111**(7): p. 1214-1221.

33. Gianola, A.J., et al., *Thermochemical studies of pyrazolide.* J. Phys. Chem. A, 2006. **110**(27): p. 8457.

34. Vogelhuber, K.M., et al., *Photoelectron spectra of dihalomethyl anions: Testing the limits of normal mode analysis.* The Journal of Chemical Physics, 2011. **134**(18): p. 184306-13.

35. Ichino, T., et al., *The vibronic level structure of the cyclopentadienyl radical.* Journal of Chemical Physics, 2008. **129**(8).

3 Wien Velocity Filter: New Mass Filter

3.1 Introduction

One of the defining advantages of studying charged particles in the gas phase is the ability to control the trajectory of ions with applied electric and magnetic fields. The forces on the charged particles from the external fields can additionally be used to separate ions based on their mass-to-charge ratio. Being able to filter anions based on their mass is a powerful tool which allows us to select one specific anion from the mixture of ions created in our source region. This ability to select an individual anion is critical for our experiment, and limited resolution of the mass filter will likely be detrimental to our measurements.

There are several techniques widely used for filtering a beam of ions, namely magnetic sector mass analyzers, RF quadrupole mass analyzers, linear time-of-flight mass spectrometers, and Wien filters.[1, 2] Determining which technique to use depends largely on whether the ion beam is pulsed or continuous, and the type of experiment, mass range and resolution required, and method of detection that will be employed. Our experiment requires a filter that has high transmission allowing a relatively large current from a focused ion beam (10^{-9} – 10^{-12} A) to reach the laser interaction region due to the low collection efficiency of our energy analyzer. We also need moderate mass resolutions ($m/\Delta m \sim 40$) in order to separate small anions (roughly 40 amu) that only differ by 1 amu – specifically the loss of a proton. The Wien velocity filter meets the above requirements and has the additional advantage of producing an undeflected beam of selected anions. However, after over thirty years of dutiful service and several rebuilds, the Wien filter in our apparatus was not functioning as designed, which caused the instrument to

show badly degraded performance. After careful consideration, we decided to redesign the original Wien filter in order to improve its resolution and address structural issues present in the current filter. First, it is necessary to understand the theory of operation behind the Wien filter, which is discussed in Section 3.2.

3.2 Theory of Wien Velocity Filter

The Wien filter employs external electric and magnetic fields that are perpendicular to each other, which in turn are both normal to the ion beam trajectory as schematically shown in Figure 3.1. All the ions created in the source region are accelerated to 735 V by a series of electrostatic lenses and thus have the same nominal kinetic energy.

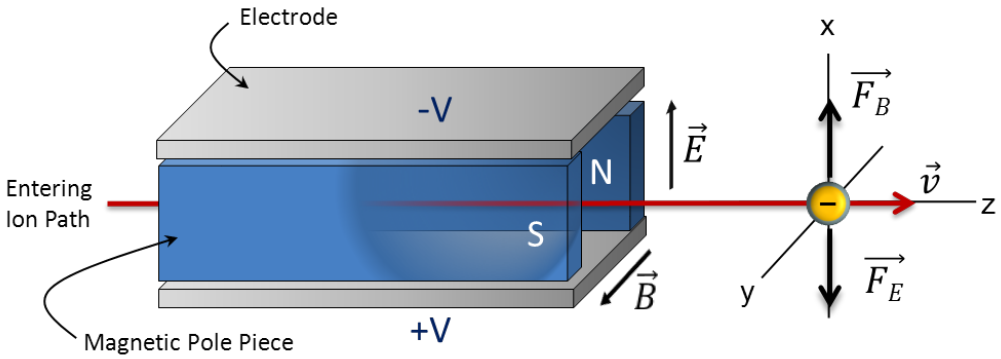

Figure 3.1 Schematic of Wien filter depicting the directions of the electric and magnetic fields, as well as the forces on the anion as it passes through the filter.

Therefore, mass selecting the ions is the same as selecting the ions based on their velocity – hence the term Wien velocity filter. The magnitude of the velocity of a particular ion can then be written as

Equation 3.1

$$v_0 = \sqrt{\frac{2E}{m_0}}$$

where E is the kinetic energy of the ion and m_0 is the mass of the particular ion that we wish to select. Since E is determined by the potential difference (V) of the electrostatic lens on the anion, we can rewrite Equation 3.1 as

Equation 3.2

$$v_0 = \sqrt{\frac{2eV}{m_0}}$$

where e is the net charge (q = |e|) of the anion.

An anion traveling through the Wien filter with velocity v_0 will experience opposing forces from the electric and magnetic fields; the Coulomb force ($\overrightarrow{F_E}$) and the Lorentz force ($\overrightarrow{F_B}$) respectively. The Coulomb force is given by Equation 3.3,

Equation 3.3

$$\overrightarrow{F_E} = e\vec{E}$$

and is dependent on the charge of the ion and the electric field, which in turn is governed by the potential difference between the electrodes in the Wien filter. The Lorentz force is given by Equation 3.4,

Equation 3.4

$$\overrightarrow{F_B} = e\vec{v} \times \vec{B}$$

In order for an anion to pass undeflected through the Wien filter, the forces from the electric and magnetic fields must be balanced. Mathematically, this condition is met when the forces described by Equation 3.3 and Equation 3.4 are equal and opposite, shown below

Equation 3.5

$$e\vec{E} = e\vec{v} \times \vec{B}$$

Substituting the expression derived for the ion velocity in Equation 3.2, and solving for the magnitude of the magnetic field,

Equation 3.6

$$B = E\sqrt{\frac{m_0}{2eV}}$$

to obtain Equation 3.6. Physically, this means that for a particular electric and magnetic field strength, only one unique m_0 will traverse through the Wien filter undeflected. Experimentally, we can control the magnitude of both E and B but we choose to keep the electric field constant and vary the magnetic field to select a desired anion.

For anions that have masses (m_x) where the forces from the electric and magnetic fields are not balanced, they will experience a centripetal force ($\vec{F}_C$) given by

Equation 3.7

$$\vec{F}_C = \vec{F}_B - \vec{F}_E$$

We can rewrite Equation 3.7 using the definition of centripetal force and Equation 3.3 and Equation 3.4

Equation 3.8

$$\frac{m_x {v_x}^2}{R} = ev_xB - eE$$

where R is the radius of the circular path that ions with mass m_x will be deflected. We can further simplify Equation 3.8

Equation 3.9

$$\frac{m_x v_x^2}{R} = eE\left[\sqrt{\frac{m_0}{m_x}} - 1\right]$$

and then set Equation 3.9 equal to R

Equation 3.10

$$R = \frac{2V}{E\left[\sqrt{\frac{m_0}{m_x}} - 1\right]}$$

Equation 3.10 is approximately correct as long as deflection angles are small.[3]

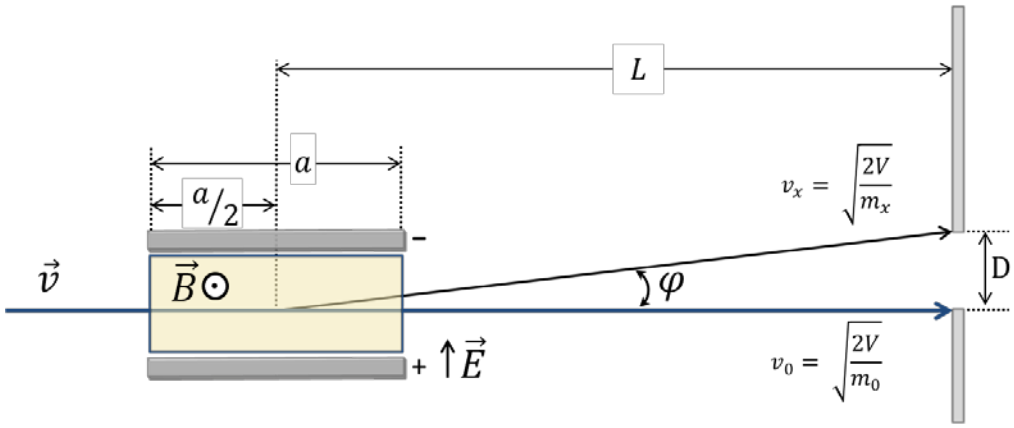

Figure 3.2 Schematic diagram defining the physical parameters of the Wien filter.

Figure 3.2 schematically defines the relevant physical parameters of the Wien filter and illustrates how ions with mass m_x are dispersed and separated compared to undeflected ions with mass m_0. Ions with mass of m_x are deflected by φ, assuming φ is small, in which case the deflection angle can be approximated as

Equation 3.11

$$\varphi = \frac{a}{R}$$

where a is the length over which the electric and magnetic fields act on the ion, which is effectively the length of the electrode and magnet pole pieces (~200 mm in our filter design). It should also be noted that in defining a, all fringe fields (electric and magnetic) are assumed to be

negligible. Equation 3.11 can be rewritten by inserting the expression for R determined in Equation 3.10 to obtain

Equation 3.12

$$\varphi = \frac{aeE}{2V}\left[\sqrt{\frac{m_0}{m_x}} - 1\right]$$

Finally, we can relate the dispersion angle (φ) to the separating power of the Wien filter by considering the distance the ions travel before encountering an aperture with diameter D

Equation 3.13

$$D = L\varphi = \frac{aLeE}{2V}\left[\sqrt{\frac{m_0}{m_x}} - 1\right]$$

where L in our apparatus is the distance from the center of the Wien filter to aperture D. We can further simplify Equation 3.12 to obtain

Equation 3.14

$$D \cong \frac{aLe\vec{E}}{4V}\frac{\Delta m}{m_0}$$

which can be rearranged to obtain an expression for the mass resolution of the mass filter, $m_0/\Delta m$

Equation 3.15

$$\frac{m_0}{\Delta m} \cong \frac{aL\vec{E}}{4DV}$$

We can then calculate the theoretical limit for the mass resolution of our Wien filter, as all the values in Equation 3.15 are known. With a = 200 mm, L = 500 mm, E = 130 V cm^{-1}, D = 2 mm, and V = 735 V, the calculated resolution is then ~ 220. The values of E can be linearly scaled to higher field strengths, which will in principle increase the mass resolution.

3.3 Previous Wien Filter Design

Equation 3.15 provides a simple mathematical relationship of how changing the electric field strength, aperture size, Wien filter size, distance to aperture, and ion beam energy affect the mass resolution. Even though the calculated $m_0/\Delta m$ is over 200 in our apparatus, in practice the best resolution we had achieved in recent years with the previous filter was far below this value, and closer to 40 under the best experimental conditions. However, often the resolution was much lower than 40, which greatly limited the ions we could study when we needed to separate ions differing by 1 amu. To better understand why the Wien filter was failing to operate, it is necessary to look at the previous Wien filter's design.

The design of the original Wien filter in our apparatus has been documented in detail in the original paper by Wahlin[3] and later in the thesis of Gunion.[4] The horizontal magnetic field is provided by an external electromagnet that magnetizes iron pole pieces inside the vacuum system that act to concentrate the field. Two electrostatic deflector plates (electrodes) create the vertical electric field. Between the deflector plates and the magnetic pole pieces are pairs of parallel stainless steel shims (parallel to both the positive and negative electrodes), which are insulated from each other by Teflon shims. A simplified diagram is shown in Figure 3.3 to illustrate the main components of the Wien filter.

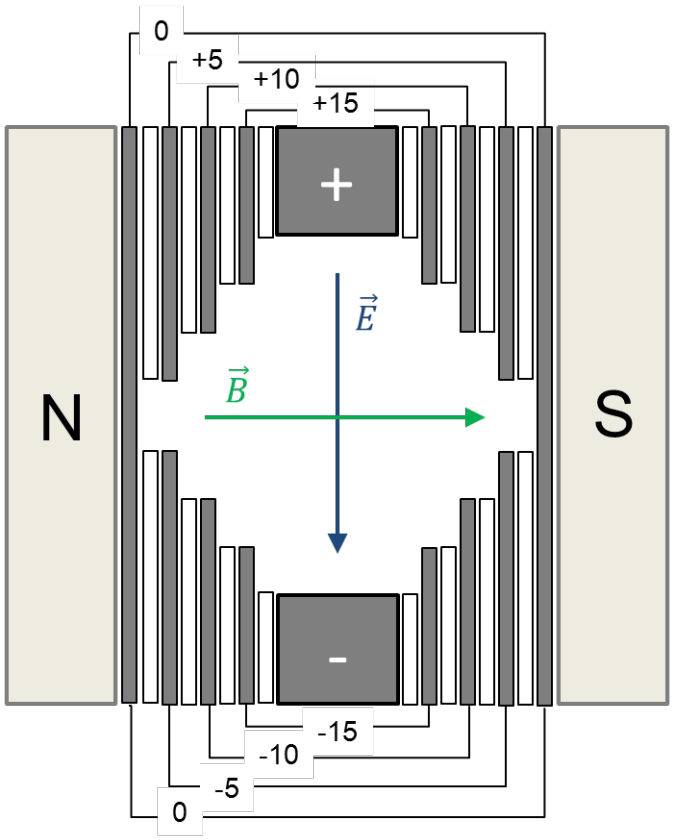

Figure 3.3 Simplified diagram of the Wien filter construction. Magnetic pole pieces in the Wien filter assembly are magnetized by an external electromagnet and provide a horizontal electric field. The electrostatic deflectors (electrodes) provide the electric field. Pairs of stainless steel shims (dark grey) separated by Teflon (white) are used to simulate infinite parallel plates and eliminate fringe fields. The voltage on the shims is decreased stepwise moving away from the electrodes while the distance between the opposite polarity shim decreases. This maintains the same electric field while decreasing the potential between the plates to the ion beam voltage. The voltages shown are an example of the stepwise decrease if the electrodes were at +20 V and -20 V where 0 is the ion beam voltage.

In Figure 3.3, the potential voltage on the electrodes is +20 V and -20 V relative to the ion beam voltage; thus, the potential difference between the electrodes is 40 V with a zero point at a distance halfway between the plates. The steel shims are used to help reduce the presence of fringe fields that would result at the edges of the electrodes if the potential suddenly dropped from the electrode voltage to ground. Instead, the voltage on the shims is stepped down from the

electrode voltage in small increments to the voltage of the ion beam (735 V), while the distance between the shims with equal voltage but opposite polarity (i.e. +15 and -15 shims directly across from each other in Figure 3.3) is decreased. This design is an attempt to create a uniform electric field which would resemble infinite parallel plates with a constant potential difference. Figure 3.4 illustrates the difference between finite and infinite electrode plates where inhomogeneous electric fields are created by fringe fields in the former case. The voltages on the shims can be varied using an external home-built voltage divider. In the example in Figure 3.3, the voltage on the electrodes is +20 V and -20 V (+755 V and +715 V taking into account the ion beam float voltage of 735 V) which is then stepped down by 5 V until reaching 0 V.

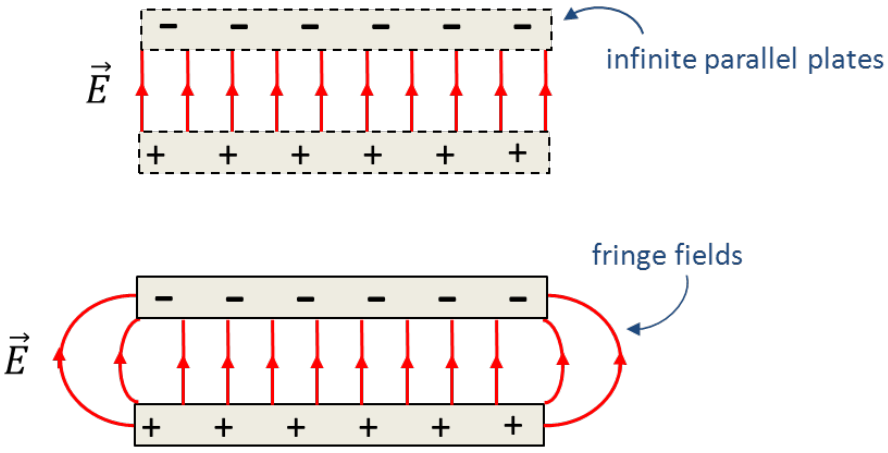

Figure 3.4 Schematic of electric field between two electrodes (parallel plates). The top example is the ideal case where the plates extend to infinity and there is a uniform electric field between the plates. The bottom example shows how fringe fields develop at the edges of electrodes creating an inhomogeneous electric field.

The actual construction of the original Wien filter was quite complicated and intricate. The entire unit was held together by a press fit where the magnetic pole pieces are attached to two cap sections to hold the electrodes and shims together in place. The entire Wien filter

assembly, including Q2 and Q3, fit inside a long rectangular housing with very tight tolerances. This has led to severe galling in the past where there is metal-metal contact between the housing and the Wien filter if great care was not taken when servicing the filter. The voltage to each of the pairs of shims (both positive and negative), as well as the electrodes, was made using spot-welded thin wires insulated with delicate ceramic tubing. Therefore, disassembling the Wien filter and accessing the shims was very tedious and time–consuming.

It is critical that all components of the Wien filter stay electrically isolated from one another in order for proper operation. However, over the course of servicing the Wien filter and several repairs over the years, nearly half of the shims were shorted creating inhomogeneous fields inside the filter. All efforts to isolate the shims failed and we were left with the decision to either undertake a major rebuild of the filter to isolate the shims, or devise a new way to eliminate fringe fields. We decided to completely redesign the Wien filter and eliminate the steel shims, while keeping the physical dimensions of the filter the same.

3.4 New Wien Filter Design

The new Wien filter employs the same crossed electric and magnetic fields to separate the ion beam, but has significant changes intended to make the electric field more uniform and increase the ease of service of the Wien filter. The distinguishing difference between the two filters is changing the stepped electric field associated with the shim plates to, essentially on with an infinite number of shim plates. This is accomplished by replacing the steel shims with two silicon coated pieces of glass that separate the magnetic pole pieces and the electrodes, shown schematically in Figure 3.5. These coated glass plates are electrically connected to the two electrodes, but have a very high sheet resistance so only a small current (approximately 100 μA) is drawn. This provides a uniform potential gradient across the plate which, in conjunction with

the electrodes, provides a uniform electric field inside the Wien filter. The new filter also uses non-metallic material in its design (see Figure 3.6), which act to prevent galling between the Wien filter casing and the chamber housing. Additionally, new isolated apertures have been added to monitor and measure ion current before and after the Wien filter. These design changes result in a mass filter that is simpler, with fewer connections and components, which has dramatically improved performance over the previous design.

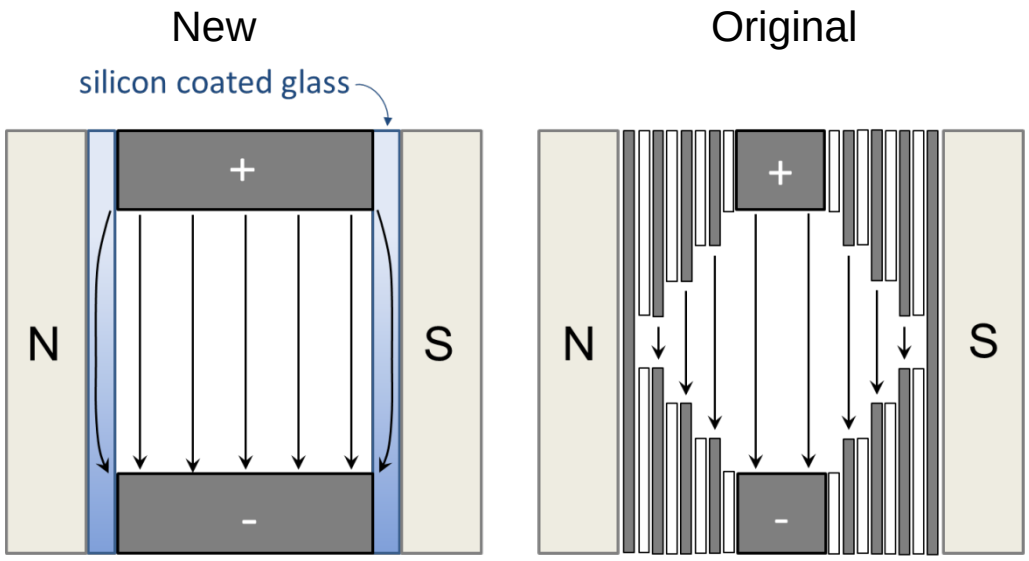

Figure 3.5 Schematic illustrating the difference of the new (left) and previous (right) Wien filter. The new Wien filter employs larger electrodes which are directly connected to silicon coated glass which acts as a high–resistance conductor creating a potential gradient between two electrodes. The curved arrows through the glass indicate the current flow through the silicon film on the glass.

In the deciding how to redesign the Wien filter, we looked at other methods for creating homogenous fields inside the ion flight path. Steel shims have been used to reduce fringe fields since the Wien filter was invented, though other designs have been suggested.[3, 5-8] The idea of using a material with high sheet resistivity that conducts a small electrical current is not new,[8]

but its implementation has presented technical challenges which made construction difficult. The desired material or coating needs to have a high sheet resistance[**] ($\geq$ 10 MΩ/sq) that is extremely uniform over the entire surface and is compatible with a high vacuum environment. There are very few conductive materials that have a sheet resistance this large that can withstand our experimental conditions. Initially, a coating of indium tin oxide (ITO) was deposited on glass plates using electron beam physical vapor deposition in the JILA special techniques laboratory. However, in order to achieve the proper resistivity, the coating thickness was too thin and easily scratched off. The material that best met our requirements was silicon deposited on glass using the same technique. Close attention was paid to ensure the thin film of silicon was uniform since the thickness of the film directly correlates to the local resistance. If the resistance varied over the coating, the potential gradient would also vary causing inhomogeneous fields in the filter.

We characterized the coatings using two spectroscopic techniques: UV-Visible spectra to investigate uniformity of the coatings, and ellipsometry to determine the approximate thickness of the film. The silicon coatings were thin enough that we could use a UV-Visible spectrometer to make transmission measurements on specific regions of the coated glass and observe how the absorption varied across the plates. A mask was used to limit the region of the slide that was probed to a 2 mm by 3 mm rectangle. If there was a large difference in thickness of the silicon film, it would be reflected in the UV-Visible spectra as an increase or decrease in the percent transmission. Spectra for a particular slide(s) in a single deposition run varied by less than 5%, which is consistent with a uniform coating. However, the spectra did vary for slides coated in different batches, which is to be expected. Therefore, the slides that were used in the Wien filter

[**] The sheet resistance (R_S) is a measure of the resistance across a thin film of uniform thickness and is analogous to resistivity used in three-dimensional systems. To calculate RS, bulk resistance is multiplied by ratio of the dimensions of the film area: $R_s = (W/L)\,R$. Sheet resistance has the units of Ω/sq.

were deposited at the same time under identical conditions. The ellipsometry measurements were also made over several localized regions of the final coated plates. The results and corresponding fits indicated that there was a uniform coating of approximately 400 nm of silicon.

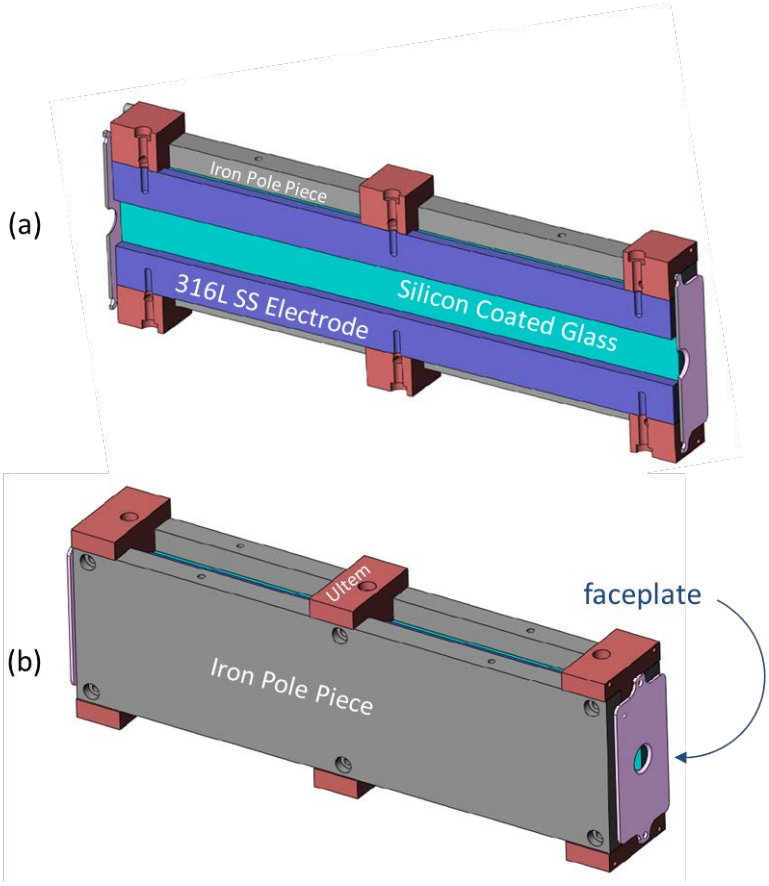

Figure 3.6 Schematic of the new Wien filter assembly. A cross section in shown in (a) highlighting the electrodes and the silicon coated glass. The entire assembled filter is shown in (b). The two faceplates at the entrance and exit of the Wien filter are optional and can be easily removed. Four identical faceplates with varying apertures (4, 5, 6, 7 mm) were made in to allow for adjustments and optimization of the Wien filter's performance

In order to make a robust connection between the silicon coated glass and the electrodes, two half-inch strips of gold were deposited (using the same deposition method as described above for the silicon) on top of the silicon coating where the two electrodes made contact with the glass.

Figure 3.6 schematically shows the fully assembled Wien filter (b) as well as a cross-section to highlight the electrodes and the coated glass (a). The electrodes are made from bead-blasted nonmagnetic 316L stainless steel. The steel was bead blasted as a precautionary measure to help limit any deflected ions from grazing the electrode surface and re-entering the selected ion beam. Both the iron plates and the electrodes are attached to the six Ultem blocks with screws. Ultem is a rigid polyetherimide polymer with low outgassing properties ideal for application in high vacuum. The coated glass is sandwiched between the electrode and the iron with a pressure fit holding the glass in place. In order to not put an excessive amount of stress on the glass, small squares of Buna rubber was inserted between the glass and the iron to act as a cushion. The electrical connections to the electrodes, faceplate, and to the iron (to float at the ion beam voltage) were provided with insulated wires (MDC coaxial single strand KAP 3 wire) which were connected with a steel fastener. The new assembled Wien filter with quadrupoles attached is shown in Figure 3.8a. A top view of the Wien filter is shown in Figure 3.8b, which shows the electrical connections to the elements in the filter.

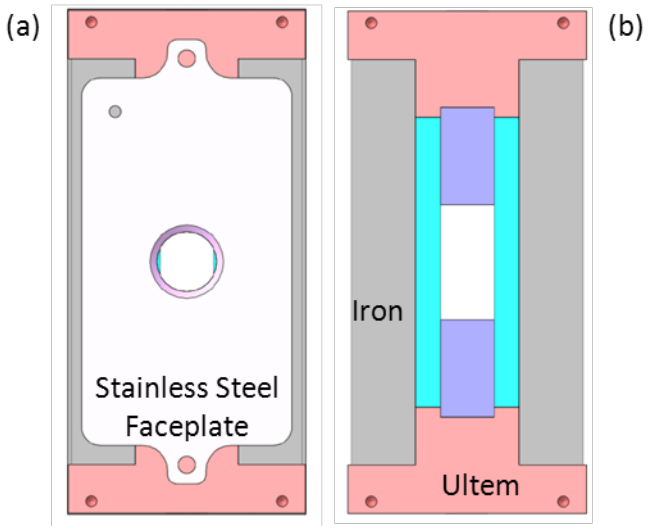

Figure 3.7 Schematic looking down the ion beam path of the Wien filter, shown with (a) and without (b) the faceplates. Besides being an aperture plate to measure the incoming and exiting ion current, the faceplate also acts to shield the ion beam from the edges of the glass plates.

The new Wien filter also has two isolated steel faceplates at the entrance and exit of the filter. These plates serve several important functions and are shown in more detail in Figure 3.7. First, the plates allow us to measure the ion current entering and exiting the Wien filter which is very useful in determining how the filter is functioning. Second, the aligned apertures also help ensure the ions enter and exit the filter on center. Lastly, the entrance faceplate acts to shield the ion beam from the edges of the glass plates, which is not at the beam voltage.

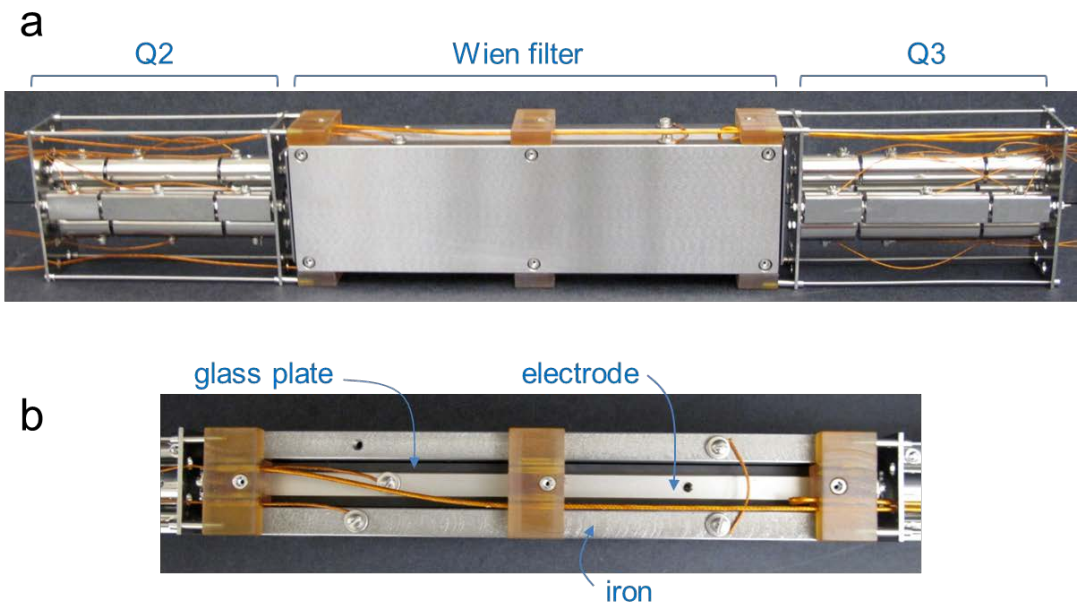

Figure 3.8 Photographs of the Wien filter assembly with quadrupoles Q2 and Q3 (a), and a top view of just Wien filter with electrical connections (b).

3.5 Performance of New Wien Filter

The major goal of this project was to design a new Wien filter that was simpler, easier to service, more reliable, and more versatile than the previous design. However, improving the mass resolution is much more difficult as we limited our project to the physical constraints of the old filter; we decided to not change the length of the filter (a) or the distance from the exit of the filter (L) to the separation aperture (D). Then, from Equation 3.15, the only variables left in our control are the magnitude of the electric and magnetic fields and the size of D. If we reduce the aperture size of D, we would also reduce the total ion current that reaches the interaction region. For the experiments in this thesis, reducing the ion current significantly would have made experiments much more difficult, so the aperture size was left at 2 mm. Therefore, only increasing the strength of the electric and magnetic fields is used to improve the resolving power

of the filter. In principle, one can increase the field strength of both the magnetic field and electric field to the limits of their corresponding power supplies. However, due to the thin 400 nm silicon coating on the glass plates in the Wien filter, we want to be careful to not draw excessive amount of current through the film which could damage its integrity. Therefore, we limit the electric field to less than 150 V, though we have tested the films under vacuum conditions up to 200 V for twenty four hours with no measurable loss in performance. Six months after the new Wien filter was installed, the resistance (measured externally) had increased in resistance from 3.8 MΩ to 5.5 MΩ. Though this is a moderate change in the resistance, the performance of the mass filter has not noticeably changed or degraded.

Figure 3.9 illustrates how increasing the electric field strength dramatically improves the resolving power of the Wien filter. In our instrument, we choose to fix the electric field strength and scan the electromagnet's voltage (and hence the magnetic field) to obtain a mass spectrum. The mass spectra shown in Figure 3.9 were taken after adding oxygen gas to the flowing afterglow and optimizing the ion optics for O^-. The electric field was set to a fixed value ranging from 18 V in (a) to 84 V in (c) while the magnetic field was scanned to allow different mass ions to pass undeflected through the filter. The mass resolution increases dramatically as the electric field is increased, and the three dominant ion peaks are cleanly resolved in panel (c) when the voltage difference on the electrodes was 84 V.

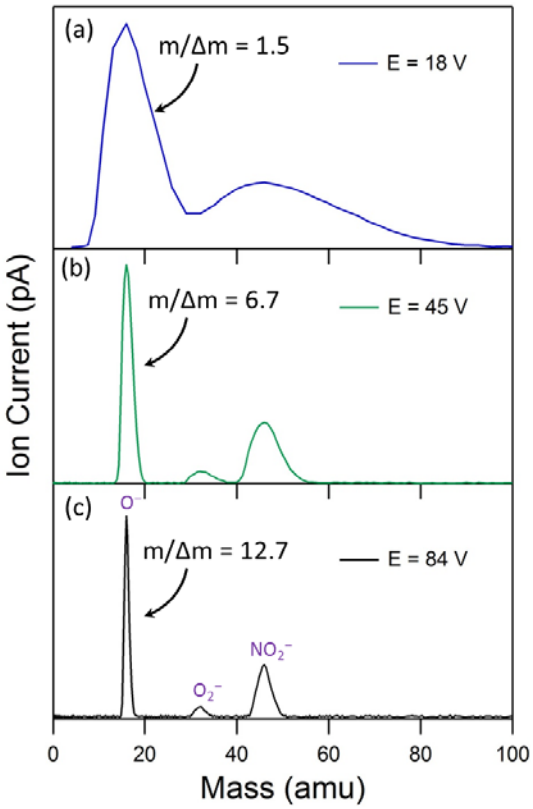

Figure 3.9 Mass spectra results using the new Wien filter with different strength magnetic and electric fields. The electric field was set to the specific value indicated in the inset of each panel and the electromagnets voltage was scanned to obtain the mass spectra. For the scans shown, oxygen was added to the flowing afterglow source and the ion optics were optimized to make O^-. The mass resolution dramatically increases as the electric field is increased from (a) – (c).

However, the real test of the Wien filter is separating ions created from reactions in our flow tube and being able to resolve the ionic products. Figure 3.10 is a typical mass spectrum of the products of the reaction of pyridine (C_5H_6N) with O^-. Under normal experimental conditions in which we make O^-, our ion source always produces O^-, O_2^- and NO_2^-, which we use to calibrate our mass spectra. The measured m/Δm for the O^- in this spectrum is 71, which nearly a factor of two greater than the previous Wien filter's best mass resolution.

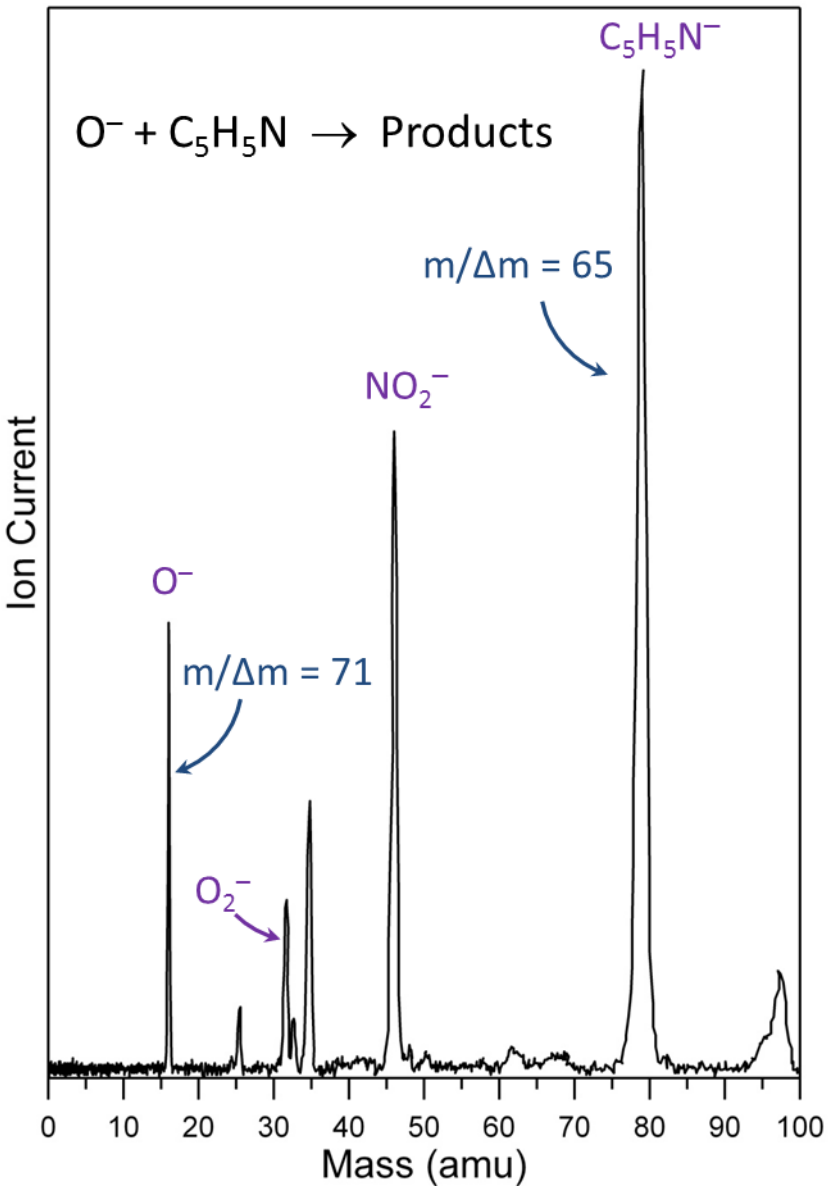

Figure 3.10 Typical mass spectrum of the products from the reaction of pyridine (C_5H_6N) with O^-. The O^- peak has a measured m/Δm = 71 and m/Δm = 65 for the $C_5H_5N^-$, which are both almost a factor of two greater than the best performance of the old Wien filter.

3.6 Conclusion

The new Wien filter is a vast improvement over the previous design and offers a reliable way to mass separate our ions. The mass resolution was dramatically improved while

maintaining the same high throughput of selected ions. The entire Wien filter assembly (including Q2 and Q3) is much easier to service with electrical connections are much less prone to shorting. However, one of the most important improvements with the new filter is the ability to measure the ion current on the two faceplates when troubleshooting poor ion beams. Before these faceplates were added, we were limited to measuring the ion current on three permanent measurement plates over the nearly ten feet which our ion beam travels. These two additional plates have greatly improved our ability to align our ion beam through the Wien filter and optimize the focusing and trajectory of the undeflected ion beam as it travels to the interaction region.

Lastly, we have found that the Wien filter's mass resolution changes dramatically with ion focusing and position. For a given electric and magnetic field setting, the mass resolution can change by 20–30% simply by adjusting the ion optics prior to the Wien filter. Therefore, when the best mass resolution is required, great care must be taken to optimize and maintain the ion beam position and spatial focusing during the course of an experiment.

3.7 References

1. Moore, J.H., C.C. Davis, and M.A. Coplan, *Building Scientific Apparatus*. Third ed 2003, Boulder: Westview Press. 654.
2. Johnson, M.A. and W.C. Lineberger, *Pulsed Methods for Cluster Ion Spectroscopy*, in *Techniques for the Study of Ion-Molecule Reactions*, J.M. Farrar and J. W. H. Saunders, Editors. 1988, Wiley: New York. p. 591-635.
3. Wahlin, L., *The Colutron, a zero deflection isotope separator.* Nuclear Instruments & Methods, 1964. **27**(1): p. 55-60.
4. Gunion, R.F., *Ultraviolet Photoelectron Spectroscopy of Molecular Anions*, in *Department of Chemistry*1995, Boulder: Boulder. p. 275.
5. Seliger, R.L., *E X B mass-separator design.* Journal of Applied Physics, 1972. **43**(5): p. 2352.
6. Jensen, K. and E. Veje, *Construction of a Wien filter heavy-ion accelerator.* Nuclear Instruments & Methods, 1974. **122**(3): p. 511-515.
7. Aberth, W., *High mass analysis capability of a Wien spectrometer.* International Journal of Mass Spectrometry and Ion Processes, 1986. **68**(1-2): p. 209-212.
8. Parker, N.W., *Wien Filter Design*, 1988, MicroBeam Inc.

4 Photoelectron Spectroscopy of Anilinide: $C_6H_5NH^-$

4.1 Introduction

Phenyl-substituted anions and radicals have been of considerable interest for the past thirty years. Aromatic amines are particularly important due to their presence in many biological molecules. Two of the simplest aromatic amines are anilinide ($C_6H_5NH^-$) and the related anilino radical (C_6H_5NH), which has had surprisingly sparse theoretical or experimental investigations. Bartmess used a pulsed ion cyclotron resonance spectrometer to record the first electron affinity determination of the anilino radical of 1.61(13) eV in 1979.[1] Five years later, Brauman refined this measurement to 1.704(30) eV using photodetachment threshold spectroscopy.[2] A time resolved resonance Raman study was performed just two years later to measure, for the first time, several vibrational frequencies of the anilino radical.[3] More recently, Ashfold and coworkers used photofragment translational spectroscopy to measure the N–H bond dissociation energy of aniline, BDE(N–H) = 90.44 kcal/mol^{-1}, forming the anilino radical as a product.

As mentioned in Chapter 1, the intensities of peaks in a photoelectron spectrum (or equivalently the intensities of transitions to the neutral vibrational levels) is governed by the Franck-Condon overlap between the ground vibrational wavefunction of the anion with the wavefunctions of the various vibrational levels of the neutral. If the geometries of the anion and neutral are similar, the best Franck-Condon overlap occurs between the ground vibrational wavefunction of the anion and the ground vibrational wavefunction of the neutral.

In this case, the most prominent peak in the photoelectron spectrum will correspond to the transition between the ground vibrational states of the anion and the neutral. This feature is designated as the origin, from which the adiabatic electron affinity can be readily determined. Furthermore, the width of the photoelectron spectral envelope is minimal in the case of a small geometry change; the Franck-Condon region of the spectrum is confined to an area near the potential minimum of the neutral molecule, where vibrational modes can be well-approximated as harmonic and uncoupled.[4]

Experimentally, there are no previously measured bond angles or lengths known for anilinide or the anilino radical. However, a recent theoretical report investigated the structure, electron affinity, and harmonic frequencies for series of substituted phenyl anions and radicals using a range of density functional methods.[5] This study found that both the ^{1}A' ground state of anilinide and ^{2}A" ground state of the anilno radical have C_s symmetry. More importantly, their results indicated that there was no significant differences in the geometry of the neutral after an electron had been removed from the anion. Therefore, we would expect that the photoelectron spectrum would have narrow vibrational envelope with a prominent origin peak.

In this chapter, we present the first photoelectron spectrum of anilinide and report the most accurate electron affinity for the anilino radical to date. The measured spectrum is surprisingly simple for a molecule containing 13 atoms, with a clear origin peak and only one dominant vibrational progression. Anilinide represents a model system where small geometry changes between the anion and the neutral result in a simple photoelectron spectra that are straightforward to understand and analyze. Furthermore, the anilino radical is also isoelectronic benzyl ($C_6H_5CH_2$) and phenoxyl (C_6H_5O) radicals, which have been previously studied with photoelectron spectroscopy.[6] The three photoelectron spectra have almost identical vibrational

structure but very different electron affinities. We compare the series of phenyl-substituted anions and radicals to understand how the different substituent on the benzene ring affects the structure and thermochemistry of three related molecules.

4.2 Experimental Method

Anilinide ($C_6H_5NH^-$) is generated using the flowing afterglow ion source described in Chapter 2. Methane is added downstream of O^- where H-atom abstraction from methane forms hydroxide (HO^-), which is thermalized and subsequently reacts with aniline: ≥98.5%, Sigma-Aldrich) to generate anilinide anions via proton abstraction. Spectra was recorded with both ions at room temperature (~ 300 K) and cooled with a liquid nitrogen (~ 200 K). The mass resolution of the new Wien velocity filter for these experiments was $m/\Delta m$ ~ 60. Typical anilinide ion beam currents were ~ 100 pA. The ~1 W output from a single-mode continuous-wave argon ion laser operating at 364 nm (3.40814 eV) is built up to approximately 100 W of circulating power using a high Q resonant cavity in the interaction region. The energy resolution of the hemispherical analyzer is approximately 11 meV under the experimental conditions used here.

Electronic structure calculations were performed with the Gaussian 03 software package.[7] Geometry optimization and frequency calculations were carried out using density functional theory (DFT) method with Becke's hybrid three-parameter functional[8] and the correlation functional of Lee et al.[9] (B3LYP) and with an augmented correlation-consistent polarized double-zeta basis set (aug-cc-pVDZ).[10, 11] The geometry of both the anilinide anion and anilino radical where constrained to C_s symmetry. No scaling factor is applied to the calculated vibrational frequencies.

The Franck-Condon profiles of the photoelectron spectra are simulated using the PESCAL program.[12] The simulations employ the calculated theoretical geometries, normal

mode vectors, and vibrational frequencies of the anion and neutral states. The Franck-Condon factors are computed in the harmonic oscillator approximation including Duschinsky rotation using the Sharp-Rosenstock-Chen method.[13] The individual vibronic peak contours are simulated by a Gaussian function with a FWHM of 11 meV, consistent with instrumental resolution.

4.3 Results and Discussion

The photoelectron spectrum of anilinide, shown in Figure 4.1a, consists of a very simple and regular vibrational progression. The most prominent peak in the spectrum, peak B in Figure 4.1a, is the origin corresponds to an electron affinity (EA) of 1.607(4) eV. The positions and assignments of all the peaks in the anilinide spectrum are given in Table 4.1. There is a very regular peak spacing of approximately 525 cm^{-1} between peaks B–F, which appear to arise from a single vibrational progression. All calculated vibrational modes, along with a qualitative description of the atomic motion and available experimental measurements, are listed in Table 4.2. The measured frequency of the vibrational progression agrees well with the calculated frequency of the ν_{22} mode of the anilino radical: 531 cm^{-1}. Based on the excellent agreement between the simulated spectrum in Figure 1b with the experimental data, peaks B–F are predominately due to the 22_0^n transition. It is a little surprising that there is only one dominant active vibrational mode as the anilino radical has 33 vibrational modes, of which 23 are totally symmetric A' modes. However, as will be shown below, the photoelectron spectrum of related substituted phenyl anions have very similar simple vibrational progressions dominated by only one or two vibrational modes.

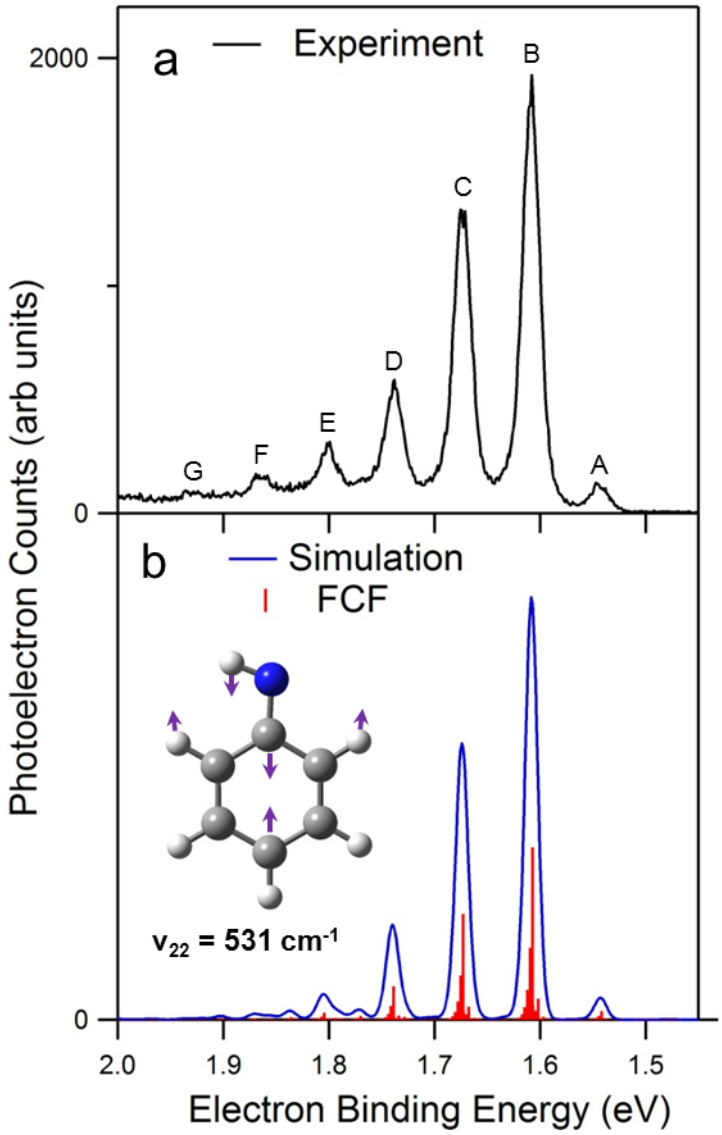

Figure 4.1 Magic-angle negative ion photoelectron spectrum of anilinide. (a) 364-nm experimental spectrum with ions at ~ 300 K. (b) Simulated photoelectron spectrum at 300 K (blue line) with red sticks corresponding to the Franck-Condon factors (FCF) for the vibronic transitions from the ground states of the anilinide anion to the anilino radical. Inset in (b) illustrates the calculated atomic displacements of the vibrational mode in the anilino radical which dominates the vibrational progression observed in the photoelectron spectrum.

Table 4.1 Peak positions and assignments for the photoelectron spectrum of anilinide anion.

Peak[a]	Frequency[b]	Assignment[c]
A	-517(10)	22_1^0
B	0	0_0^0
C	524(10)	22_0^1
D	1048(10)	22_0^2
E	1551(10)	22_0^3
F	2054(15)	22_0^4
G	2559(20)	

[a] Peak labels used in Figure 1

[b] Relative to the origin peak, B

[c] The ν_{22} mode involves symmetric ring deformation

Table 4.2 Calculated and experimental vibrational frequencies of anilinide anion ($\tilde{X}\ ^1$A') and the anilino radical ($\tilde{X}\ ^2$A")

Mode		Description	Calculations[a] (cm^{-1})		Experiment[d] (cm^{-1})	
			Anion	Neutral	Anion	Neutral
A′	ν_1	N-H str	3392	3418		
	ν_2	C-H sym str	3165	3206		
	ν_3	C-H str	3149	3199		
	ν_4	C-H str	3122	3186		
	ν_5	C-H str	3106	3179		
	ν_6	C-H str	3097	3169		
	ν_7	C-C sym str	1618	1587		
	ν_8	C-C str	1538	1565		1560[b]
	ν_9	C-C str + C-N wag	1479	1478		1505[b]
	ν_{10}	C-C str + C-N str	1501	1460		1452[b]
	ν_{11}	C-C str + N-H wag	1358	1360		
	ν_{12}	C-H sym wag	1328	1340		
	ν_{13}	C-N str + C-C str	1369	1313		1324[b]
	ν_{14}	C-H wag + C-C str	1167	1175		
	ν_{15}	C-H wag + N-H wag	1135	1162		
	ν_{16}	C-H wag + N-H wag	1168	1161		
	ν_{17}	C-H wag + C-C str	1058	1084		
	ν_{18}	Ring breathing	1019	1025		
	ν_{19}	Ring deformation	968	978		~980[a]
	ν_{20}	Ring breathing	816	828		817[b]
	ν_{21}	Ring deformation	619	614		
	ν_{22}	Ring deformation	527	531		**524(10)**[c] 533[b]
	ν_{23}	C-C-N bend	416	417		
A″	ν_{24}	C-H wag	942	1000		1003[b]
	ν_{25}	C-H wag	933	982		
	ν_{26}	C-H wag	706	917		
	ν_{27}	C-H wag	794	826		
	ν_{28}	C-H wag + ring torsion	822	785		
	ν_{29}	C-H wag + N-H wag	663	690		
	ν_{30}	C-H wag	670	672		
	ν_{31}	Ring flap	493	489		
	ν_{32}	Ring torsion	430	390		
	ν_{33}	o-o-p–Ring deformation	179	199		

[a] Reference [14]

[b] Reference [3]

[c] This work

[d] Tripathi measured band at 1167 cm^{-1}, which could be assigned to three different calculated modes involving C–H bending motion (1161, 1162, and 1175 cm^{-1}), and is left unassigned

Table 4.3 summarizes the calculated optimized geometry and associated geometry change between the anilinide anion and the anilino radical following the photodetachment of an electron. There is very modest but localized geometry change of the ∠C3–C4–C5 and ∠C6–C1–C2 bond angles, which correlate with the atomic displacements in the ν_{22} vibrational mode of the anilino radical and illustrated in the inset of Figure 4.1b. If the negative charge in the anion was localized on the nitrogen atom, one would expect the ∠C1–N–H bond angle to change substantially. Our calculations indicate that there is only a modest 1° change in this bond angle when an electron is removed from the anion. Other studies have suggested that the negative charge is indeed delocalized over the phenyl π-system.[15] This conclusion agrees with our experimental results, including the photoelectron angular distribution measurements, and indicate negligible activity in vibrational modes involving the N – H bond or ∠C1–N–H bond angle.

Table 4.3 Optimized Geometry of anilinide anion ($\tilde{X}\ ^1$A') and the anilino radical ($\tilde{X}\ ^2$A") and the calculated net geometry change after removing an electron from the anion to form the radical (B3LYP/aug-cc-pvdz). Bond lengths are in units of angstroms (Å) and bond angles are in units of degree (◦). The geometry change is defined as the difference between the values of the internal coordinates from the anion to the radical.

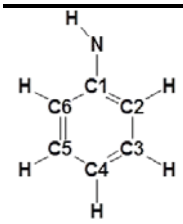	Anilinide Anion	Anilino Radical	Geometry Change
Internal Coordinate	$\tilde{X}\ ^1$A'	$\tilde{X}\ ^2$A"	$\tilde{X}\ ^2$A" ← $\tilde{X}\ ^1$A'
C1–C2	1.449	1.436	–0.013
C2–C3	1.388	1.385	–0.003
C3–C4	1.412	1.408	–0.004
C4–C5	1.408	1.408	0
C5–C6	1.391	1.386	–0.005
C6–C1	1.451	1.438	–0.013
C2–H	1.093	1.089	–0.004
C3–H	1.095	1.091	–0.004
C4–H	1.091	1.090	–0.001
C5–H	1.096	1.091	–0.005
C6–H	1.095	1.092	–0.003
C1–N	1.337	1.341	+0.004
N–H	1.025	1.027	+0.002
∠C1–C2–C3	122.7	120.9	–1.8
∠C2–C3–C4	122.0	120.4	–1.6
∠C3–C4–C5	117.1	120.1	+3
∠C4–C5–C6	121.9	120.3	–1.6
∠C5–C6–C1	122.7	120.9	–1.8
∠C6–C1–C2	113.7	117.5	+3.8
∠C6–C1–N	126.1	124.5	–1.6
∠C1–N–H	108.5	109.5	+1
∠C1–C6–H	117.9	118.6	+0.7
∠C1–C2–H	117.0	117.4	+0.4

The simulated anilinide spectrum also indicates there are several other minor transitions that contribute to peaks B–D that are spaced by 20 cm^{-1}. These transitions are due to sequence bands from the low–frequency out-of-plane ν_{33} vibrational mode (33_n^n). Due to the low frequency of this mode, these sequence bands will still have some intensity even when the ions are cooled to ~ 200 K; for this reason, we do not measure appreciable peak narrowing in our cold spectrum (shown in Figure 4.2). Peak A, to the lower binding energy of the origin, is a hot band assigned to the 22_1^0 transition from vibrationally excited anions. When the ions were cooled to ~ 200 K, the intensity of this peak is reduced significantly, confirming its assignment as a hot band.

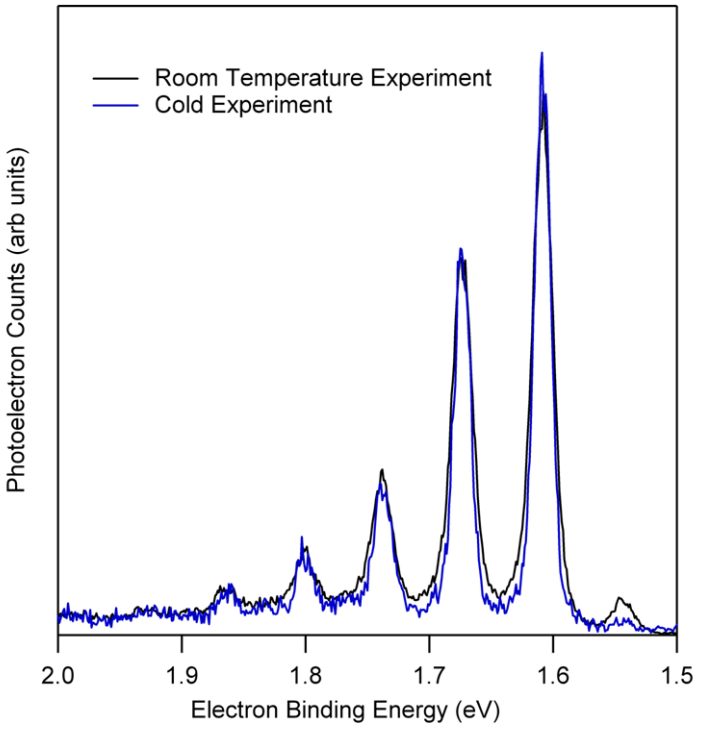

Figure 4.2 The 364 nm magic angle photoelectron spectrum of anilinide at ~ 300 K (black line) and ~ 200 K (blue line). The spectrum measured with cold ions has lower counts and was normalized to the room temperature spectrum. Both spectra look very similar except for the intensity of the hot band peak at approximately 1.55 eV, which is reduced in when the ions are cooled.

Since the photoelectron spectra of two other phenyl-substituted anions have been previously recorded in this lab[6], it is informative to compare them with the results of anilinide. Benzyl anion ($C_6H_5CH_2^-$) and phenoxide ($C_6H_5O^-$) are isoelectronic with anilinide and share many similarities. All three anionic substituents (NH^-, CH_2^-, and O^-) are powerful π-electron-donor substituents[16] whose π-donating ability increase in the order of $O^- \sim NH^- < CH_2^-$. Additionally, based on the results for anilinide in this work, we would expect only modest geometry changes when an electron is detached from benzyl and phenoxide anions.

Figure 4.3 compares the three photoelectron spectra, which were all recorded using similar experimental conditions; 364 nm spectra recorded at magic angle using room temperature ions. The three spectra look remarkably similar, in that there is a single vibrational progression with ~ 515 cm^{-1} peak spacing. This isn't too surprising since all three anions and corresponding radical geometries have many similarities, as we anticipated.[15, 17] Only small difference are calculated in the C_1–C_2 and the C_3–C_4 bonds in the radicals, whose lengths decrease in going from phenoxyl to benzyl radical. This variance in bond lengths has been attributed to the differences in the electronegativity of the substituents.[17] In a computational study on these three radicals, Adamo and coworkers found that there was no significant mixing in the vibrational modes characteristic of the six-membered ring and those representative of the substituents.[17] Therefore, the vibrational normal modes in the anilino radical have analogous modes in the benzyl and phenoxyl radicals. The 515 cm^{-1} mode in both benzyl and phenoxyl radicals was assigned to a vibrational mode that involves the same atomic displacements seen in the ν_{22} vibrational mode of the anilino radical.

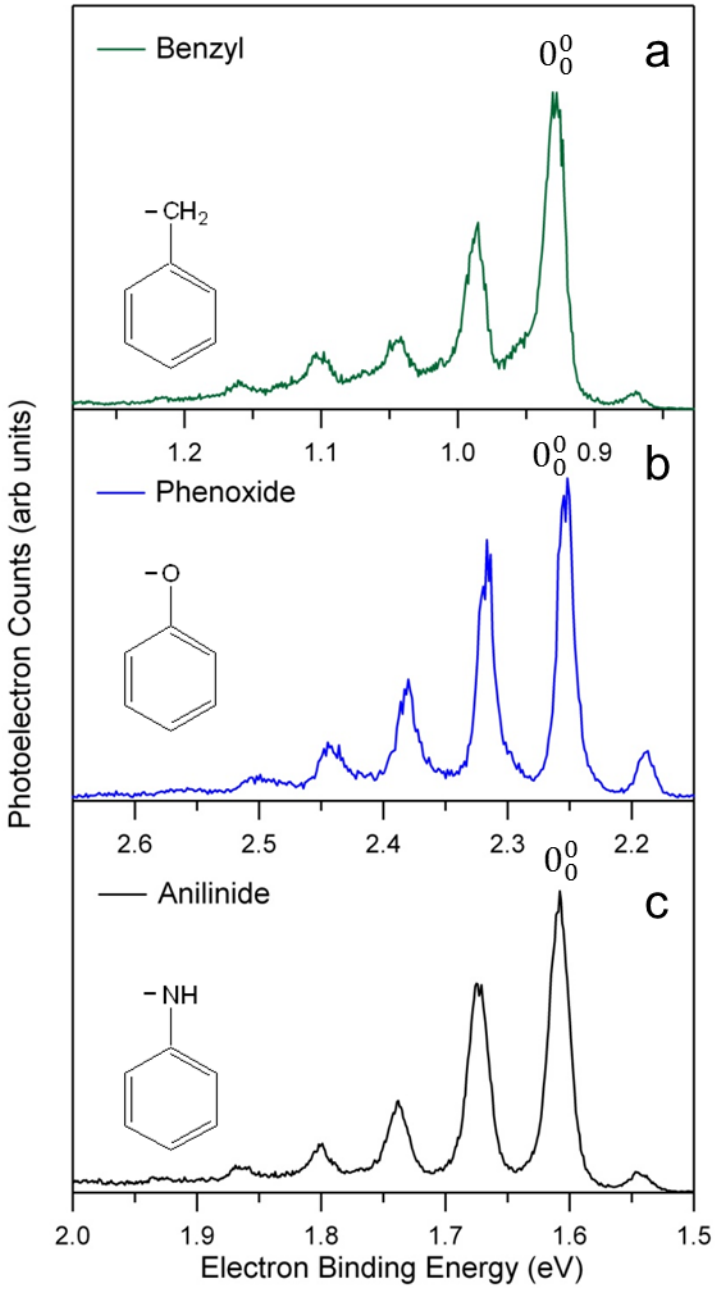

Figure 4.3 The 364 nm magic angle photoelectron spectra of three phenyl-substituted anions. The spectra of benzyl anion ($C_6H_5CH_2^-$) and phenoxide ($C_6H_5O^-$) were previously recorded in our lab and shown in (a) and (b) respectively.[6] The aniline spectrum with room temperature ions is shown in (c). The three spectra are plotted on independent energy scales with the origin peaks (0_0^0) aligned to highlight the similar vibrational progressions.

However, the EA's of the three radicals are drastically different, spanning a range of almost 1.5 eV. The trend in the EA is found to increase in magnitude with the electronegativity of the substituent on the benzene ring: $O^- > NH^- > CH_2^-$. Phenoxyl has the largest EA value at 2.253(6) eV, followed by anilino at 1.607(4) eV, with Benzyl having the lowest EA at 0.912(6) eV.

4.4 Conclusion

The photoelectron spectrum of anilinide is measured for the first time and which allows for the most accurate EA determination of the anilino radical of 1.607(4) eV. The measured spectrum contains only one dominant vibrational progression corresponding to a ring-distortion vibrational mode. This molecule is a model system for when there is a small geometry change between an anion and the corresponding neutral, resulting in a very simple photoelectron spectrum that is straight forward to analyze. We also compared our results with two other previously studied phenyl-substituted anions to determine the effects of changing the substituent on a benzene ring. The photoelectron spectra are nearly identical since the changes in geometry are nearly the same for all three species. The EAs, however, are significantly different due to the different electronegativities of the substituents.

4.5 References

1. Bartmess, J.E., J.A. Scott, and R.T. McIver, *Scale of acidities in the gas phase from methanol to phenol.* Journal of the American Chemical Society, 1979. **101**(20): p. 6046-6056.
2. Drzaic, P.S. and J.I. Brauman, *Electron photodetachment from phenylnitrene, anilide, and benzyl anions - Electron affinities of the anilino and benzyl radicals and phenylnitrene.* Journal of Physical Chemistry, 1984. **88**(22): p. 5285-5290.
3. Tripathi, G.N.R. and R.H. Schuler, *Time resolved resonance raman Spectra of anilino radical and aniline radical cation.* Journal of Chemical Physics, 1987. **86**(7): p. 3795-3800.
4. Vogelhuber, K.M., et al., *Photoelectron spectra of dihalomethyl anions: Testing the limits of normal mode analysis.* The Journal of Chemical Physics, 2011. **134**(18): p. 184306-13.
5. Xu, W. and A. Gao, *Structures, Electron Affinities, and Harmonic Vibrational Frequencies of C_6H_5X/C_6H_5X- (X = N, S, NH, PH, CH_2, and SiH_2).* The Journal of Physical Chemistry A, 2005. **110**(3): p. 997-1004.
6. Gunion, R.F., et al., *Ultraviolet photoelectron-spectroscopy of the phenide, benzyl and phenoxide anions, with ab initio calculations.* International Journal of Mass Spectrometry and Ion Processes, 1992. **117**(1-3): p. 601-620.
7. Frisch, M.J., et al., *Gaussian 03, Revision B.01*2004, Wallingford, CT: Gaussian, Inc.
8. Becke, A.D., *Density-functional thermochemistry. III. The role of exact exchange.* Journal of Chemical Physics, 1993. **98**(7): p. 5648-5652.
9. Lee, C.T., W.T. Yang, and R.G. Parr, *Development of the colle-salvetti correlation-energy formula into a functional of the electron-density.* Physical Review B, 1988. **37**(2): p. 785-789.
10. Woon, D.E. and T.H. Dunning, *Gaussian-Basis Sets for Use in Correlated Molecular Calculations .3. the Atoms Aluminum through Argon.* Journal of Chemical Physics, 1993. **98**(2): p. 1358-1371.
11. Dunning, T.H., *Gaussian-basis sets for use in correlated molecular calculations. 1. The atoms boron through neon and hydrogen.* Journal of Chemical Physics, 1989. **90**(2): p. 1007-1023.
12. Ervin, K.M., *PESCAL, Fortran program.* PESCAL, Fortran program, 2010.
13. Ervin, K.M., et al., *Naphthyl radical: Negative ion photoelectron spectroscopy, Franck-Condon simulation, and thermochemistry.* J. Phys. Chem. A, 2001. **105**(48): p. 10822.
14. King, G.A., T.A.A. Oliver, and M.N.R. Ashfold, *Dynamical insights into (1)pi sigma* state mediated photodissociation of aniline.* Journal of Chemical Physics, 2010. **132**(21).
15. Rappoport, Z.Z., ed. *The Chemistry of Anilines, Part 1*. 2007.

16. Kemister, G., et al., *A theoretical approach to substituent effects. Examination of phenoxides and anilides as models for benzyl anions.* The Journal of Organic Chemistry, 1980. **45**(6): p. 1056-1060.

17. Adamo, C., et al., *Structure and magnetic properties of benzyl, anilino, and phenoxyl radicals by density functional computations.* Journal of Chemical Physics, 1998. **109**(23): p. 10244-10254.

5 Photoelectron Spectroscopy of Azinides: Pyridinide, 1,2-diazinide, 1,3-diazinide, 1,4-diazinide, 1,3,5-triazinide

5.1 Introduction

There is considerable interest in understanding the pyrolysis of nitrogen-containing heterocycles, especially five-membered (azole) and six-membered (azine) compounds.[1-3] These nitrogen-rich compounds are abundant in coal,[4, 5] and represent the fundamental unit of many high-energy density materials.[6, 7] Combustion of these compounds leads to the production of nitrogen oxide (NO_x) species, which play an important role in the formation and degradation of tropospheric ozone.[8] A number of recent studies have focused on the pyrolysis of azine molecules containing one, two, and three nitrogen atoms (referred to as pyridine, diazines, and triazines, respectively).[9-14] One of the main goals of these studies was to determine the strength and reactivity of specific C–H bonds that were shown to be critical in the decomposition process. For example, the generally accepted mechanism for decomposition of pyridine is initiated by the cleavage of the weakest C–H bond – the bond adjacent to the nitrogen atom.[3] Clearly, knowledge of the bond dissociation energy (BDE) of various C–H bonds in azine molecules is needed to understand which decomposition pathways are most important.

Azines provide model systems to investigate how replacement of a C–H group with a nitrogen atom affects the thermochemical properties of six-membered aromatic rings. Only a limited number of experimental studies of gaseous azines exist, and those have been largely limited to shock tube experiments.[9, 11, 12, 14-16] One of the most important shock tube results was the bond strengths for pyridine, 1,3-diazine, and 1,4-diazine. However, the shock tube

measurements rely heavily on modeling and fits to data, which in turn lead to fairly large error bars for the dissociation energy. There appear to be no experimental determinations of the BDE of 1,2-diazine or any triazines. These shock tube results were later complemented by a comprehensive theoretical investigation by Barckholtz et al., focused on computing the C–H and N–H BDEs of aromatic hydrocarbons.[17] Both shock tube and theoretical studies concluded that when there was more than one possible C–H bond fission site, the most stable radical site was always adjacent to a nitrogen atom. Furthermore, both found that the strengths of all C–H bonds in pyridine and the diazines were less than the C–H bond strength in benzene (112.9(5) kcal mol^{-1}), the prototypical six-membered ring aromatic molecule.[18]

The bond strength of benzene was determined[19] using a combination of gas-phase ion chemistry and negative ion photoelectron spectroscopy[20] utilizing the negative ion thermochemical cycle given by Equation 5.1 and depicted in Figure 5.1,

Equation 5.1

$$\mathrm{D(R-H)} = \Delta_{\mathrm{acid}}H(\mathrm{RH}) + \mathrm{EA(R)} - \mathrm{IE(H)}$$

where D(R–H) is the BDE, $\Delta_{\mathrm{acid}}H$(RH) is the gas-phase enthalpy of deprotonation, EA(R) is the electron affinity and IE(H) is the ionization energy of a hydrogen atom. In this chapter, we apply this well-established methodology to obtain the C–H bond strengths of the most acidic sites of several azines. To date, the EAs of any azinyl radical have not been measured. The gas phase acidities of pyridine and the diazines have been reported,[21] but these measurements were made at elevated temperatures (450 – 650 K) with relatively large error bars (±2.4 kcal mol^{-1}). The identity of the deprotonation site was also not verified, but only surmised based on chemical intuition and the primitive theoretical calculations available twenty years ago. The gas phase acidity of 1,3,5-triazine has never been measured, though a recent study of its reactivity was

recently reported.[16] Schafman and Wenthold[15] investigated the site-specific deprotonation of pyridine and determined the gas phase acidities of each of the three pyridinide isomers. In contrast to the findings for pyridinyl radical in the shock tube studies, the position of the most stable anion arises from deprotonation of the carbon in the 4-position, farthest from the nitrogen atom.

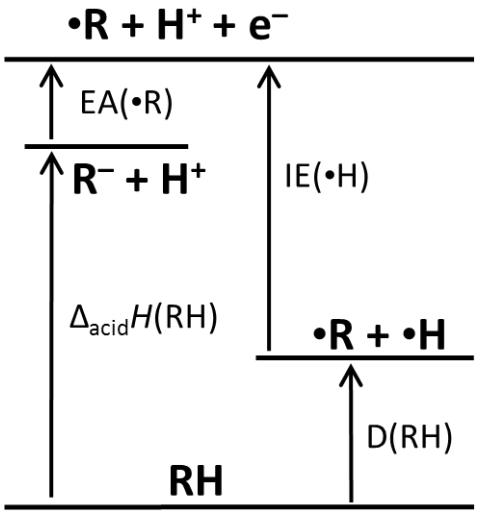

Figure 5.1 Schematic of the Negative Ion Thermochemistry Cycle used to relate the experimentally determined EA and $\Delta_{acid}H_{298}$ with the known ionization energy (IE) of hydrogen to obtain the C–H BDEs (D(RH)) in this work.

A brief review of earlier work from this laboratory on the photoelectron spectroscopy of phenide ($C_6H_5^-$, resultant anion after removing a proton from benzene) provides a framework for understanding the experimental results for the azinide anions, which are isoelectronic with phenide and have many similar properties. The photoelectron spectrum of phenide was, at the time of publication, unusually complex but was composed of extensive, resolved vibrational structure.[20] The phenide spectrum, reproduced in Figure 5.2a, is dominated by two ring-

distortion vibrational progressions with frequencies of 600(10) cm^{-1} and 968(15) cm^{-1}. The presence of only two dominant active vibrational modes is remarkable, given that there are ten allowed A_1 symmetry modes in the phenyl radical. The normal modes responsible for the vibrational progression are in-plane ring distortions principally involving the carbon atom where the ejected electron was localized. The reported EA was 1.096(6) eV, much higher than for other alkyl radicals that do not have a conjugated π electronic system.[22] This finding shows that the ring system contributes significantly to the stabilization of the electron pair on the carbon atom, from which a proton was removed.

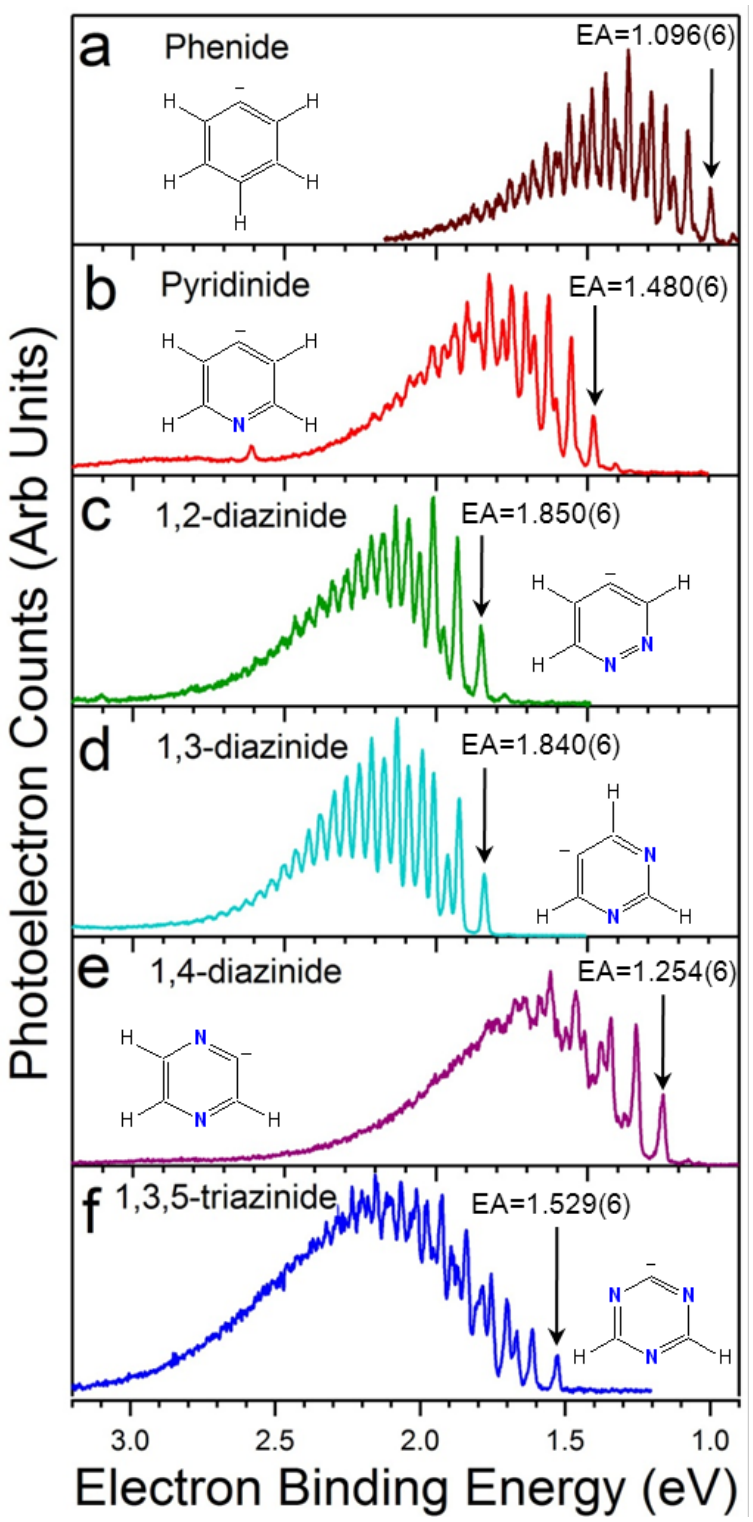

Figure 5.2 Magic-angle negative ion photoelectron spectra of phenide (a), pyridinide (b), 1,2-diazinide (c), 1,3-diazinide (d), 1,4-diazinide (e), 1,3,5-triazinide (f).

The deprotonation enthalpy of benzene was determined to be $\Delta_{acid}H_{300}(C_6H_6)$ = 401.7(5) kcal mol^{-1} in a detailed study by Davico et al.[19] This study measured the rate constants for proton transfer between amide ion and benzene, and between phenide ion and ammonia, obtaining the equilibrium constant between the forward and reverse proton transfer reactions.[19] Recent work has refined the acidity of ammonia – the reference acid in the Davico work – and the acidity of benzene was slightly reduced,[18] by 0.5 kcal mol^{-1}, to 401.2(5) kcal mol^{-1}. Using this $\Delta_{acid}H$ for benzene, and the EA of phenyl radical (0 K), the BDE of benzene was determined using Equation 5.1 to be $D_{300}(C_6H_6)$ = 112.9(5) kcal mol^{-1}. This benzene C–H bond strength provides the basic reference point for evaluating the C–H bond strengths of azines upon systematic addition of nitrogen atom(s).

In this Chapter we employ a combination of gas-phase ion chemistry, anion photoelectron spectroscopy, and *ab initio* calculations to investigate the gas phase acidities, radical EAs, and C–H bond strengths of five azine molecules: pyridine, 1,2-diazine (pyridazine), 1,3-diazine (pyrimidine), 1,4-diazine (pyrazine), and 1,3,5-triazine (s-triazine). We measure the EA of the azinyl radicals and gas phase acidity for each azine (with the exception of pyridine[23]), which allows determination of the C–H BDE for the most acidic proton site in each azine molecule.

Due to the large number of molecules studied, the result section is divided into six sections. First, we present an overview of our experimental findings, followed by a detailed analysis of 1,3-diazine, which typifies the other four azines studied. Following the experimental results, we discuss the general trends in C-H bond strengths observed in the context of adding nitrogen atoms to azines.

5.2 Experimental Method

Negative Ion Photoelectron Measurements

The negative ion photoelectron spectrometer used in this experiment has been described in detail in Chapter 2. Negative ions are formed in a flowing afterglow ion source. A microwave discharge containing trace amounts of O_2 in He buffer gas (~0.4 Torr) generates atomic oxygen radical anion, O^-. Methane is added downstream of O^- where H-atom abstraction from methane forms hydroxide (HO^-), which is thermalized and subsequently reacts with an appropriate azine precursor (pyridine, 1,2-diazine, 1,3-diazine, 1,4-diazine, 1,3,5-triazine: ≥97%, Sigma-Aldrich) to generate azinide anions. Since many of the azine molecules have low vapor pressures, high-purity helium (General Air, 99.99999%) was bubbled through the sample which significantly increased the azinide ion signal. Spectra was recorded both with ions at room temperature (~ 300 K) and cooled with a liquid nitrogen (~ 150 K). The mass resolution of the new Wien velocity filter for these experiments was $m/\Delta m$ ~ 60. Typical mass-selected ion beam currents were ~ 50 –120 pA. The ~1 W output from a single-mode continuous-wave argon ion laser operating at 364 nm (3.40814 eV) is built up to approximately 100 W of circulating power in the interaction region. The energy resolution of the hemispherical analyzer is approximately 11 meV under the experimental conditions used here.

Flowing Afterglow-Selected Ion Flow Tube (FA-SIFT) Measurements

The gas phase acidities of the azines were determined via proton transfer reaction kinetic measurements using a variety of anions in a tandem FA-SIFT instrument that has been described previously.[24, 25] The experimental details for the acidity measurements have been reported in detail in previous publications[16, 26] and will not be repeated here. However, a brief summary of

the method used to extract the gas phase acidities and related deprotonation enthalpies is provided below.

The gas-phase acidity measurements for the most acidic proton of the azines (AH) are made relative to a reference acid (RH) by measuring the forward (k_f) and reverse (k_r) proton-transfer reaction rate constants at 298 K, shown below in Equation 5.2.

Equation 5.2

$$RH + A^- \underset{k_r}{\overset{k_f}{\rightleftarrows}} R^- + AH$$

The ratio of the rate constants gives the proton-transfer equilibrium constant ($K_{equil} \equiv k_f / k_r$), which can be used together with the known $\Delta_{acid}G_{298}(RH)$ to determine $\Delta_{acid}G_{298}(AH)$ using Equation 5.3.

Equation 5.3

$$\Delta_{acid}G_{298}(AH) = \Delta_{acid}G_{298}(RH) + RT \ln K_{equil}$$

A small calculated entropy correction ($T\Delta_{acid}S_{298}$) is added to the measured $\Delta_{acid}G_{298}(AH)$ value to obtain $\Delta_{acid}H_{298}$ using Equation 5.4.

Equation 5.4

$$\Delta_{acid}H_{298}(AH) = \Delta_{acid}G_{298}(AH) + T\Delta_{acid}S_{298}(AH)$$

Theoretical methods

Electronic structure calculations were performed with the Gaussian 03 software package.[27] Geometry optimization and frequency calculations were carried out using density functional theory (DFT) method with Becke's hybrid three-parameter functional[28] and the

correlation functional of Lee et al.[29] (B3LYP) and with an augmented correlation-consistent polarized double-zeta basis set (aug-cc-pVDZ).[30, 31] No scaling factor is applied to the calculated vibrational frequencies.

The Franck-Condon profiles of the photoelectron spectra are simulated using the PESCAL program.[32] The simulations employ the calculated theoretical geometries, normal mode vectors, and vibrational frequencies of the anion and neutral states. The Franck-Condon factors are computed in the harmonic oscillator approximation including Duschinsky rotation using the Sharp-Rosenstock-Chen method.[33] The individual vibronic peak contours are simulated by a Gaussian function with a FWHM of 11 meV, consistent with instrumental resolution.

5.3 Results

Figure 5.2 shows the negative ion photoelectron spectra of the five azinide anions studied, as well as the previously published spectrum of phenide for comparison.[34] One of the most striking features of the azinide spectra is the similarity of the vibrational progressions. The structure in the spectra is largely dominated by two vibrational modes with frequencies of approximately 700 and 1000 cm^{-1}, analogous to those observed in the phenide spectrum. Each spectrum has a clear origin peak that is marked with an arrow indicating the measured EA, reported in Table 5.1. The photoelectron spectra of 1,3-diazinide and 1,3,5-triazinide, shown in Figure 5.2d and Figure 5.2f respectively, were recorded at ~ 150 K; the remaining spectra were collected at 300 K. All 300 K spectra exhibit a singular hot band peak to the lower-eBE side of the origin peak. From these hot bands, we extract a frequency corresponding to a transition originating from a ring-distortion mode in the anion. Measured vibrational frequencies are

summarized in Table 5.2. With a photon energy of ~ 3.4 eV, we did not observe clear spectroscopic signatures of excited states of the neutral radicals. There are weak features that appear at higher binding energy in the spectra of pyridinide and 1,2-diazinide, but the signal level was insufficient for a conclusive assignment.

Table 5.1 Summary of Experimental Thermochemical Properties of Azine Systems: C-H Bond Dissociation Energies, Electron Affinities, and Deprotonation Enthalpies

	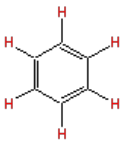 Benzene	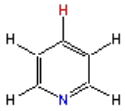 Pyridine	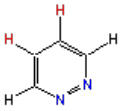 1,2-diazine	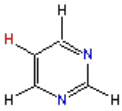 1,3-diazine	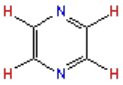 1,4-diazine	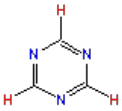 1,3,5-triazine
D_{298}(C-**H**) (kcal mol^{-1})	112.9(5)[a]	110.4(2.0)	111.3(7)	113.4(7)	107.5(4)	107.8(7)
EA (eV)	1.096(6)[b]	1.480(6)	1.850(6)	1.840(6)	1.254(6)	1.529(6)
$\Delta_{acid}H_{298}$(C-**H**) (kcal mol^{-1})	401.2(5)[a]	389.9(2.0)[c]	382.2(7)	384.6(7)	392.2(4)	386.1(7)

[a] Reference [18]
[b] Reference [34]
[c] Rererence [15]

Table 5.3 summarizes the results of the gas-phase acidity measurements from the FA-SIFT experiments. Our experimental acidities are from the most acidic sites in the azines, all which reside within an 8 kcal mol^{-1} range and have error bars of less than 1 kcal mol^{-1}. The gas-phase acidity of pyridine, which was previously measured by Schafman and coworkers, was not repeated in this study but is described in the results section below.[15]

Table 5.2 Experimental Vibrational Frequencies of Azine Radicals and Anions[a]

	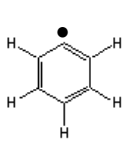 Phenyl	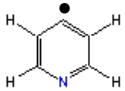 Pyridinyl	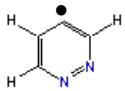 1,2-diazinyl	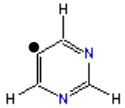 1,3-diazinyl	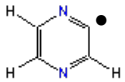 1,4-diazinyl	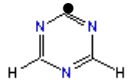 1,3,5-triazinyl
Neutral *Anion*	ν_4=600(10)	ν_9=600(20) *ν_9=580(50)*	ν_{14}=640(20) *ν_{15}=620(50)*	ν_8=680(20) *ν_8=660(40)*	ν_{14}=700(20) *ν_{14}=670(50)*	ν_7=680(20) *ν_7=670(40)*
Neutral	$\nu_{9/10}$=968(15)	ν_7=1010(50)	$\nu_{12/13}$=1000(80)	ν_7=980(20)	NA	$\nu_{4/5}$=1110(70)

[a] Neutral frequencies are grouped in rows by type of vibration; frequencies are labeled based on mode ordering for a particular azine.

Table 5.3 Summary of FA-SIFT Results

Azine	$\Delta_{acid}G_{298}$[a]	$\Delta_{acid}S_{298}$[b]	$\Delta_{acid}H_{298}$
Pyridine	382.1(2.0)	7.9	389.9(2.0)[c]
1,2-diazine	374.0(7)	8.2	382.2(7)
1,3-diazine	376.8(7)	7.8	384.6(7)
1,4-diazine	383.5(4)	8.7	392.2(4)
1,3,5-triazine	377.3(7)	8.8	386.1(7)

[a] Units of kcal mol^{-1}
[b] Calculated at the B3LYP/6-311++G(d,p) level of theory
[c] Reference [15]

Using the measured EA and $\Delta_{acid}H$ values, we directly determine the BDE for all five azines via Equation 5.1, which are reported in Table 5.1. Due to the precision in the EA and gas-phase acidity measurements, the site-specific reported C–H BDEs have much smaller error bars than previously reported bond strengths for pyridine, 1,3- and 1,4-diazine. The BDEs of 1,2-diazine at the 4 position and 1,3,5-triazine are experimentally determined for the first time.

As discussed in the experimental methods section, the azinide anions are synthesized in both experiments by deprotonation of the parent azine using HO^- as the initial base. In the case of 1,4-diazine and 1,3,5-triazine, all the hydrogen atoms are equivalent and there is only one anion isomer possible. However, for pyridine, 1,2- and 1,3-diazine, there are several unique hydrogen atoms, each with a different gas-phase acidity. We identify the deprotonation site by comparing the experimental photoelectron spectra with Franck-Condon simulations of the different possible isomers as well as comparing the measured EA and $\Delta_{acid}H$ values with

calculations, given in Table 5.4. We justify our assignment of the pyridinide, 1,2- and 1,3-diazinide anion isomers individually in the following results.

The remainder of the Results section is organized as follows: for each azine molecule studied, we identify the deprotonation site and give a brief summary of the photoelectron spectroscopy and gas-phase acidity measurements. The azines studied are presented in order of increasing nitrogen content: pyridine, the diazines, and 1,3,5-triazine. However, due to the similarity of the results for the five azines studied, we present the findings of one azine in detail: 1,3-diazine. We selected 1,3-diazine as the model azine because it highlights the major challenges and findings typical of the azine/azinide/azinyl systems.

Table 5.4 Calculated[a] EAs, $\Delta_{acid}H_{298}$s, and BDEs for Benzene and the Azines[b].
[a] Calculated using B3LYP/aug-cc-pVDZ

	$\Delta_{acid}H_{298}$ (kcal mol^{-1})	EA (eV)	BDE (kcal mol^{-1})
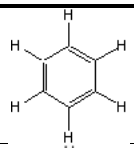 Benzene	399.2	1.095	110.9
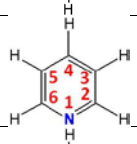 Pyridine(2)	399.4	0.854	105.5
Pyridine(3)	391.8	1.433	111.3
Pyridine(4)	389.7	1.469	110.0
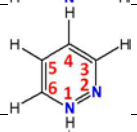 1,2-diazine(3)	389.8	1.342	107.1
1,2-diazine(4)	380.5	1.819	108.9
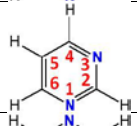 1,3-diazine(2)	396.2	1.072	107.3
1,3-diazine(4)	389.4	1.251	104.7
1,3-diazine(5)	383.7	1.824	112.2
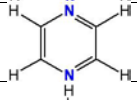 1,4-diazine	391.0	1.224	104.7
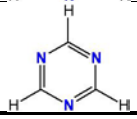 1,3,5-triazine	385.4	1.500	106.4

[b] If more than one isomer is possible for an anion/radical, number in parentheses indicates deprotonation site

5.3.1 Pyridinide, $C_5H_4N^-$

Pyridine has three possible anion isomers with very similar measured acidities for the hydrogen atoms at the 3- and 4-positions: 391.2 – 391.5 and 389.9(2.0) kcal mol^{-1} respectively.[15] Wenthold and coworkers also measured the regioselectivity of pyridine deprotonation under very similar experimental conditions as those used in this work and found 70 – 80% of the anions corresponded to pyridin-4-ide, and 20 – 30% were from pyridine-3-ide.[15]

Deprotonation from the 2-position, which is calculated to be the least acidic site in pyridine, was shown to be inaccessible under their experimental conditions. In our experiments, the pyridinide anion exchanged two hydrogen atoms with D_2O, duplicating the results by Schafman and Wenthold.[15] These results are consistent with the theoretical prediction (Table 5.4) that both the 2- and 3-position hydrogen atoms are sufficiently acidic to be accessed by HO^-. However, even though hydrogen atoms in the 2- and 3-positions have similar acidities, we expect to make primarily the pyridine-4-ide anion based on the branching ratios determined by Wenthold. This is supported by our simulations of the photoelectron spectra of the various pyridinide isomers; the experimental spectrum is clearly best reproduced by the pyridin-4-ide simulation shown in Figure 5.3b. Contribution from multiple isomers would result in a more congested spectrum than what we observe, indicating that only pyridine-4-ide contributes significantly to the photoelectron spectrum.

The measured EA of pyridin-4-yl is 1.480(6) eV, in excellent agreement with the calculated EA of 1.469 eV. We experimentally measure two vibrational frequencies of the pyridinyl radical, one at 600(20) cm^{-1} and another at 1010(50) cm^{-1}, and one frequency of pyridinide anion at 580(50) cm^{-1}. Using the previously reported $\Delta_{acid}H$ and the measured EA reported above, the C–H BDE for pyridine at the 4-position is 110.4(2.0) kcal mol^{-1}.

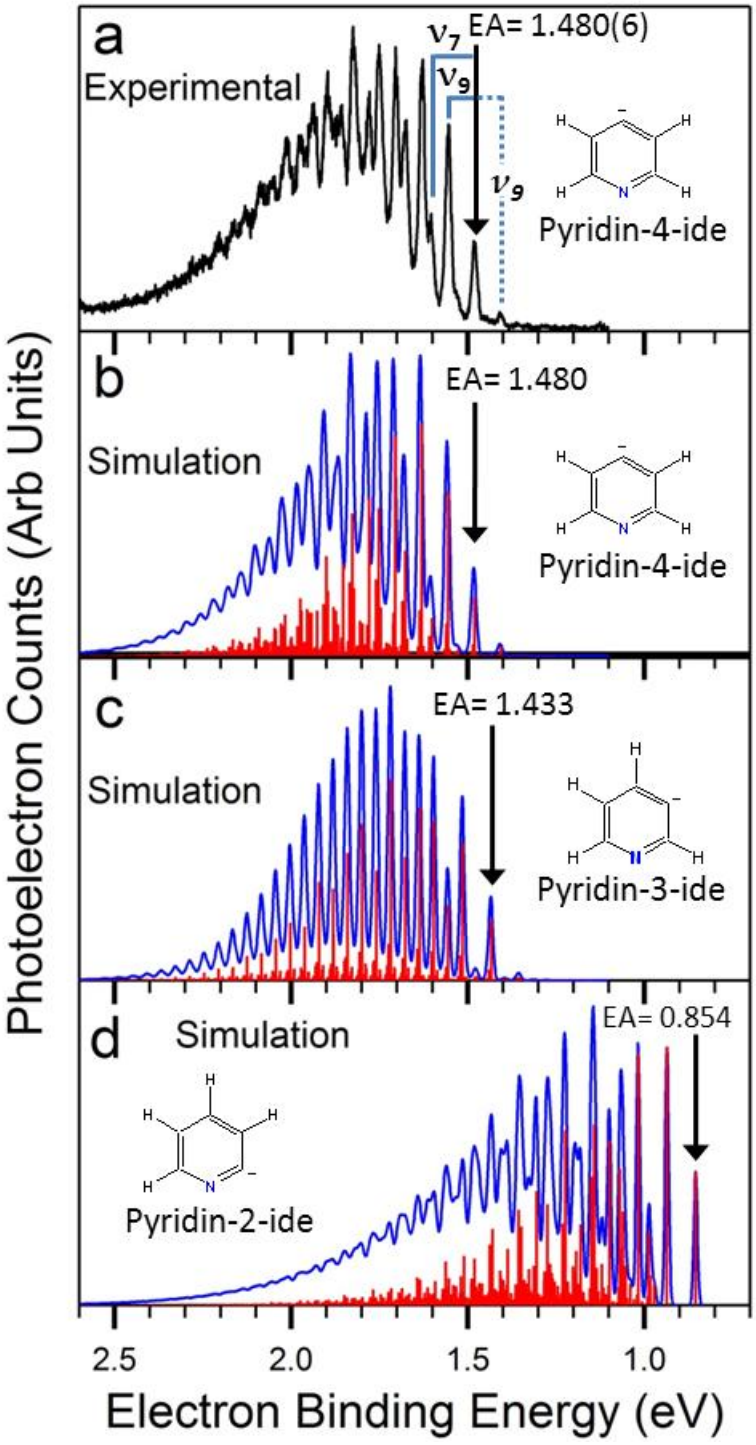

Figure 5.3 Magic-angle negative ion photoelectron spectra of pyridinide and simulations of possible anion isomers at 300 K. (a) 364-nm experimental spectrum; peaks used to identify experimental frequencies are indicated with solid lines (neutral frequencies) and dashed lines (anion frequency). Simulated photoelectron spectra of pyridin-4-ide (b), pyridine-3-ide (c), pyridine-2-ide (d).

5.3.2 1,3-Diazine, $C_4H_3N_2^-$

The analysis of 1,3-diazine results are more detailed than the other azine species in this chapter and is used to address many of the challenges and findings characteristic to the azines studied. The experimental 150 K magic-angle photoelectron spectrum of 1,3-diazinide is shown in Figure 5.4, along with Frank-Condon spectral simulations of the three possible 1,3-diazinide isomers. We confirm that we only observe contributions from one isomer by comparing our photoelectron spectra to the corresponding Franck-Condon simulations. In general, we can distinguish between signatures of different anion isomers if they have unique photoelectron spectra.[35-37] 1,3-Diazinide has three possible anion isomers, but as Figure 5.4 indicates, all three have dramatically different simulated photoelectron spectra. The simulation of 1,3-diazin-5-ide has nearly quantitative agreement with the experimental photoelectron spectrum, while neither the vibrational structure nor the calculated EA of 1,3-diazin-4-ide or 1,3-diazin-2-ide match the observed spectrum. We also compare the calculated $\Delta_{acid}H_{298}$ of each isomer with our experimental measurements. The hydrogen at the 2-position is calculated to be much less acidic (at least 6 kcal mol^{-1}) relative to the other hydrogen atoms at the 4 and 5 positions and, therefore, will be inaccessible in our experiment. The measured $\Delta_{acid}H_{298}$ of 384.6(7) kcal mol^{-1} is consistent with the calculated value of 383.7 kcal mol^{-1} for the hydrogen at the 5-position. Based on agreement between the experimental and simulated photoelectron spectra, as well as the agreement of the measured $\Delta_{acid}H_{298}$ with calculations, it is clear that only 1,3-diazin-5-ide contributes to our measurements.

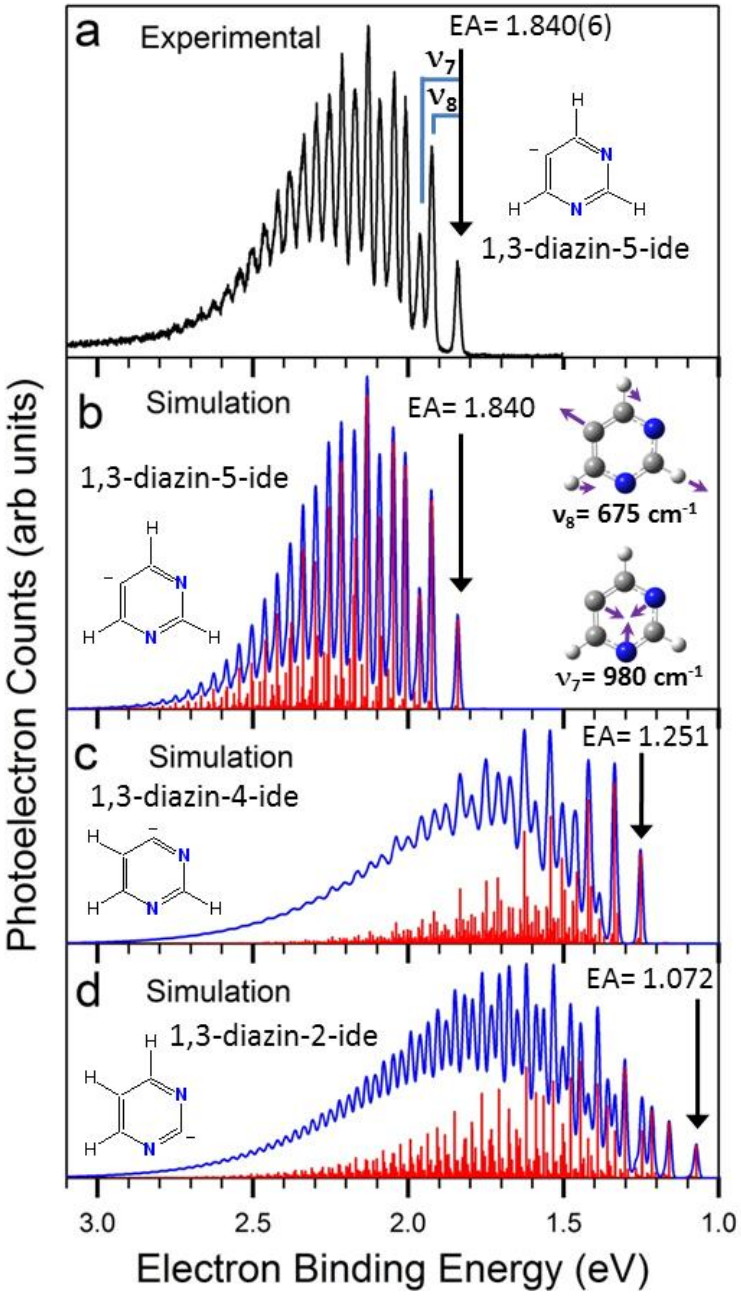

Figure 5.4 Magic-angle negative ion photoelectron spectrum of 1,3-diazinide. (a) 364-nm experimental spectrum with ions cooled to ~150 K. Peaks used to identify experimental frequencies are indicated with solid lines. (b) Simulated photoelectron spectrum at 150 K. Inset in (b) illustrates the calculated atomic displacements of the two most dominant vibrational modes, though all active modes are included in simulation. The simulated spectra for 1,3-diazin-4-ide and 1,3-diazin-2-ide are shown in (c) and (d) respectively.

Confident with our identification of 1,3-diazin-5-ide anion, we can now investigate the vibrational structure in the measured photoelectron spectrum. The spectrum of 1,3-diazinide was also collected at room temperature (not shown); the 300 K spectrum has a hot band at lower binding energy than the origin transition, from which we directly measure one vibrational frequency of the anion, 660(40) cm^{-1}. The photoelectron spectrum in Figure 5.4a has two dominant vibrational progressions that yield two vibrational frequencies of the neutral 1,3-diazin-5-yl radical, 680(20) and 980(20) cm^{-1}. Chemical insight and *ab initio* calculations enable assignment of these frequencies to vibrational normal modes. Table 5.5 lists the calculated vibrational modes for 1,3-diazin-5-ide anion and 1,3-diazin-5-yl radical, along with a qualitative description of the atomic motion and the experimental measurements for the photoelectron spectrum.

In general, progressions observed in photoelectron spectroscopy are from vibrational modes with atomic displacements that reflect the change in equilibrium geometry from the anion to the neutral. The location of the excess electron in the anion has a large effect on the equilibrium geometry; in 1,3-diazin-5-ide, there are two electrons localized on the 5-carbon atom. This causes the $\angle C_4C_5C_6$ bond angle to be smaller and the two adjacent C–C bond lengths to be larger than in the corresponding radical, which does not have to accommodate the excess charge. This prediction is confirmed by our calculations that indicate a +12.3° change in the $\angle C_4C_5C_6$ bond angle, and a 0.035 Å decrease in the adjacent C–C bond length upon photodetachment. Therefore, we expect that the observed vibrational progressions will correspond to totally symmetric vibrations that involve changes in the $\angle C_4C_5C_6$ angle and the C_4–C_5 and C_6–C_5 bond length. The moderate geometry change between the 1,3-diazin-5-ide

anion and neutral 1,3-diazin-5-yl radical results in the observed extended vibrational progression spanning approximately 1 eV.

Table 5.5 Calculated and Experimental Vibrational Frequencies for 1,3-diazin-5-ide ($^1A_1$) and 1,3-diazin-5-yl ($^2A_1$).

Mode		Description	Calculations[a] (cm^{-1})		Experiment[b] (cm^{-1})	
			Anion	Neutral	Anion	Neutral
A1	ν_1	sym H str	3087	3182		
	ν_2	sym H str	3035	3175		
	ν_3	sym ip ring deformation	1475	1513		
	ν_4	N-C-N sym str + H-wag	1412	1409		
	ν_5	sym ip ring deformation	1156	1126		
	ν_6	sym ring breathing	1075	1081		
	ν_7	sym ip ring deformation	975	989		980(20)
	ν_8	sym ip ring deformation	673	688	657(40)	675(20)
A2	ν_9	asym o-o-p H-wag	995	972		
	ν_{10}	o-o-p ring deformation	330	400		
B1	ν_{11}	asym o-o-p H-wag	962	1000		
	ν_{12}	o-o-p ring deformation	866	895		
	ν_{13}	o-o-p ring deformation	764	700		
	ν_{14}	o-o-p ring puckering	345	376		
B2	ν_{15}	asym H str	3035	3179		
	ν_{16}	asym ip ring deformation	1559	1598		
	ν_{17}	asym ip H-wag	1392	1435		
	ν_{18}	asym ip H-wag	1343	1331		
	ν_{19}	asym ip ring deformation	1223	1250		
	ν_{20}	asym ip ring deformation	1169	1158		
	ν_{21}	asym ip ring deformation	652	568		

[a] Used GAUSSIAN03 B3LYP/aug-cc-pVDZ where all frequencies are harmonica and unscaled, this work
[b] Experimental, this work

Based on our calculations, there are eight possibly active totally symmetric A_1 vibrational modes in 1,3-diazinyl radical, which are listed in Table 5.5. However, only two vibrational modes (ν_7 and ν_8) have frequencies that are low enough to correspond to the experimentally measured values. We assign the first three peaks in the 1,3-diazin-5-ide spectrum to the origin and to the ν_7 and ν_8 fundamental transitions (7_0^1 and 8_0^1 respectively). The remaining peaks are either sequence or overtone bands. The two dominant active modes involve symmetric in-plane ring distortions, illustrated in the inset of Figure 5.4b. These two types of symmetric ring deformation modes are representative of the active modes in the other four azinyl systems, and the measured frequencies in Table 5.2 are grouped accordingly.

Both the experimental and simulated spectra of 1,3-diazin-5-ide show a resolved and nearly harmonic vibrational progression. The resolved structure is due to the fact that only a few normal modes have activity, and their vibrational progressions do not overlap. The simulation also indicates that most of the peaks in the photoelectron spectrum owe their intensity largely to single vibronic transitions (the red sticks in Figure 5.4b – c correspond to the Franck-Condon factors). This produces resolved structure throughout the entire progression. The near equal spacing in each vibration progression is in part due to the rigidity of the aromatic ring, which constrains the extent of the atomic displacements upon photodetachment, leading to nearly harmonic vibrational modes. In addition, the independent harmonic-oscillator approximation used to model the photoelectron spectra works extremely well, which indicates that the normal modes are predominantly uncoupled. In contrast, we have found that even in much smaller molecular systems (such as dihalomethyl radicals (CHX_2)[38] and triplet states of the halocarbenes (CX_2)[39]) large geometry changes and "soft" vibrational potentials can lead to spectra that are congested and extremely difficult to interpret.

Using methanol as a reference acid, the acidity of 1,3-diazine was determined to be $\Delta_{acid}G_{298}$(1,3-diazine) = 376.8(7) kcal mol^{-1} and $\Delta_{acid}H_{298}$(1,3-diazine) = 384.6(7) kcal mol^{-1}. Combining the enthalpy of deprotonation with the EA for 1,3-diazin-5-yl, we determine the C–H bond strength for the 5-position in 1,3-diazine to be 113.4(7) kcal mol^{-1}.

5.3.3 1,2-Diazine, $C_4H_3N_2^-$

The measured 300 K photoelectron spectrum of 1,2-diazinide is shown in Figure 5.5a. 1,2-Diazine has two unique hydrogen atoms that have very different calculated acidities; the hydrogen at the 4-position is ~ 9 kcal mol^{-1} more acidic than the 3-position. The simulation of 1,2-diazin-4-ide is presented in Figure 5.5b. From the excellent agreement of the measured origin and observed vibrational structure with the calculated EA and the Franck-Condon simulation, it is clear that we only measure contributions from 1,2-diazin-4-ide. Based on the calculated EA and Franck-Condon profile of 1,2-diazin-3-ide (Figure 5.5c), if there were any 1,2-diazin-3-ide ions present in the ion beam, we would expect to observe a broader vibrational progression at lower binding energy than what we observe experimentally.

The measured EA of 1,2-diazin-4-yl is 1.850(6) eV, which is in good agreement with the calculated value of 1.819 eV. The photoelectron spectrum yields two vibrational frequencies for the 1,2-diazinyl radical, one at 640(20) cm^{-1} and another at 1000(80) cm^{-1}, and one frequency for 1,2-diazinide anion at 620(50) cm^{-1}. However, we cannot definitively assign the peaks in the ~1000 cm^{-1} progression to a single vibrational mode as there are two totally symmetric modes (ν_{12} and ν_{13}) with nearly degenerate frequencies around 1000 cm^{-1}.

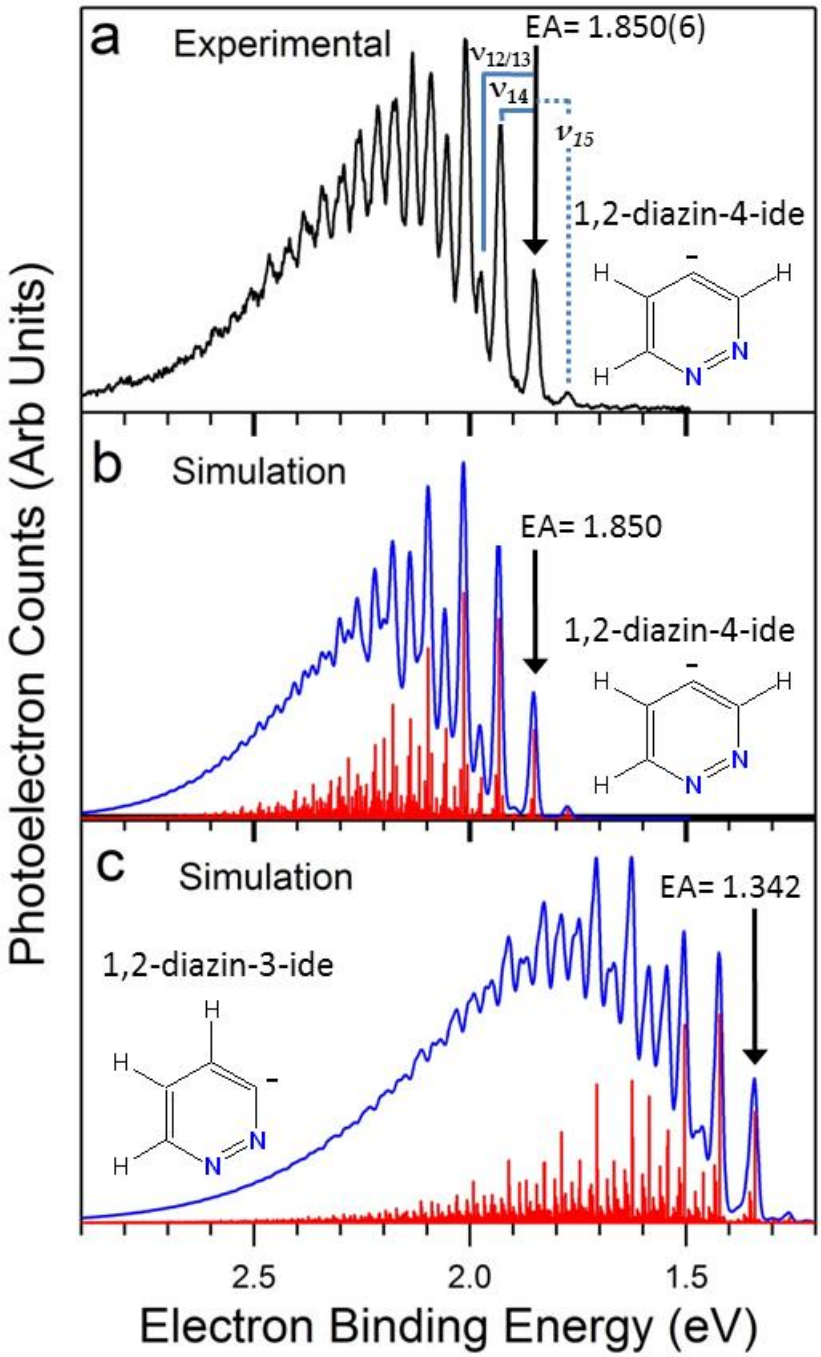

Figure 5.5 Magic-angle negative ion photoelectron spectra of 1,2-diazinide and simulations of possible anion isomers at 300 K. (a) 364-nm experimental spectrum; peaks used to identify experimental frequencies are indicated with solid lines (neutral frequencies) and dashed lines (anion frequency). The simulated spectra for 1,2-diazin-4-ide and 1,2-diazin-3-ide are shown in (b) and (c) respectively

The gas-phase acidity of $\Delta_{acid}G_{298}$(1,2-diazine) = 374.0(7) kcal mol^{-1} was measured with a corresponding enthalpy of deprotonation of $\Delta_{acid}H_{298}$(1,2-diazine) = 382.2(7) kcal mol^{-1}. Combining the measured enthalpy of deprotonation above with the EA for 1,2-diazin-4-yl, we determine the C–H bond strength for the 4-position in 1,2-diazine to be 111.3(7) kcal mol^{-1}.

5.3.4 1,4-Diazine, $C_4H_3N_2^-$

The four hydrogen atoms in 1,4-diazine are equivalent so there is only one possible 1,4-diazinide isomer. The measured EA of the 1,4-diazinyl radical is 1.254(6) eV, again in very good agreement with the calculated EA of 1.224 eV. We can experimentally identify one vibrational frequency of the 1,4-diazinyl radical, 700(20) cm^{-1}, and one frequency of the 1,4-diazinide anion, 670(50) cm^{-1}.

Using water as the reference acid, the acidity of 1,4-diazine is determined to be $\Delta_{acid}G_{298}$(1,4-diazine) = 383.5(4) kcal mol^{-1}, with a corresponding enthalpy of deprotonation $\Delta_{acid}H_{298}$(1,4-diazine) = 392.2(4) kcal mol^{-1}. From the measured enthalpy of deprotonation with the EA for 1,4-diazinyl, we determine the C–H bond strength for the 1,4-diazine to be 107.5(4) kcal mol^{-1}.

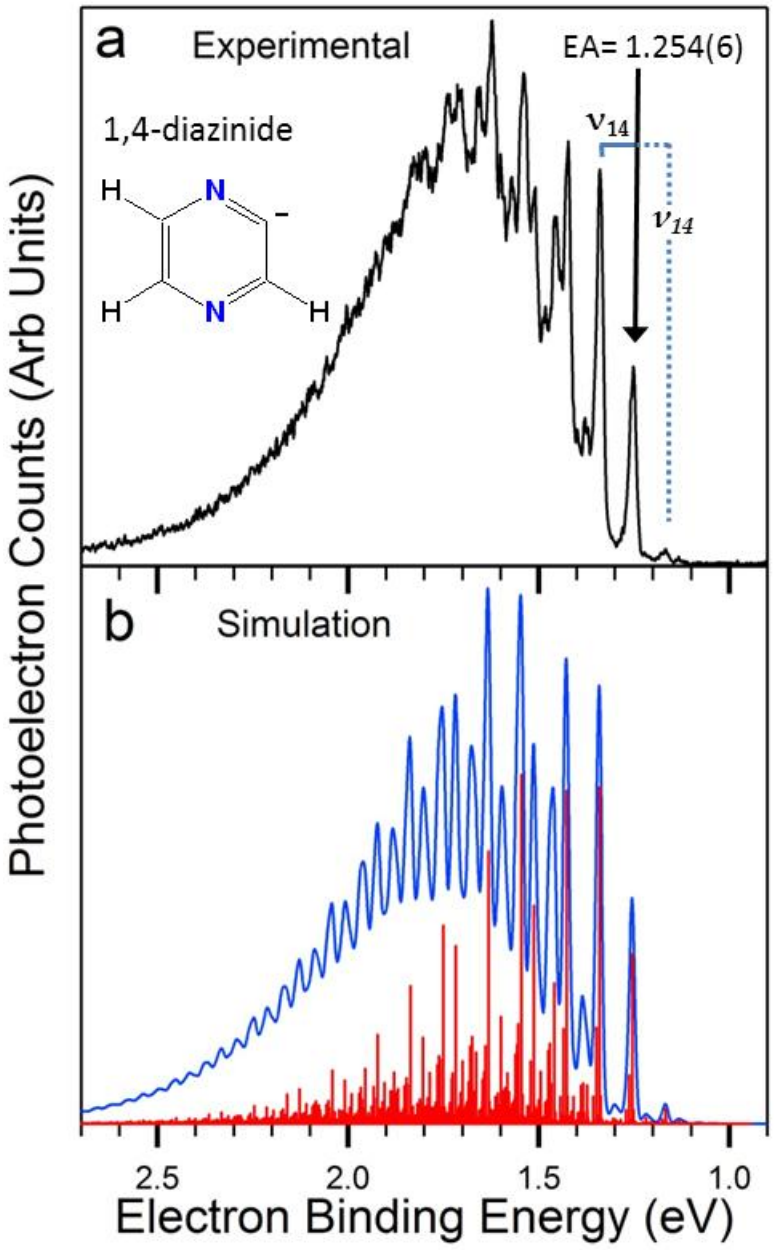

Figure 5.6 Magic-angle negative ion photoelectron spectrum of 1,4-diazinide. (a) 364-nm experimental spectrum with ion at 300 K. Peaks used to identify experimental frequencies are indicated with solid (neutral frequency) and dashed lines (anion frequency) (b) Simulated photoelectron spectrum at 300 K.

5.3.5 1,3,5-Triazine, $C_3H_2N_3^-$

The three hydrogen atoms in 1,3,5-triazine are equivalent, therefore there is only one possible 1,3,5-triazinide isomer. The measured EA of 1,3,5-triazinyl is 1.529(6) eV. We

experimentally measure two vibrational frequencies for the 1,3,5-triazinyl radical, 680(20) cm^{-1} and 1110(70) cm^{-1}, and one frequency for 1,3,5-triazinide anion, 670(40) cm^{-1}. As with 1,2-diazinyl, we cannot definitively assign the peaks in the ~1100 cm^{-1} progression to a single vibrational mode due to two modes (ν_4 and ν_5) with nearly degenerate frequencies around 1100 cm^{-1}.

Using methanol as the reference acid, we determine the acidity of 1,3,5-triazine to be $\Delta_{acid}G_{298}$(1,3,5-triazine) = 377.3(7) kcal mol^{-1}, and the corresponding enthalpy of deprotonation is $\Delta_{acid}H_{298}$(1,3,5-triazine) = 386.1(7) kcal mol^{-1}. Using the enthalpy of deprotonation with the EA for 1,3,5-triazinyl, we determine the C–H bond strength for 1,3,5-triazine to be 107.8(7) kcal mol^{-1}.

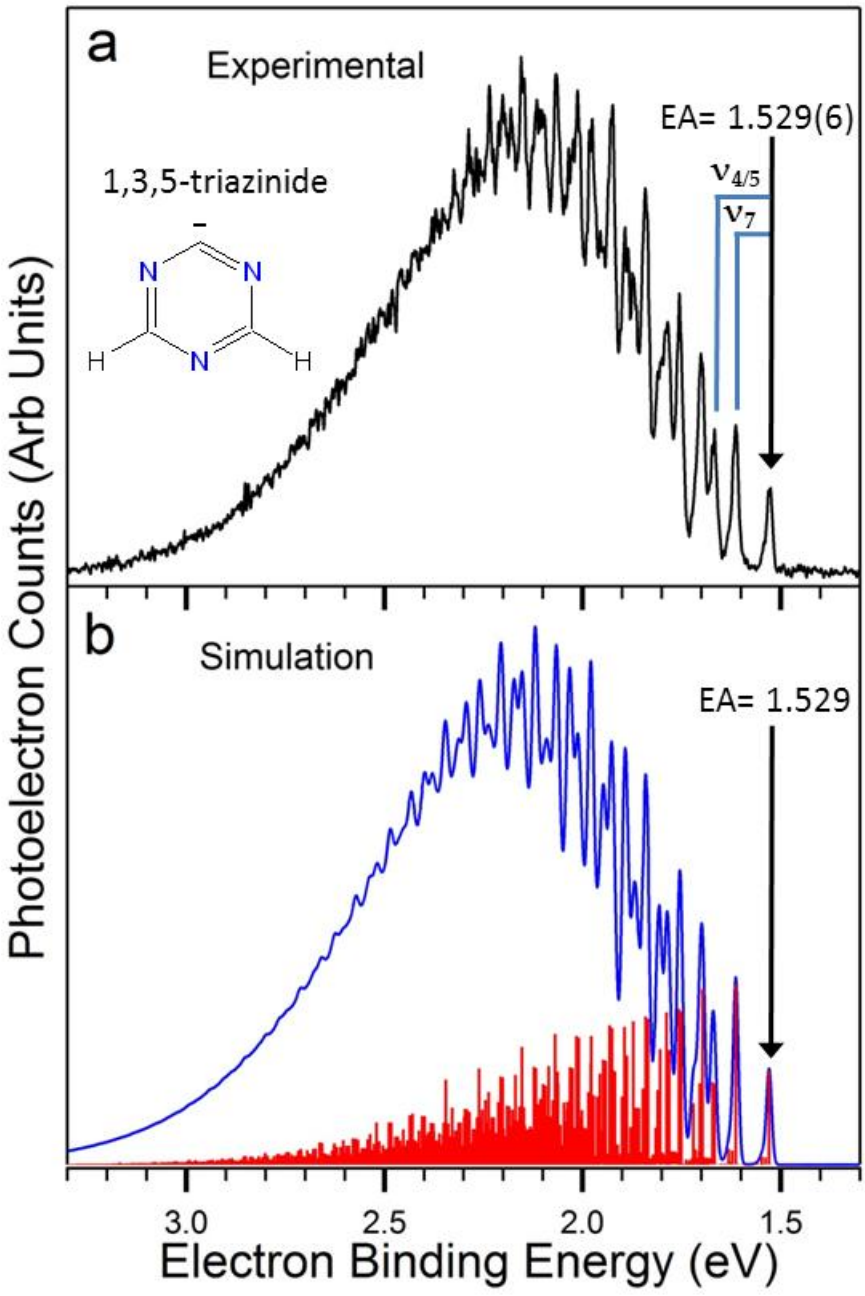

Figure 5.7 Magic-angle negative ion photoelectron spectrum of 1,3,5-triazinide. (a) 364-nm experimental spectrum with ion cooled to ~ 150 K. Peaks used to identify experimental frequencies are indicated with solid lines. (b) Simulated photoelectron spectrum at 150 K.

5.4 Discussion

In order to understand the effects of adding nitrogen atoms to six-membered rings, we will first compare pyridine with benzene; this is the simplest case in which only one nitrogen atom has been added. We then will systematically investigate and compare azines in order of increasing complexity and nitrogen content. By studying a series of azines with slight perturbations, namely the addition of nitrogen atoms, we can try to decouple what factors contribute to the stability of the azinide anions and the strength of C–H bonds.

Like benzene, pyridine is aromatic but replaces a C–H group with an electronegative nitrogen atom with a lone pair of electrons in an out-of-plane sp^2 hybridized orbital. This nitrogen insertion causes the hydrogen atoms in the 2-, 3-, and 4-positions – *ortho*, *meta*, and *para* respectively – to have drastically different measured acidities depending on proximity to the nitrogen atom.[15] In pyridine, the hydrogen in the *para* position is the most acidic, and is 11.3 kcal mol^{-1} more acidic than benzene. In fact, our results seem to agree with past findings that there are competing electrostatic effects that influence the stability of an azinide anion, and in turn the gas-phase acidity and EA.[15] Schafman suggested that forming an anion at the *para* position is favorable due to resonance stabilization.[15] This resonance picture is depicted in Scheme 5.1. The *ortho* position also benefits from resonance stabilization, but suffers from extensive electron-pair repulsion with the lone-pair electrons on the nitrogen atom, destabilizing the anion. In general, the relative stability of an anion can be inferred by the value of the deprotonation enthalpy. For example, if a specific azinide anion is very stable relative to the neutral azine molecule, then the proton at the anion site will be more acidic and the corresponding $\Delta_{acid}H$(R-H) value with be *lower*. Furthermore, since our experiments

preferentially deprotonate at the most acidic site in each azine, the anion that is formed will be the most stable relative to the other possible anion isomers.

Scheme 5.1

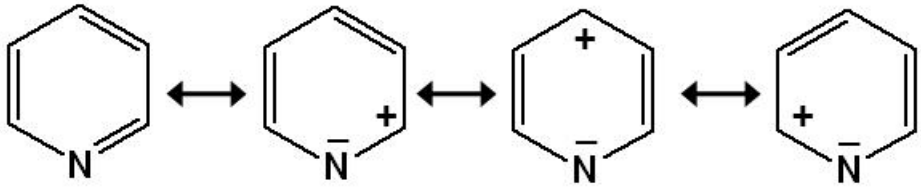

The EA of pyridin-4-yl radical is 1.480(6) eV, a ~ 50% increase from the measured EA of the phenyl radical of 1.096(6) eV. The measured EAs give us insight into the stability of an azinide anion relative to the neutral radical. The more energy required to photodetach the electron results in a larger EA and implies a more stable anion. With a smaller measured $\Delta_{acid}H$ and an increased EA, it appears that inserting a nitrogen atom into benzene acts to stabilize the anion *para* to the nitrogen. Finally, using both the EA and $\Delta_{acid}H$, we determined the *para* C–H bond strength, which is the energy required to homolytically cleave the C–H bond. We find the C–H bond in the *para*-position is slightly weaker than the C–H bond strength in benzene: 110.4(2.0) and 112.9(5), respectively. In general, the more stable the resulting azinyl radical is relative to the neutral azine, the lower the BDE.

The diazines, which contain two nitrogen atoms, provide insight into how increasing the nitrogen content within an azine affects its chemical properties. 1,4-Diazine is the simplest case where there is only one possible anion due to the symmetry of the two nitrogen atoms in the ring. Using pyridine as a guide, one would expect that forming an anion adjacent to a nitrogen atom would create a relatively unstable anion due to unfavorable lone-pair repulsion. This is indeed what we find, as the $\Delta_{acid}H$ is larger and the EA is smaller in 1,4-diazine as compared to our results for pyridine deprotonated at the *para* position. We also find that the C–H bond strength

in 1,4-diazine is ~2.6 kcal mol^{-1} weaker than the *para* C–H bond in pyridine. Previous studies on pyridin-2-yl have suggested that a radical adjacent to a nitrogen atom can be stabilized by a resonance interaction between the unpaired electron and the adjacent nitrogen lone pair.[9, 11, 12, 40] In other words, the adjacent nitrogen atom allows for additional resonance structures, serving to delocalize the unpaired electron and thereby stabilize the radical.[11] Therefore, a more stable 1,4-diazinyl radical would explain the lower BDE. We can conclude that there is a balancing of electrostatic effects between electron – lone-pair repulsion in the anion and resonance stabilization in the radical.

The other two diazines, 1,2- and 1,3-diazine, lack the symmetry of 1,4-diazine but share similar experimental results. In both cases, the most acidic site is the farthest away from the nitrogen atoms, the *meta*-position for both diazines. The photoelectron spectra in Figure 5.2 illustrate the similarity of the EAs – within 10 meV of each other – and that 1,2-diazin-4-yl and 1,3-diazin-5-yl have the largest EAs of any of the azines we studied. These results indicate that the anion formed from 1,2- and 1,3-diazine are very stable relative to the corresponding neutral azine or radical. Table 5.1 also indicates that the measured $\Delta_{acid}H$ values are smaller than any of the other azines we studied, further implying the stability of the 1,2-diazin-4-ide and 1,3-diazin-5-ide anions. Comparing the results from benzene and pyridine to the diazines, it also appears that the additional nitrogen plays a role in stabilizing the anion. However, it is very difficult to experimentally decouple which factors are most important. The C–H bond for 1,3-diazine at the 5-position is the strongest we measure with an BDE of 113.4(7) kcal mol^{-1}. The C–H bond in 1,2-diazine at the 4-position is only slightly weaker with a BDE of 111.3(7) kcal mol^{-1}. Unlike 1,4-dazinyl, the radical formed in both of these diazines has no additional resonance interaction with an adjacent nitrogen atom, thus both have bond strengths similar to benzene.

Lastly, 1,3,5-triazine is the special case where there are three nitrogen atoms inserted symmetrically into the six-membered ring. As with 1,4-diazine, only one possible anion can be formed, which will be adjacent to a nitrogen atom. But unlike 1,4-diazinide, the excess electron of 1,3,5-triazinide is adjacent to two nitrogen atoms, which should be very unfavorable if one only considers the effect of electron – lone-pair repulsion. However, the EA is ~ 0.3 eV (or ~ 7 kcal mol^{-1}) larger and the $\Delta_{acid}H$ is ~ 6 kcal mol^{-1} smaller than for 1,4-diazine. It would appear that lone-pair repulsion with the excess electron is not the dominant factor governing the EA of 1,3,5-triazinide.

Though our experimental measurements are limited to anions formed at the most acidic deprotonation site in an azine, we can use our calculations to compare chemical properties of azinide isomers. As shown in the results section, our experimental results agree very well with our calculations, giving us confidence in the calculations for the other isomers. 1,3-Diazine deprotonated at the 2-position forms an anion similar to 1,3,5-triazinide in that the excess electron of both anions is located between two nitrogen atoms. The $\Delta_{acid}H$ value for 1,3-diazine at the 2-position is 10 kcal mol^{-1} *larger* than what we measure in 1,3,5-triazine. Furthermore, the calculated EA of 1,3-diazin-2-yl is nearly 0.5 eV *smaller* than what we measure for 1,3,5-triazinyl. The comparison of the $\Delta_{acid}H$ and the EA values are both indicative of a less stable 1,3-diazin-2-ide anion. Thus, the additional nitrogen atom *para* to the anion in 1,3,5-triazinide must stabilize the anion in order to observe such a drastic decrease in the enthalpy of deprotonation and increase in the EA.

We can make several additional observations concerning the C–H bond strengths in the azines we studied by combining our experimental observations with our calculations. Table 5.4 summarizes the calculated results for all possible isomers created by single deprotonation of the

azine species in this work. Our experimental results indicate that the C–H bond strength is the weakest when adjacent to and strongest when removed from a nitrogen atom. The calculated results support this finding; in pyridine, 1,2-diazine, and 1,3-diazine, the weakest bond is indeed adjacent to a nitrogen atom. Furthermore, the most acidic deprotonation site generally corresponds to the strongest C–H bond with the largest BDE value. Even though we find that the BDEs vary depending on the proximity to a nitrogen atom, all six measured BDEs in Table 5.1 only span a narrow 6 kcal mol^{-1} range.

5.5 Conclusion

Five azine molecules were investigated by both negative ion photoelectron spectroscopy and ion kinetics using a FA-SIFT. We were able to, for the first time, measure EAs for five azinyl radicals, as well greatly improve the accuracy of the deprotonation enthalpies for four azine molecules. The measured acidities and EAs are accounted for based on electrostatic arguments where certain anion sites are preferentially stabilized by resonance while others are destabilized by electron pair repulsion. However, as the nitrogen content increases in the diazines and 1,3,5-triazine, there is a balancing of these competing effects which are manifested in our results. We determined site-specific BDE for all five azines, including the first experimental measurements for 1,2-diazine and 1,3,5-triazine. The results suggest that the proximity of the C–H bond to a nitrogen atom has a greater influence on the thermochemistry (EA, BDE, $\Delta_{acid}H_{298}$) than the number of nitrogen atoms in the azine. Furthermore, we found that C–H bonds adjacent to a nitrogen atom have lower BDE relative to C–H bonds *meta* or *para* to the nitrogen.

5.6 References

1. Smith, K.L., et al., eds. *The Structure and Reaction Processes of Coal*. 1994, Plenum Press: New York.
2. Wallace, S., K.D. Bartle, and D.L. Perry, *Quantification of nitrogen functional groups in coal and coal derived products.* Fuel, 1989. **68**(11): p. 1450-1455.
3. Hore, N.R. and D.K. Russell, *Radical pathways in the thermal decomposition of pyridine and diazines: a laser pyrolysis and semi-empirical study.* Journal of the Chemical Society-Perkin Transactions 2, 1998(2): p. 269-275.
4. Axworthy, A.E., V.H. Dayan, and G.B. Martin, *Reactions of fuel-nitrogen compounds under conditions of inert pyrolysis.* Fuel, 1978. **57**(1): p. 29-35.
5. Pohl, J.H. and A.F. Sarofim, *Devolatilization and oxidation of coal nitrogen.* Symposium (International) on Combustion, 1977. **16**(1): p. 491-501.
6. Fried, L.E., et al., *Design and synthesis of energetic materials.* Annual Review of Materials Research, 2001. **31**(1): p. 291-321.
7. Turker, L., S. Gumus, and T. Atalar, *A DFT Study on Nitro Derivatives of Pyridine.* Journal of Energetic Materials, 2010. **28**(2): p. 139-171.
8. FinlaysonPitts, B.J. and J.N. Pitts, *Tropospheric air pollution: Ozone, airborne toxics, polycyclic aromatic hydrocarbons, and particles.* Science, 1997. **276**(5315): p. 1045-1052.
9. Doughty, A. and J.C. Mackie, *Kinetics of thermal-decompotion of the diazines – shock-tube pyrolysis of pyrimidine.* Journal of the Chemical Society-Faraday Transactions, 1994. **90**(4): p. 541-548.
10. Jones, J., et al., *Ab-initio studies of the thermal-decomposition of azaaromatics- Free-radical versus intermolecular mechanism.* Journal of the Chemical Society-Faraday Transactions, 1995. **91**(11): p. 1587-1592.
11. Kiefer, J.H., et al., *Pyrolyses of aromatic azines: Pyrazine, pyrimidine, and pyridine.* Journal of Physical Chemistry A, 1997. **101**(38): p. 7061-7073.
12. Mackie, J.C., M.B. Colket, and P.F. Nelson, *Shock-tube pyrolysis of pyridine.* Journal of Physical Chemistry, 1990. **94**(10): p. 4099-4106.
13. Mackie, J.C., et al., *Shock-tube Pyrolysis of Pyrrole and Kinetic Modeling.* Int. J. Chem. Kinet., 1991. **23**(8): p. 733.
14. Xu, H. and J.H. Kiefer, *Shock Tube Study of 1,3,5-Triazine Dissociation and Relaxation and Relaxation of Pyrazine.* International Journal of Chemical Kinetics, 2010. **42**(4): p. 211-220.
15. Schafman, B.S. and P.G. Wenthold, *Regioselectivity of pyridine deprotonation in the gas phase.* Journal of Organic Chemistry, 2007. **72**(5): p. 1645-1651.

16. Garver, J., et al., *Gas Phase Reactions of 1,3,5-Triazine: Proton Transfer, Hydride Transfer, and Anionic σ-Adduct Formation.* Journal of the American Society for Mass Spectrometry, 2011. **22**(7): p. 1260-1272.

17. Barckholtz, C., T.A. Barckholtz, and C.M. Hadad, *C-H and N-H bond dissociation energies of small aromatic hydrocarbons.* J. Am. Chem. Soc., 1999. **121**(3): p. 491.

18. Ervin, K.M. and V.F. DeTuro, *Anchoring the gas-phase acidity scale.* Journal of Physical Chemistry A, 2002. **106**(42): p. 9947-9956.

19. Davico, G.E., et al., *The C-H bond-energy of benzene.* Journal of the American Chemical Society, 1995. **117**(9): p. 2590-2599.

20. Gunion, R.F., et al., Int. J. Mass Spectrom. Ion Processes, 1992. **117**: p. 601.

21. Meotner, M. and S.A. Kafafi, *Carbon acidities of aromatic-compounds.* Journal of the American Chemical Society, 1988. **110**(19): p. 6297-6303.

22. Wenthold, P.G., et al., *Transition-state spectroscopy of cyclooctatetraene.* Science, 1996. **272**(5267): p. 1456-1459.

23. We chose to not repeat the acidity measurement for pyridine since it seemed unlikely we could improve on the measurement make by Schafman and Wenthold. Reactivity measurements and exchange reactions with D_2O were consistent with Schafman's findings.

24. Van Doren, J.M., et al., *The tandem flowing afterglow-sift-drift.* International Journal of Mass Spectrometry and Ion Processes, 1987. **81**: p. 85-100.

25. Bierbaum, V.M., *Theory and Ion Chemistry*, in *Encyclopedia of Mass Spectrometry*, M.L. Gross and R. Caprioli, Editors. 2003, Elsevier: Amsterdam. p. 276.

26. Wren, S.W., et al., *Nitrogen Proximity Effects in Azines: How Nitrogen Atoms Affect C–H Bond Strengths and Anion Stability.* In Preparation.

27. Frisch, M.J., et al., *Gaussian 03, Revision B.05*2003, Pittsburgh: Gaussian, Inc.

28. Becke, A.D., *Density-functional thermochemistry. III. The role of exact exchange.* Journal of Chemical Physics, 1993. **98**(7): p. 5648-5652.

29. Lee, C.T., W.T. Yang, and R.G. Parr, *Development of the colle-salvetti correlation-energy formula into a functional of the electron density.* Physical Review B, 1988. **37**(2): p. 785-789.

30. Woon, D.E. and T.H. Dunning, *Gaussian-Basis Sets for Use in Correlated Molecular Calculations .3. the Atoms Aluminum through Argon.* Journal of Chemical Physics, 1993. **98**(2): p. 1358-1371.

31. Dunning, T.H., *Gaussian-basis sets for use in correlated molecular calculations. 1. The atoms boron through neon and hydrogen.* Journal of Chemical Physics, 1989. **90**(2): p. 1007-1023.

32. Ervin, K.M., *PESCAL, Fortran program.* PESCAL, Fortran program, 2010.

33. Ervin, K.M., et al., *Naphthyl radical: Negative ion photoelectron spectroscopy, Franck-Condon simulation, and thermochemistry.* J. Phys. Chem. A, 2001. **105**(48): p. 10822.

34. Gunion, R.F., et al., *Ultraviolet photoelectron-spectroscopy of the phenide, benzyl and phenoxide anions, with ab initio calculations.* International Journal of Mass Spectrometry and Ion Processes, 1992. **117**(1-3): p. 601-620.

35. Ichino, T., et al., *Structure of the vinyldiazomethyl anion and energetic comparison to the cyclic isomers.* Journal of Physical Chemistry A, 2007. **111**(34): p. 8374-8383.

36. Villano, S.M., et al., *Photoelectron spectroscopy and thermochemistry of the peroxyacetate anion.* European Journal of Mass Spectrometry, 2010. **16**(3): p. 255-268.

37. Villano, S.M., et al., *Photoelectron Spectroscopy and Thermochemistry of the Peroxyformate Anion.* Journal of Physical Chemistry A, 2010. **114**(1): p. 191-200.

38. Vogelhuber, K.M., et al., *Photoelectron spectra of dihalomethyl anions: Testing the limits of normal mode analysis.* The Journal of Chemical Physics, 2011. **134**(18): p. 184306-13.

39. Wren, S.W., et al., *The photoelectron spectrum of CCl_2^-: the convergence of theory and experiment after a decade of debate.* Physical Chemistry Chemical Physics, 2009. **11**(23): p. 4745-4753.

40. Kikuchi, O., et al., *An ab initio molecular-orbital study of pyridyl radicals.* Bulletin of the Chemical Society of Japan, 1988. **61**(1): p. 291-292.

6 Photoelectron Spectroscopy of Dihalocarbenes: CCl_2^-, CBr_2^- and CI_2^-

6.1 Introduction

Carbenes are highly reactive diradicals with two electrons occupying nearly degenerate σ and π orbitals. They serve as intermediates in many chemical reactions, including addition to a double bond, insertion into a single bond, dimerization, and intramolecular rearrangement.[1-4] The nature of the substituents affects whether the electronic configuration of the ground state is a σ^2 singlet or a diradical $\sigma^1\pi^1$ triplet.[4] The singlet $^1A_1$ and triplet $^3B_1$ states lie close in energy but exhibit very different reactivities, so the difference in energy between the two states (ΔE_{ST}) is a quantity of great interest. Furthermore, dihalocarbenes have served as test cases for comparing experimental and theoretical energy splittings. For these reasons, carbenes have drawn attention from both experimental and theoretical research groups for decades. The simplest carbene possesses a single carbon atom, **:**CXY; methylene, **:**CH_2 and the halocarbenes have accordingly been the subject of numerous experimental and theoretical investigations.[5]

Singlet-triplet energy splittings are difficult to determine experimentally.[4] Though the singlet ground states of the dihalocarbenes have been well-characterized,[6-18] spectroscopic methods are commonly unable to interrogate states of different multiplicity, making ΔE_{ST} an elusive quantity. Extensive theoretical work has been done to calculate ΔE_{ST} of the dihalocarbenes. In the late 1980s, Carter and Goddard[19-21] carried out one of the first thorough studies to determine the magnitude of ΔE_{ST} of neutral dihalocarbenes. More calculations

followed,[22-25] and the computational results reached a consensus that the $^3B_1$ states of CCl_2, CBr_2, and CI_2 lie 10 – 35 kcal mol^{-1} higher in energy than their respective $^1A_1$ ground states.

Anion photoelectron spectroscopy has been shown to be an important, direct method for measuring ΔE_{ST}.[26, 27] In 1999, Lineberger and co-workers investigated the series of dihalocarbenes CX_2 (X = F, Cl, Br, I) with this technique.[28] The singlet-triplet splitting obtained from the spectrum of CF_2^- (ΔE_{ST} = 54(3) kcal mol^{-1})[28] agreed with theoretical predictions (ΔE_{ST} = 56.9(7) kcal mol^{-1}),[29] but the energy splittings for the heavier dihalocarbenes did not.[29] Theorists calculated a ΔE_{ST} of ~ 20 kcal mol^{-1} for CCl_2 and ~ 17 kcal mol^{-1} for CBr_2,[22-25] while the photoelectron spectra implied substantially lower ΔE_{ST} values: 3(3) kcal mol^{-1} for CCl_2, and 2(3) kcal mol^{-1} for CBr_2. Recently, more sophisticated calculations have followed as rapid advances in theory have been made.[29-37] Of particular interest was CCl_2, the most computationally tractable of the dihalocarbenes. Notably, Dyke and co-workers performed a combined *ab initio*/Franck-Condon study to simulate the CCl_2^- photoelectron spectrum.[35] All calculations yielded the larger ΔE_{ST} values, consistent with the earlier theoretical studies. This discrepancy between theory and experiment prompted us to carry out a careful reinvestigation of the photoelectron spectra of the dihalocarbenes, particularly CCl_2^-.

We have carefully examined the chemistry taking place in the ion source, and identified contamination from $CHCl_2^-$ in the previously reported CCl_2^- spectrum; the spectrum of this contaminant unexpectedly obscured the triplet band origin of CCl_2 and resulted in an erroneous determination of $\Delta E_{ST}(CCl_2)$. In the current study, we collect the photoelectron spectrum of pure $CHCl_2^-$ and minimize its contribution to elucidate the CCl_2^- experimental data.[38] We present the 351 nm photoelectron spectrum of CCl_2^- that exhibits vibrationally resolved transitions to singlet and triplet electronic states, yielding substantially improved agreement with

high-level calculations. We then show that the halomethyl anions $CHBr_2^-$ and CHI_2^- also had contaminated the previous photoelectron spectra of CBr_2^- and CI_2^-.[28] The material in the Chapter is largely based upon two recent publications from this laboratory.[38, 39]

6.2 Experimental Method

The negative ion photoelectron spectrometer used in this experiment has been described in detail in Chapter 2. Negative ions are formed in a flowing afterglow ion source. A microwave discharge containing trace amounts of O_2 gas in He buffer gas (~ 0.4 Torr) generates atomic oxygen radical anion, O^-. The appropriate CH_2X_2 dihalomethane precursor (CH_2Cl_2, CH_2Br_2, or CH_2I_2, Sigma-Aldrich) is added downstream, where it can undergo a variety of reactions with O^-: H_2^+ abstraction to produce CX_2^- + H_2O, H^+ abstraction to produce CHX_2^- + OH, O addition to produce X^- + OCH_2X, and H abstraction to produce OH^- + CHX_2. Collisions with helium buffer gas vibrationally cool the ions to approximately 300 K. As described in more detail later, we employ a different reaction sequence using hydroxide (OH^-) reactant ion to produce exclusively CHX_2^- dihalomethyl anions exclusively. The flow tube can be cooled with a liquid nitrogen jacket to obtain a cold spectrum of ions with vibrational temperatures near 200 K. The original Wien velocity filter, with a mass resolution of $m/\Delta m$ ~ 40, was used in these experiments. The typical ion current for the mass-selected ion beam of CX_2^- and CHX_2^- is between 200 and 500 pA. Here, the ~ 0.5 W output from a single-mode continuous-wave argon ion laser operating at either 351 nm (3.531 eV) or 364 nm (3.408 eV) is built up to approximately 50 W of circulating power in an optical buildup cavity located within the vacuum system. The energy analyzer resolution for these experiments was approximately 12 meV. However, after accounting for the resolution of the spectrometer and rotational peak profiles, absolute electron binding energies can be determined with an accuracy of 5 meV or better.[40] A

rotatable half-wave plate positioned outside the buildup cavity controls the polarization of the photodetachment radiation. All spectra shown here were collected with magic angle polarization unless otherwise noted.

6.3 Theoretical Methods

Electronic structure calculations were carried out using the Gaussian 03 software package.[41] All calculations for CCl_2 use the coupled-cluster CCSD(T) method[42] with an augmented correlation-consistent polarized triplet-zeta basis set (aug-cc-pVTZ).[43, 44] Calculations for CBr_2 were performed with density functional theory at the B3LYP/6-311++G(d,p) level.[45, 46] Geometries were optimized and harmonic vibrational frequencies and normal mode coordinates were calculated for the doublet anion and the singlet and triplet neutral states. Calculated harmonic frequencies are reported without applying a scaling factor.

The Franck-Condon profiles of the photoelectron spectra are simulated using the PESCAL program, which was modified recently in order to simulate transitions among multiple electronic states simultaneously.[47] The simulations start with the theoretical geometries, normal mode vectors, and vibrational frequencies of the anion and neutral states. For the $X\ ^1A_1$ CCl_2 and $X\ ^1A_1$ CBr_2 singlet states, however, the harmonic frequencies, anharmonicities, and geometries from high-resolution spectroscopy experiments[14, 17, 18, 48, 49] (Tables 2 and 3) are used in the simulations instead of the calculated values. For the singlet state transitions, the anharmonicities are significant and known experimentally, whereas the calculated Duschinsky rotation angles between normal mode vectors of the two active are modest (5.3° for CCl_2 and 9.6° for CBr_2). Therefore, the Franck-Condon factors for the singlet state are calculated in the Morse oscillator, parallel mode approximation using numerically integrated Laguerre polynomial wavefunctions.[50] For the CCl_2 triplet state transition, the anharmonicities are unknown

experimentally, and the calculated Duschinsky rotation angle is significant (17.5°), so the Franck-Condon factors are calculated in the harmonic oscillator approximation but including Duschinsky rotation using the Sharp-Rosenstock-Chen method.[51, 52]

The individual vibronic peak contours are obtained by calculating the rotational spectrum, treating the molecules approximately as prolate tops, and convoluting the rotational transitions with the instrumental resolution function, approximated as a Gaussian function with a FWHM of 12 meV. This procedure directly accounts for the small (typically < 4 meV) displacement of the rotationless origin of a peak from the location of its maximum intensity. Finally, the normal mode displacements between the anion and the neutral for the Franck-Condon active modes (symmetric stretch and bend), along with the positions of the origin transitions, are adjusted from the theoretical values to match the experimental spectra.

The Wien filter partially resolves the $^{12}C^{35,37}Cl_2^-$ and $^{12}C^{79,81}Br_2^-$ ions; calculated frequencies and rotational constants indicate that the presence of more than one isotope will produce negligible broadening. Thus, isotope issues are neglected in the analysis.

6.4 Results and Discussion: Dihalocarbene Anions (CX_2^-)

In the previous dihalocarbene studies and in the work presented in this paper, the dihalocarbene target anions are produced by reacting O^- with CH_2X_2 (X=Cl, Br, I).[53] As a specific example, reactions involving CH_2Cl_2 are described in detail below. A variety of reactions occur when O^- reacts with CH_2Cl_2 at 300 K, leading to the formation of products with the following branching fractions:[53]

Scheme 4.1

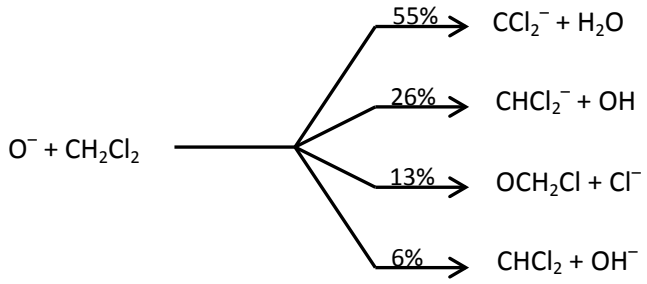

Abstraction of H_2^+ by O^- occurs with 55% yield to produce the desired CCl_2^-; however, $CHCl_2^-$ produced by proton abstraction, with *m/z* only 1 amu greater than the desired product, is a significant minor ionic reaction product. Since the Wien filter has a mass resolution of at best $m/\Delta m \sim 40$, we can only partially separate ions within 1 amu of each other at *m/z* ~ 80, specifically CCl_2^- and $CHCl_2^-$. It was initially anticipated that the electron affinity of $CHCl_2$ was sufficiently low that it would not be an important contaminant in the CCl_2^- photoelectron spectrum. However, the significant difference between the experimental[28] and calculated[35] photoelectron spectra of CCl_2^-, as well as of the heavier dihalocarbenes,[31] have led us to investigate the dihalomethyl anionic product of this reaction as a possible cause of the discrepancy.

In order to evaluate the $CHCl_2^-$ contribution to the CCl_2^- spectrum, we replace O^- with OH^- in the above reaction. Only the dihalomethyl anionic product is now formed, as described in Chapter 2

Scheme 4.2

$$OH^- + CH_2Cl_2 \longrightarrow CHCl_2^- + H_2O$$

Sufficient methane is added to ensure complete removal of O^- before CH_2Cl_2 is introduced into the ion source region in order to guarantee that $CHCl_2^-$ is the only species present near *m/z* ~ 83.

The photoelectron spectrum of $CHCl_2^-$ is remarkably broad and exhibits extensive vibrational structure, and will be analyzed further in Section 6.5. Comparison with the earlier data shows conclusively that dihalomethyl anion contamination was present in the previously reported photoelectron spectrum of CCl_2^- and is responsible for the bulk of the progression previously attributed[28] to the triplet state of CCl_2. Spectra of $CHBr_2^-$ and CHI_2^-, similarly broad and highly structured, overlap with the spectra of the corresponding dihalocarbene anion, indicating that dihalomethyl anion contamination was also present in the photoelectron spectra of CBr_2^- and CI_2^-.[28]

We take several steps to obtain dihalocarbene anion photoelectron spectra with minimal contamination. We first minimize CHX_2^- contribution to the contaminated spectrum by tuning the Wien mass filter to 50% of the maximum ion signal on the low-mass side of the appropriate unresolved mass peak. In the synthesis of CCl_2^-, we took the additional step of using deuterated dichloromethane precursor (CD_2Cl_2) to increase the mass difference between CCl_2^- and $CDCl_2^-$, improving our ability to separate the two ions with the Wien filter. As this approach is less effective for the heavier dihalocarbenes, CH_2Br_2 and CH_2I_2 precursors were used to make CBr_2^- and CI_2^-, respectively. Next, the appropriately scaled authentic CHX_2^- photoelectron spectrum is subtracted from the two-component spectrum. The multiple peaks that are attributable solely to dihalomethyl anion are used to determine the scaling factor. The final constraint is that the scaling factor must leave the subtracted spectrum everywhere non-negative. As discussed below,

this procedure was applied to each of the dihalocarbenes, but the amount of new information gained diminished for the heavier dihalocarbenes.

6.4.1 CCl_2^-

We obtain a 351-nm photoelectron spectrum of CCl_2^- that clearly resolves both the $X\ ^1A_1$ and $a\ ^3B_1$ electronic states of the carbene. By tuning the Wien filter to the low-mass side of the mass peak containing both CCl_2^- and $CDCl_2^-$, the dihalomethyl anion contribution to the photoelectron spectrum is considerably reduced from that previously reported.[28] Figure 6.1a shows the previous 364 nm photoelectron spectrum reported by Schwartz *et al.*[28] Figure 6.1b depicts the new 351 nm spectrum that contains signal from both CCl_2^- and $CDCl_2^-$ (black trace). The 351 nm pure $CDCl_2^-$ photoelectron spectrum obtained under the same experimental conditions is shown in red in Figure 6.2b, highlighting the contamination in the CCl_2^- spectrum. There is very good overlap between the pure $CDCl_2^-$ spectrum and the progression centered at 2.7 eV in the contaminated CCl_2^- spectrum. The contribution due to pure $CDCl_2^-$ is subtracted from the contaminated CCl_2^- spectrum in Figure 6.1b to produce the clean CCl_2^- photoelectron spectrum shown in Figure 6.1a. Some residual $CDCl_2^-$ contamination is seen as regular structure between 2.5 and 2.7 eV because of the slight difference in the peak widths of the two data sets.

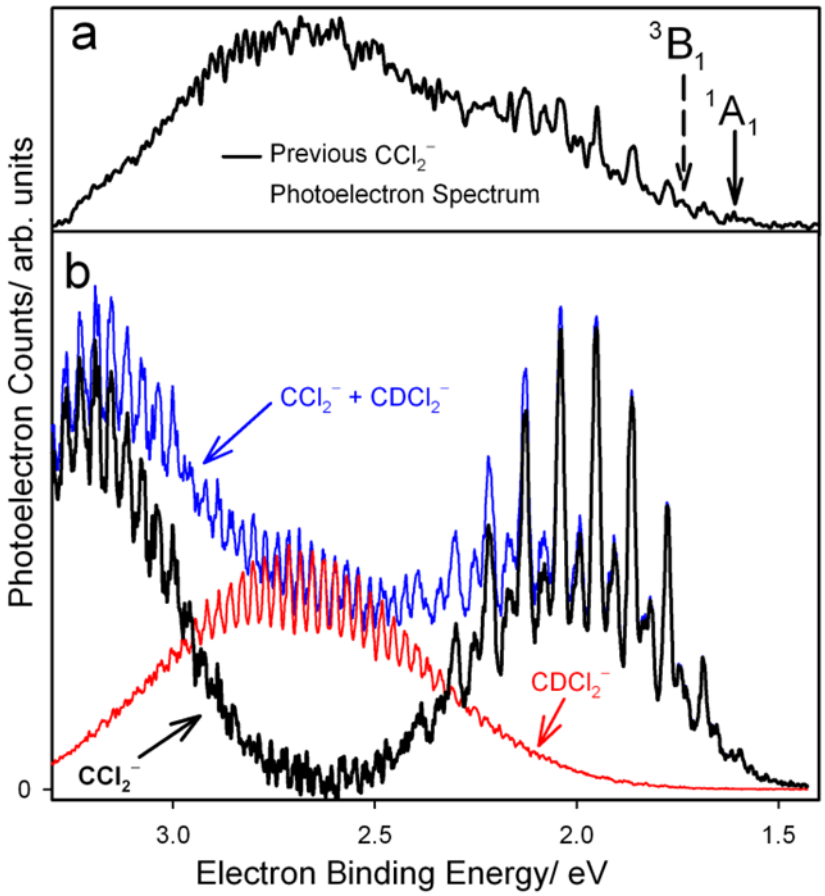

Figure 6.1 CCl_2^- magic angle photoelectron spectra. (a) The 364 nm CCl_2^- spectrum from the previous experimental study.[28] (b) The new 351 nm spectrum collected at *m/z* ~ 81 minimizes the $CDCl_2^-$ contamination. The pure $CDCl_2^-$ spectrum is scaled and subtracted from the *m/z* ~ 81 trace to yield the "clean" CCl_2^- spectrum.

Figure 6.2a depicts the clean CCl_2^- photoelectron spectrum from Figure 6.2b together with a 364 nm spectrum of CCl_2^- that have both been corrected for $CDCl_2^-$ contamination. The 364 nm cold spectrum of CCl_2^- was obtained while the source flow tube region was cooled with liquid nitrogen. Cooling the flow tube reduces the vibrational temperature of the ions and therefore reduces hot band contributions to the photoelectron spectrum. Figure 6.2b shows the simulated spectrum obtained using the PESCAL program. The intensity of the hot band transitions in the singlet state is consistent with a vibrational temperature of 350 K for CCl_2^-. The experimental

spectra are limited to an upper binding energy of 3.3 eV because slow electrons (eKE < ~0.3 eV) are not transmitted through the hemispherical energy analyzer. As a result, spectral features from electrons detached near threshold lose intensity. An instrument-related sharp drop-off and the erroneous appearance of a maximum in the Franck-Condon envelope appear at 3.2 eV, which represents a lower limit for the triplet state VDE. The CCSD(T)/aug-cc-pVTZ calculation gives a triplet VDE of 3.401 eV (Table 6.1), slightly beyond the usable range of our spectrometer.

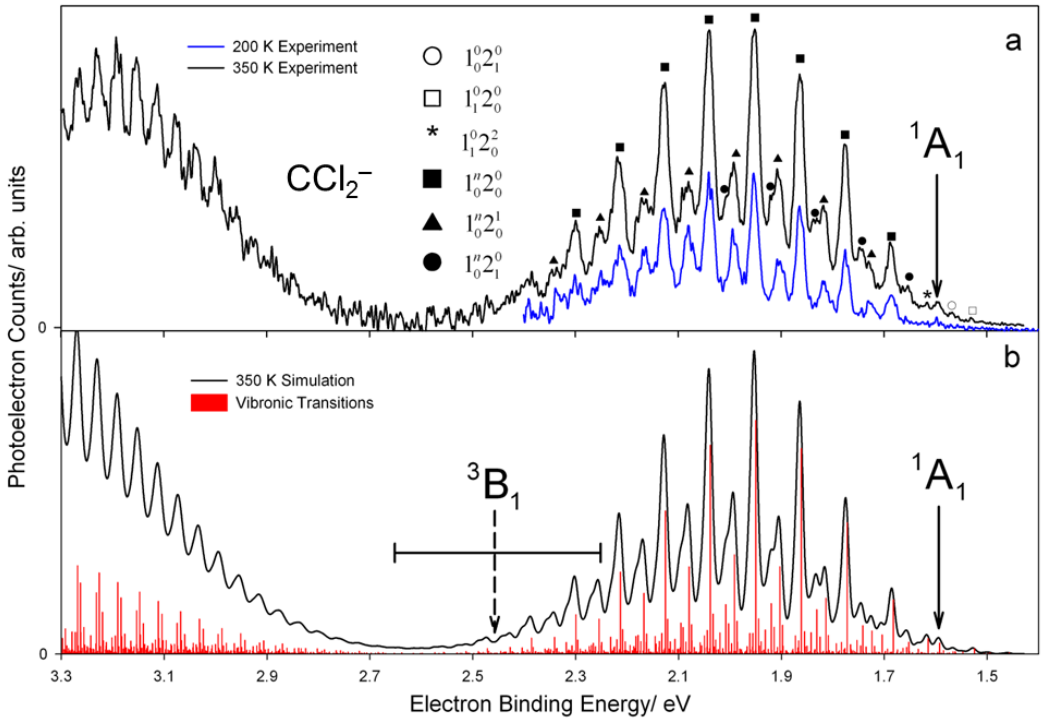

Figure 6.2 Analysis of the photoelectron spectrum of CCl_2^-. (a) The experimental magic angle spectrum was collected at room temperature (upper trace) and at ~200 K (lower trace). (b) Simulated photoelectron spectrum computed at 350 K. The singlet and triplet origins are marked with solid and dashed arrows, respectively. Sticks represent individual vibronic transitions.

The photoelectron spectrum of CCl_2^- in Figure 6.2a has improved energy resolution over the previous photoelectron experiments,[28] a result of several instrumental improvements and of

optimization of the ion-laser intersection position relative to the electron energy analyzer optics. Additionally, we now resolve features at higher electron binding energy because higher photon energy is available with 351 nm excitation and because $CDCl_2^-$ contamination has been subtracted. The origin peak of the singlet $X\ ^1A_1$ state is marked with a solid arrow and is seen in both the room temperature and cold spectra. Our experimental measurement for EA($X\ ^1A_1$ CCl_2) of 1.593(6) eV, which includes a rotational peak shift of -4 ± 1 meV, is in good agreement with previous experimental assignments and has improved accuracy.[28, 54] The cold spectrum shows a significant reduction in several peak intensities relative to the room temperature spectrum. This observation, along with measured progression peak spacing, enables the assignment of hot bands within the singlet manifold and further confirms the identity of the origin peak.

Table 6.1 Energies of origin transitions, vertical detachment energies, and singlet-triplet splittings (ΔE_{ST}) of dihalocarbenes (eV).

		$X\ ^1A_1 \leftarrow X\ ^2B_1$		$a\ ^3B_1 \leftarrow X\ ^2B_1$		
		(0-0)	VDE	(0-0)	VDE	ΔE_{ST}
CCl_2	*This work*	1.593(6)	2.00	2.47(20)	>3.2	0.9(2)
	Theoretical [a]	1.586	1.910	2.481	3.401	0.895
CBr_2	*This work*	1.78(10)	2.25	>1.9	--	--
	Theoretical [b]	1.834	2.400	2.579	3.719	0.745
CI_2	*This work*	< 3	--	--	--	--
	Theoretical [b]	2.095	2.537	2.500	3.535	0.39

[a] CCSD(T)/aug-cc-pVTZ.
[b] Single-point RCCSD(T)/ECP28MWB- and ECP46MDF-basis sets[31]

We observe three distinct vibrational progressions in the singlet state, which are identified in Figure 6.2a. The dominant progression arises from the symmetric stretch vibration. A series of doublet peaks lie between the symmetric stretch peaks; the lower eBE peaks arise

from combination bands involving the v_1 symmetric stretch combined with one quantum of the v_2 bending vibration, denoted $1_0^n 2_0^1$. The higher eBE component of each doublet arises from the hot band progression $1_0^n 2_1^0$. The two peaks with lower binding energy than the origin are hot bands involving the symmetric stretch and bending vibrations in the CCl_2^- anion. From these progressions, vibrational frequencies of the $X\ ^2B_1$ anion and neutral $X\ ^1A_1$ state are determined and reported in Table 6.1.

The simulation of the $X\ ^1A_1$ state of CCl_2 reproduces all of the resolved peaks in the experimental spectrum, which is explicitly shown in Figure 6.3. Furthermore, the peak positions and assignments agree quite well with the earlier and more precise dispersed fluorescence measurement of $X\ ^1A_1$ CCl_2 vibrational frequencies.[48] The extended progressions also enable an estimate of the anharmonicity of the symmetric stretch vibration, consistent with previous measurements.[48, 55] The simulation indicates that several transitions contribute to each peak in the singlet state, although the contributions are minor. For example, the bending vibration (v_2) is approximately half the frequency of the symmetric stretch vibration (v_1), which results in the $1_0^n 2_0^2$ progression contributing intensity to the symmetric stretch progression. Likewise, the $1_0^n 2_0^3$ progression adds a minor contribution to the intensity of the $1_0^n 2_0^1$ peaks. The fundamental bending vibration $1_0^0 2_0^1$ peak cannot be observed in our spectrum because of its low intensity and spectral congestion. These observations are consistent with previous high-level simulations of the CCl_2 photoelectron spectrum.

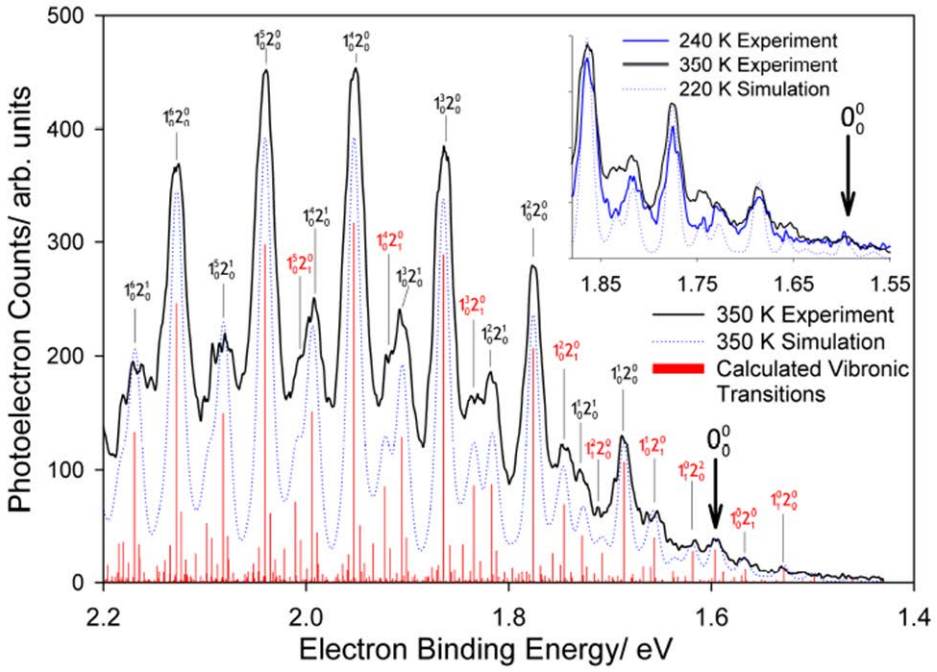

Figure 6.3 Expanded view of $X\ ^1A_1$ CCl_2^-. All the resolved features are identified based on peak position, progression spacing, and agreement with the simulated spectrum. The inset is an expanded view of the origin region comparing the cooled and room temperature photoelectron spectra. The peak labels in red designate hot bands, and the solid arrows indicate the origin for $X\ ^1A_1$ CCl_2.

We assign the broad spectral feature at higher binding energy to the $a\ ^3B_1$ excited state of CCl_2. The progression has an apparent onset at ~ 2.7 eV and has a Franck-Condon vibrational envelope that extends beyond the region accessible with our apparatus. The well-structured progression is very regular with peaks having a FWHM of 30 meV spaced by 300 cm^{-1}. The width is a factor of two greater than the instrument resolution, indicating that more than one transition lies beneath each of the triplet peaks. The extended progression also indicates that a large geometry change occurs in both the C-Cl bond length and the Cl-C-Cl bond angle when an electron is ejected from the $X\ ^2B_1$ state of the anion to produce the $a\ ^3B_1$ state of neutral CCl_2. Calculations confirm this observation (Table 6.2), with computed differences in C-Cl bond

length and Cl-C-Cl bond angle of the $X\ ^2B_1$ and $a\ ^3B_1$ states of 0.2 Å and 23°, respectively. Such large geometry changes make the interpretation of the photoelectron spectrum more challenging; this is investigated further in Section 6.5 for the dihalomethyl anion and corresponding radicals.[39, 56]

Table 6.2 Spectroscopic quantities and molecular constants of CCl_2.

		r /Å	θ /°	ν_1 /cm^{-1}	ν_2 /cm^{-1}	ν_3 /cm^{-1}
$\mathbf{CCl_2^-}$	*This work*	1.90(2) [a]	104(2) [a]	500(100)	200(100)	--
$\boldsymbol{X\ ^2B_1}$	*Experimental* [b]	1.92(2)	103(2)	--	--	--
	Theoretical [c]	1.892	103.75	547.6	243.3	463.3
$\mathbf{CCl_2}$	*This work*	--	--	737(6)	339(10)	--
$\boldsymbol{X\ ^1A_1}$	*Experimental*	1.714(1) [d]	109.3(1) [d]	731.14(22) [e]	335.79(11) [e]	745 [f]
	Theoretical [c]	1.729	109.02	728.7	333.7	758.1
$\boldsymbol{a\ ^3B_1}$	*This work*	1.69(10) [a]	127(10) [a]	~600 [g]	300(20) [g]	--
	Theoretical [c]	1.684	127.40	681.6	296.8	992.6

[a] Geometry changes are computed using Franck-Condon analysis. Absolute geometries are determined using as reference the experimental LIF geometrical parameters[18] of $X\ ^1A_1$ CCl_2.
[b] Photoelectron spectroscopy[54]
[c] CCSD(T)/aug-cc-pVTZ (this work)
[d] LIF[18]
[e] Dispersed fluorescence[48]
[f] Excitation matrix[14]
[g] Value obtained from peak separations at high vibrational quantum numbers (10-12) and simulations of extent of progressions based on calculated geometries. See text.

The triplet origin cannot be identified in the spectrum for several reasons. First, the large geometry change between $X\ ^2B_1$ CCl_2^- and $a\ ^3B_1$ CCl_2 results in a very small Franck-Condon overlap between the ground vibrational levels of the nuclear wavefunctions of the anion and the $a\ ^3B_1$ state of the neutral. The calculated CCSD(T) origin peak position for the $a\ ^3B_1$ state is 2.475 eV eBE, indicated by a dashed arrow in Figure 6.2b. The calculated VDE of the triplet state is 3.401 eV, which is not accessible with our laser photon energy. The intensity at the VDE

is calculated by Franck-Condon factors to be approximately 10^5 times higher than that at the origin. Based upon this estimate, the intensity of the triplet origin is too weak to be observed with our apparatus, even if there were no other obscuring features. Additionally, the expected triplet origin occurs at electron binding energies corresponding to the greatest interference from the $CHCl_2^-$ contaminant. Furthermore, the high energy end of the $X\ ^1A_1$ state progression overlaps the low energy end of the triplet spectrum. These factors effectively render the triplet origin unobservable.

Consequently, we must use only the shape and intensity of the $a\ ^3B_1$ photoelectron spectrum to obtain an estimate of the binding energy of the triplet origin; this origin then gives our best estimate of the singlet-triplet splitting. We simulate the $a\ ^3B_1$ photoelectron spectrum using a range of origin values centered around the calculated 2.475 eV value. Simulations with origins above 2.7 and below 2.3 eV do not reproduce the experimental features and spectral shape without large changes in the calculated optimized geometries of the $X\ ^2B_1$ and $a\ ^3B_1$ states. Therefore, from the agreement of the simulated spectrum with the experimental results and using the EA determined for the $X\ ^1A_1$ state, we estimate ΔE_{ST} = 0.9(2) eV for CCl_2. This value is consistent with singlet-triplet splitting obtained in recent theoretical studies.[31, 35, 57]

Further detailed analysis of the triplet state progression provides an experimental challenge. The observed peak widths of the resolved $a\ ^3B_1$ state features indicate that each peak contains contributions from several vibrational transitions. Despite this fact, the separation between the resolved transitions is remarkably uniform at 302(11) cm^{-1}, a value that is consistent with the calculated frequency of the bending vibration of 296 cm^{-1} and that is also approximately half the calculated (690 cm^{-1}) symmetric stretch frequency. Dyke *et al.* calculate substantial anharmonicity in this mode, quite possibly leading to an apparent near 2:1 ratio of these

frequencies at the higher vibrational levels that are observed in the triplet progressions.[35] Therefore, we might well expect the resultant vibrational progression to appear as a single progression with contributions from both the bending and symmetric stretching vibrations of *a* $^3B_1$ CCl_2.

Our simulations, as well as those carried out earlier by Dyke et. al,[35] clearly show a single progression of peaks containing contributions from both the bending and symmetric stretching vibrations of *a* $^3B_1$ CCl_2. The transitions result from overlapping combination bands of the bending vibrational progression built upon successive quanta of the symmetric stretch vibration. Using our simulated spectrum and corresponding vibronic transitions, we determine the vibrational frequencies for the symmetric stretch (~600 cm^{-1}) and bending vibrations (~300 cm^{-1}), listed in Table 6.2.

6.4.2 CBr_2^-

We report the 364 nm photoelectron spectrum of CBr_2^- obtained through the reaction of CH_2Br_2 with O^-. As with CCl_2^-, both CBr_2^- and $CHBr_2^-$ are formed in the reaction of CH_2Br_2 with O^- and are not separable with the Wien filter. Thus, we selectively synthesize $CHBr_2^-$ by reacting CH_2Br_2 with OH^- and then subtract the $CHBr_2^-$ contribution to the contaminated spectrum. The photoelectron spectrum at *m/z* 172, taken with horizontal polarization and containing both CBr_2^- and $CHBr_2^-$, is compared to the magic-angle spectrum of pure $CHBr_2^-$ in Figure 6.4a The spectrum of $CHBr_2^-$ is highly structured, indicating that the signal at high eBE in the contaminated spectrum is due to $CHBr_2^-$. This correspondence of well-defined peaks enables subtraction of the contaminant from the spectrum. The $CHBr_2^-$ spectrum is scaled to the contaminated CBr_2^- spectrum, assuming that the difference between the two spectra must remain

positive and that all of the intensity in the high eBE peaks is due to $CHBr_2^-$. The clean photoelectron spectrum of CBr_2^-, mostly free of contamination from $CHBr_2^-$, is also shown in Figure 6.4a. After subtraction, we observe one main progression centered at 2.3 eV that we assign to $X\ ^1A_1$ CBr_2. Combined with the improved spectral resolution and increased signal-to-noise in this study, the subtraction of $CHBr_2^-$ yields a CBr_2^- spectrum with substantial improvement over the previous photoelectron spectrum of CBr_2^- (Figure 6.4b).[28]

The $X\ ^1A_1$ state of CBr_2 displays an extended vibrational progression due to the very large difference in $\angle$ (Br-C-Br) bond angel between the anion and the singlet neutral, indicated in Table 6.3. This change in geometry also results in poor Franck-Condon overlap between the ground vibrational levels of $X\ ^2B_1$ CBr_2^- and $X\ ^1A_1$ CBr_2, and thus we are unable to observe the singlet origin peak in the photoelectron spectrum.

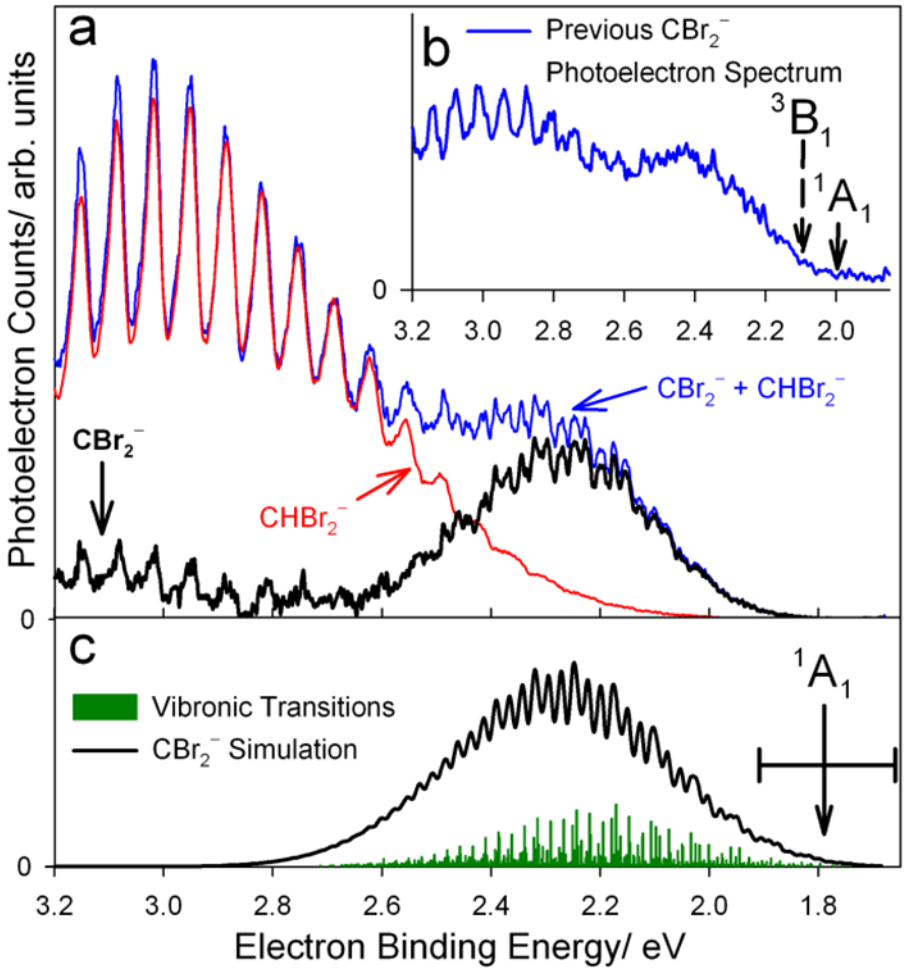

Figure 6.4 CBr_2^- magic angle photoelectron spectra: A comparison of (a) the new 364 nm spectrum with (b) the previously published 364 nm spectrum.[28] The new photoelectron spectrum is collected at *m/z* ~ 172 and contains both CBr_2 and $CHBr_2$. The pure $CHBr_2^-$ spectrum is clearly responsible for the progression attributed to the triplet state of CBr_2 in the previous spectrum. Subtraction of the $CHBr_2^-$ contribution from the *m/z* ~ 172 spectrum yields the corrected CBr_2^- spectrum. (c) Franck-Condon simulation of the singlet state of CBr_2, computed at 350 K. Sticks represent individual vibronic transitions. Solid arrows in (b) and (c) mark the singlet origin in the previous and current studies, respectively, as determined by Franck-Condon analysis. The dashed arrow in (b) marks the incorrect triplet origin assignment of the previous dihalocarbene study.[28]

Franck-Condon simulations are employed to aid in the interpretation of the singlet state spectrum (Figure 6.4c). Frequencies and anharmonicities of the singlet state were obtained from a recent single vibronic level (SVL) emission study by Reid and co-workers,[49] while parameters for the

anion were calculated using B3LYP/6-311++G** (Table 6.3).[58] The convolution (black trace) of the individual vibronic transitions (green sticks) reproduces the experimental photoelectron spectrum with EA($X\ ^1A_1\ CBr_2$) = 1.75(15) eV. The geometry change between the anion and the neutral are determined from these simulations. Using as a reference the geometry of the singlet neutral that was determined by the LIF excitation spectrum[17] combined with *ab initio* calculations,[59] we determine the geometry of $X\ ^2B_1\ CBr_2^-$ (Table 6.3): the C-Br bond length is 2.09(2) Å, with a BrCBr bond angle of 105(4)º.

Table 6.3 Spectroscopic quantities and molecular constants of CBr_2.

		r /Å	θ /º	ν_1 /cm^{-1}	ν_2 /cm^{-1}	ν_3 /cm^{-1}
$\mathbf{CBr_2^-}$	*This work*	2.09(2) [b]	105(4) [b]	--	--	--
$\boldsymbol{X\ ^2B_1}$	*Theoretical* [a]	2.100	106.36	455.8	129.7	365.8
$\mathbf{CBr_2}$	*This work*	--	--	600(50)	200(50)	--
$\boldsymbol{X\ ^1A_1}$	*Experimental*	1.865 [c]	110.7 [c]	606.6(4) [d]	199.5 [d]	679.8(7) [d]
	Theoretical [e]	1.898	110.0	601.6	196.6	655.3
$\boldsymbol{a\ ^3B_1}$	*This work*	--	--	--	--	--
	Theoretical [e]	1.839	129.5	533.6	185.4	878.7

[a] B3LYP/6-311++G** (this work)
[b] Geometry changes are computed using Franck-Condon analysis. Absolute geometries are determined using as reference the experimental LIF geometrical parameters[17] of $CBr_2\ X\ ^1A_1$.
[c] Combined LIF[17] and Theory[59]
[d] Single Vibronic Level Emission[49]
[e] CCSD(T)/cc-pVTZ[31]

Franck-Condon simulations reveal that the progression arising from $X\ ^1A_1$ of CBr_2 results from overlapping combination bands of the bend built upon successive quanta of the symmetric stretch vibration. The simulated stick spectrum is in good agreement with the peak positions of the $X\ ^1A_1$ manifold observed by SVL emission.[49] The frequency of the symmetric stretch vibration is approximately three times that of the bend, so the spacing between peaks in

the photoelectron spectrum roughly corresponds to the frequency of the bending vibration. Analysis of the spectral peak positions supports a bending frequency of approximately 200 cm^{-1}, with an uncertainty on the order of the peak width (100 cm^{-1}).

It is unclear whether we have any evidence of the triplet state of CBr_2 in the photoelectron spectrum. Upon subtraction of the $CHBr_2^-$ photoelectron spectrum from the contaminated CBr_2^- spectrum, some residual intensity remains at binding energies greater than 2.6 eV (Figure 6.4a). Because the fractional $CHBr_2^-$ contribution in this region is large and because all of the maxima in the subtracted spectrum occur at very nearly the same energy as $CHBr_2^-$ contaminant peaks, we must consider this residual intensity above 2.6 eV EBE to be an artifact of the subtraction. Unfortunately, unlike the CCl_2^- spectrum in which the $CHCl_2^-$ peak appears in the valley between the singlet and triplet states of CCl_2, the $CHBr_2^-$ contamination—and thus the residual intensity—occurs in the region we expect to see the triplet. Dyke and co-workers predict the $a\ ^3B_1$ origin to be 2.579 eV with a VDE of 3.719 eV (Table 6.1).[31] Franck-Condon simulations, shown in Figure 6.5, of the $a\ ^3B_1$ CBr_2 spectrum using molecular constants calculated by Dyke *et al.*[31] reproduce the peak spacing of the residual features; however, this peak spacing is also the same (within 15 cm^{-1}) as that of the contaminant $CHBr_2^-$. Thus, the fact that the contaminant ion completely overlaps the region in which we expect to see the triplet, along with the similarity in $CHBr_2$ and the predicted $a\ ^3B_1$ CBr_2 vibrational progressions, conspire to prevent a definitive assignment of the residual peaks. It is clear, however, that the previous $a\ ^3B_1$ origin assignment was incorrect, and the ΔE_{ST} of CBr_2 is greater than previously reported.[28]

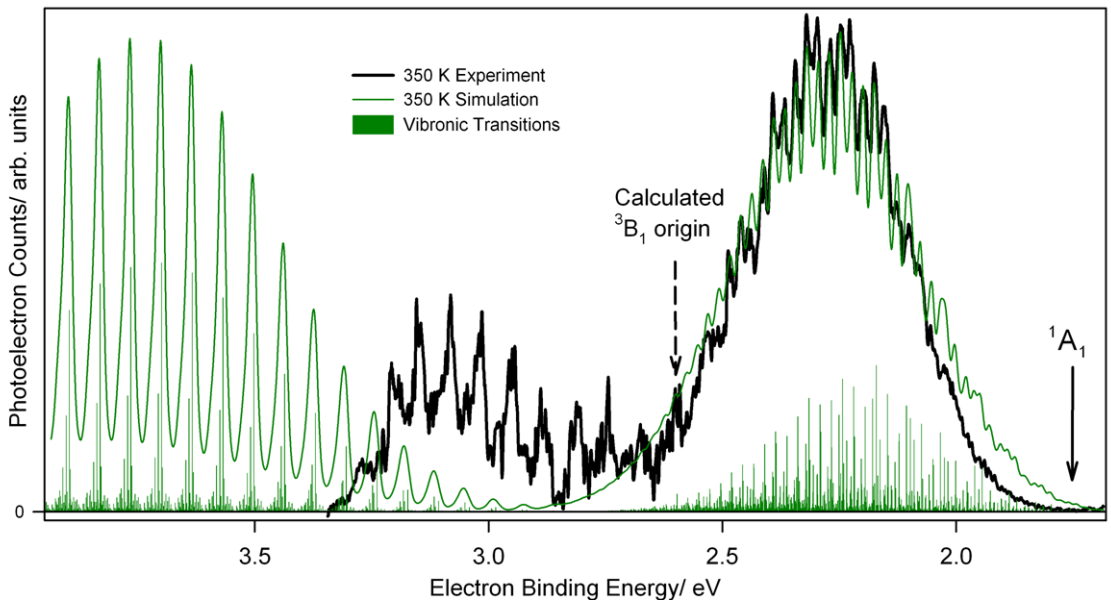

Figure 6.5 Comparison of the best fit simulation and the corrected CBr_2^- spectrum, showing both the *a* $^3B_1$ and *X* $^1A_1$ states of CBr_2 in the simulation. The *a* $^3B_1$ state is simulated using the electron affinity and vibrational frequencies calculated by Dyke *et al.*[31] The Franck-Condon factors for both the singlet and triplet states are calculated in the Morse oscillator, parallel mode approximation using numerically integrated Laguerre polynomial wavefunctions.

6.4.3 CI_2^-

Finally, we report the 364 nm photoelectron spectrum of CI_2^- obtained through the reaction of CH_2I_2 with O^-. As with the other halocarbenes, a pure CHI_2^- spectrum is measured, appropriately scaled, and then subtracted from the contaminated spectrum to obtain a clean CI_2^- spectrum. Unlike the other carbenes, we observe a two photon process with the continuous-wave excitation laser, involving 364 nm photodissociation of CI_2^- to form CI + I^-, followed by a second photon detaching an electron from I^-. The resulting narrow peak at eBE = 3.06 eV coincides with the known electron affinity of I (EA = 3.059 eV[60]) and confirms the two-photon source of this feature. The presence of the I^- peak indicates that the IC – I^- dissociation energy is substantially less than the photon energy, 3.406 eV. This I^- two-photon feature was not observed

in the previous photoelectron spectrum[28] (Figure 6.6b), presumably because the laser power in the previous work—a factor of four lower than that used in the present study—was insufficient to make this two-photon process significant. Similar two-photon processes have been observed in anion photoelectron spectroscopy of O_3^-, Ni_3^-, and Au_3^-.[50, 61, 62] We speculate that 364 nm radiation might produce CX – X^- photodissociation in CCl_2^- and CBr_2^-, as well. However, we are unable to observe Cl^- or Br^- photodissociation products because the electron affinity of Cl (EA = 3.613 eV[63]) exceeds the laser photon energy, and 351 nm photodetachment of Br^- (EA(Br) = 3.364 eV[64]) produces electrons with kinetic energy that is too low to be transmitted through the hemispherical electron analyzer.

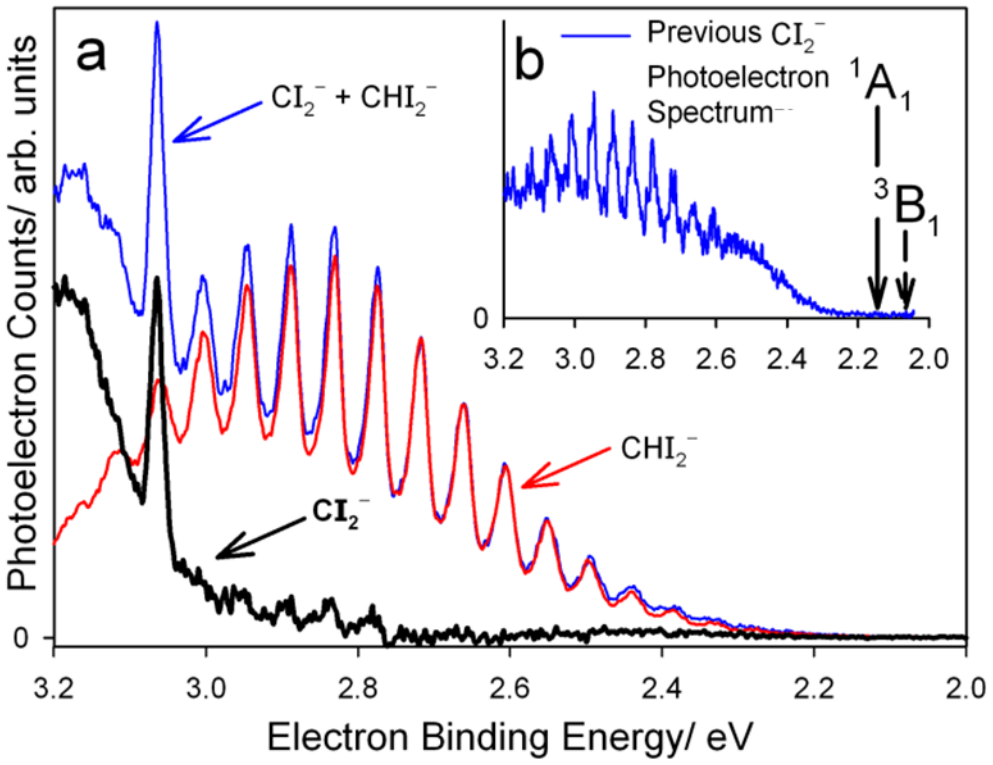

Figure 6.6 CI_2^- 364 nm photoelectron spectra: A comparison of (a) the new magic angle spectrum and (b) the previously published spectrum.[28] The previous singlet and triplet origin assignments are marked with solid and dashed arrows, respectively, in (b). The photoelectron spectrum collected at *m/z* ~ 266 contains both CI_2 and CHI_2. The pure CHI_2^- spectrum is clearly responsible for the progression attributed to the triplet state of CI_2 in the previous spectrum.[28] Subtraction of the CHI_2^- contribution from the *m/z* ~ 266 spectrum yields the corrected CI_2^- spectrum.

The photoelectron spectrum is dominated by CHI_2^-, which has a broad spectral band spanning approximately 1 eV. As seen in Figure 6.6a, there is some residual structure left after the subtraction of CHI_2^- features at binding energies below 3 eV. As with CBr_2^-, the residual peaks mimic the CHI_2^- spectrum. The remaining broad, structureless feature is attributed to CI_2^-, but the lack of resolved features and limited electron energy range preclude any further assignment. Calculations performed by Dyke *et al.* predict the electron affinity of CI_2 to be 2.1 eV and the *a* $^3B_1$ origin to be 2.5 eV with a VDE of 3.5 eV.[31] After the subtraction of the CHI_2

progression, we find no significant photoelectron signal below 3.0 eV, and can only claim that $EA(CI_2) < 3$ eV. It is clear that the previous origin assignments[28] for the CI_2 singlet and triplet states were actually components of the CHI_2^- photoelectron spectrum, and the assignments were incorrect

6.5 Results and Discussion: Dihalomethyl Anions (CHX_2^-)

One of the key reasons why the contamination of the dihalocarbene photoelectron spectra went undetected for nearly ten years was the lack of any experimental photoelectron spectra of the dihalomethyl anions. Though the CHX_2^- spectra are shown in the previous sections, these were mainly used to subtract their contribution from the spectra of the CX_2^- anions. This section focuses on what we can experimentally learn about the dihalomethyl anions and corresponding radicals.

Even though the dihalomethyl anions and radicals contain only four atoms, analysis of the experimental spectra is very challenging due to the large geometry change between the anion and neutral. We have dedicated a considerable amount of effort analyzing and modeling the dihalomethyl spectra in an attempt to extract the spectroscopic information one hopes to obtain using photoelectron spectroscopy.[39] Furthermore, we investigate how the normal mode analysis that is generally used to model photoelectron spectra is inadequate for molecular systems where there is significant mode-coupling present, as well when there is a large geometry change between the anion and neutral. Thus, a more sophisticated methodology is required to model and simulate the photoelectron spectra, which accounts for mode coupling and the anharmonic nature of the anion and neutral potential energy surfaces.

The photoelectron spectra of the three dihalomethyl anions ($CHCl_2^-$, $CHBr_2^-$, CHI_2^-) and their deuterated analogs are shown in Figure 6.7. The spectra exhibit extended, partially

resolved vibrational progressions that arise from the large geometry change that takes place when an electron is detached from the pyramidal anion, producing an essentially planar neutral radical. This large geometry change and the broad vibrational progression are analogous to the triplet state of CCl_2, which also has an extended vibrational progression with no measurable intensity at the origin. From the Franck-Condon simulations (shown for $CDCl_2^-$ in Figure 6.10), the origin transition is calculated to have approximately 10^{-5} the intensity of the peak at the VDE. Thus, the origin will not be experimentally observable. Even though the origin cannot be directly measured, the observed VDE of each dihalomethyl radical can be readily determined from the spectra in Figure 6.7. These measured VDE's are in good agreement with the calculated values.[65] Furthermore, the calculated EAs are consistent with previous experimental EA determinations of $CHCl_2$ and $CHBr_2$ (Table 6.4).[66] This provides us with confidence that electronic structure calculations can be used to accurately describe the electronic energies of these species.

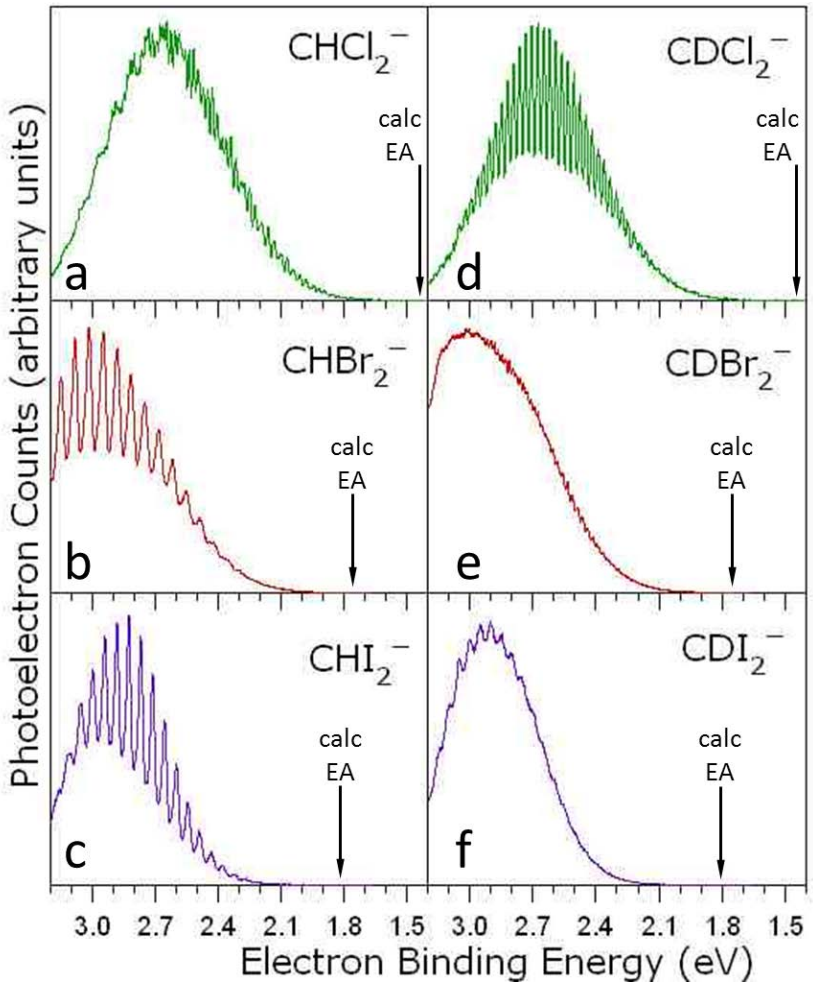

Figure 6.7 Experimental photoelectron spectra of the dihalomethyl anions (a) $CHCl_2^-$, (b) $CHBr_2^-$, (c) CHI_2^-, (d) $CDCl_2^-$, (e) $CDBr_2^-$, and (f) CDI_2^-. The calculated (B3LYP/6-311++G(d,p)) adiabatic electron affinity (EA) for each dihalomethyl radical is marked with a labeled arrow.

The calculated VDEs, computed by subtracting the energy of the anion from the energy of the neutral at the equilibrium geometry of the anion, agree reasonably well with the measured VDEs of the dihalomethyl anions, as shown in Table 6.4 The calculation of the difference in energy between the VDE and the EA should be fairly accurate for the rigid dihalomethyl anions. Therefore, an estimate for the EA can be obtained using the following equation:

Equation 6.1

$$EA_{est} = VDE_{exp} - [VDE_{calc} - EA_{calc}]$$

where

Equation 6.2

$$VDE_{calc} = E(\text{neutral at anion eqm geometry}) - E(\text{anion at anion eqm geometry})$$

and

Equation 6.3

$$EA_{calc} = E(\text{neutral at neutral eqm geometry}) - E(\text{anion at anion eqm geometry})$$

The results of the EA estimates using Equation 6.1 are summarized in Table 6.4. Our estimates are consistent with the previous EA determinations of $CHCl_2$ and $CHBr_2$.[66] The simulations and calculations for the photoelectron spectra presented in Figure 6.10 employ the EA estimates for the $CHCl_2$ and $CDCl_2$ radicals, listed in Table 6.4

Table 6.4 The experimental and calculated [CCSD(T)/aug-cc-pVDZ for $CHCl_2$($CDCl_2$) and B3LYP/6-311++G(d,p) for $CHBr_2$($CDBr_2$) and CHI_2(CDI_2)] electron affinity (EA) and vertical detachment energy (VDE) for each of the dihalomethyl radicals. Basis sets and pseudopotentials for Br and I were developed by Stoll et al.[67, 68]

		$CHCl_2$	**$CDCl_2$**	**$CHBr_2$**	**$CDBr_2$**	**CHI_2**	**CDI_2**
EA/ eV	*Experiment*	1.3(2)[a]	1.3(2)[a]	1.9(2)[a]	1.9(2)[a]	1.9(2)[a]	1.9(2)[a]
		1.47(4)[b]		1.71(8)[b]			
	Calculation	1.430	1.433	1.744	1.747	1.820	1.826
VDE/ eV	*Experiment*	2.6487	2.6815	3.0181	3.0171	2.8287	2.9057
	Calculation	2.8621	2.8630	2.8829	2.8836	2.8271	2.8271

[a] Estimates of EA were obtained by subtracting the calculated difference in energy between the VDE and the EA ($VDE_{calc} - EA_{calc}$) from the experimentally measured VDE using Equation 6.1.

[b] Experiment, Fourier transform ion cyclotron resonance mass spectrometry[66]

One of the most striking features of the spectra in Figure 6.7 is the observed regular peak spacing and the dramatic affect that deuteration has on the structure of the vibrational progression. There are several indications that the structure in the spectra does not result from a single vibrational progression and instead arises from multiple active vibrational modes with several vibronic transitions lying under each peak. First, the spacing between the peaks in the spectrum of $CDCl_2^-$ (230 cm^{-1}) does not correspond to the calculated frequency of any of the symmetric vibrational modes. Out of the 6 vibrational modes in $CDCl_2^-$, only 4 are totally symmetric, with the lowest frequency mode (the HCCl symmetric stretch) calculated to be ~ 300 cm^{-1}. Second, isotopic substitution has an unexpected effect on the spectrum of $CHCl_2^-$. The spectrum generally becomes more congested upon deuteration, as seen in the spectra of $CHBr_2^-$ and, to a lesser extent, of CHI_2^-. However, the spectrum of $CDCl_2^-$ has more resolved structure than that of $CHCl_2^-$, implying that the observed structure is due to accidental resonance among two or more vibrational modes, rather than to a single vibrational progression. Also, the peak widths near the VDE are at least 20 meV, significantly greater than our experimental resolution of about 12 meV; this is particularly true for $CHCl_2^-$ and $CDCl_2^-$ where the cooled ions should have minimal broadening from hot band transitions. Furthermore, the modulation depth of the peaks and the peak spacings change across the progression, a result of anharmonicity causing the vibronic transitions to move into and out of resonance.

Although the spectra show that multiple active vibrational modes give rise to the observed structure, the similarity of the $CHBr_2^-$ and CHI_2^- spectra suggests that the out-of-plane bend is active, and that the spacing of the peaks roughly corresponds to the frequency of this motion in the neutral species. In $CHBr_2$ the average peak spacing is 520(30) cm^{-1}, and in CHI_2 it is 440(40) cm^{-1} near the VDE.

To carry our analysis further, we turn to theory to model the photoelectron spectra and, hopefully, identify the origins of the observed vibrational structure experimentally. However, because a large geometry change takes place when an electron is removed from a dihalomethyl anion to generate the floppy radical, the independent normal-mode treatment (which typically works well for photoelectron spectra with modest geometry changes) fails for the dihalomethyl anions. A strong indicator why the independent normal-mode treatment is inappropriate for the CHX_2 species is shown in Figure 6.8 and Figure 6.9. Figure 6.8 plots the potential energy curves for the out-of-plane torsion angle ($\tau_{ClCHCl'}$) for both the anion and the neutral. Based on the calculated geometry difference between the anion and the neutral, we predict that vibrational mode involving this out-of-plane distortion will contribute significantly to the photoelectron spectrum. It is apparent that approximating this mode as a harmonic oscillator is unsuitable. Figure 6.9 depicts how the internal coordinates ($\theta_{HCCl,}$ r_{CH}, and r_{CCl}) in $CHCl_2$ vary as a function of $\tau_{ClCHCl'}$. The values for both θ_{HCCl} and r_{CCl} strongly depend on $\tau_{ClCHCl'}$, while r_{CH} remains essentially unchanged as $\tau_{ClCHCl'}$ is varied. Therefore, these three normal coordinates ($\theta_{HCCl,}$ $\tau_{ClCHCl'}$, and r_{CCl}) are not independent of each other, which demonstrating mode coupling. Accounting for this coupling is essential to simulate accurately the photoelectron spectra, as will be shown below.

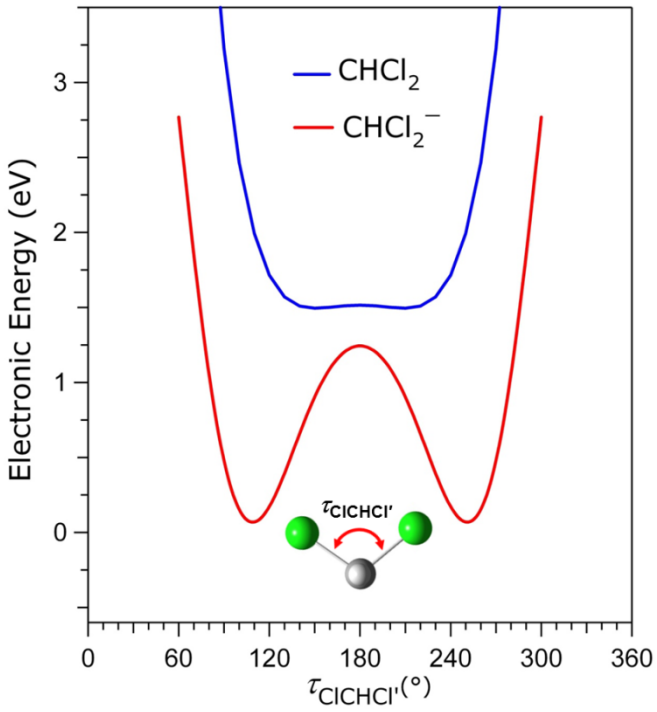

Figure 6.8 $CHCl_2$ (blue) and $CHCl_2^-$ (red) potential energy curves as a function of the out-of-plane angle ($\tau_{ClCHCl'}$). The inversion barrier for $CHCl_2$ is calculated to be only 162 cm^{-1}.

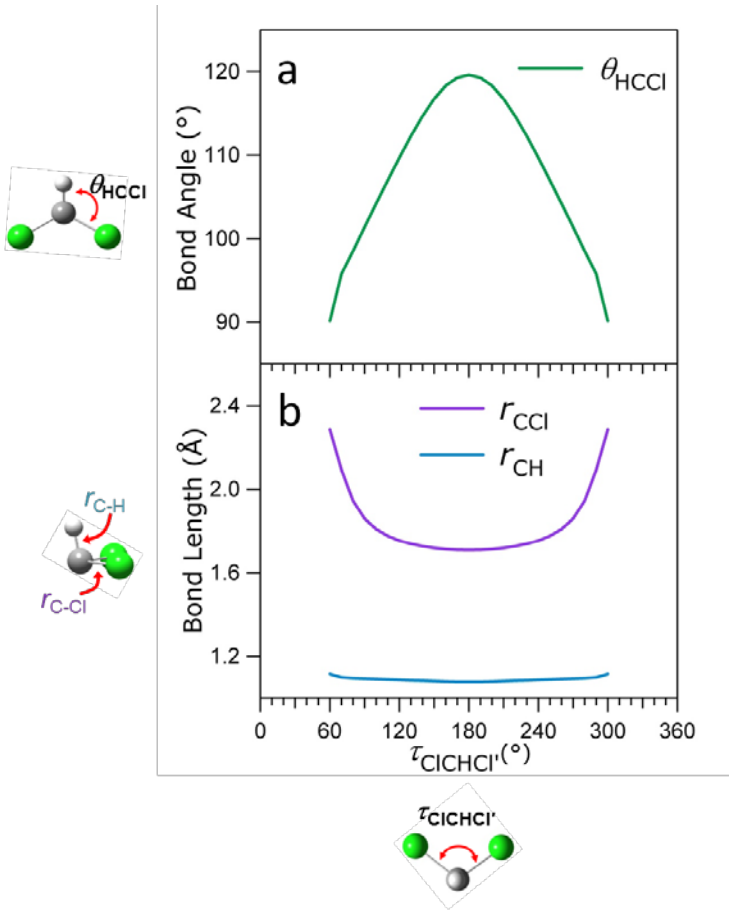

Figure 6.9 Change in the $CHCl_2$ internal coordinates θ_{HCCl} (green) (a), r_{CCl} (purple) and r_{CH} (blue), (b), as the out-of-plane angle $\tau_{ClCHCl'}$ is varied. Plots indicates the dependence of both the θ_{HCCl} angle and the C–Cl bond length (r_{CCl}) on the out-of-plane angle ($\tau_{ClCHCl'}$)

It is now instructive to compare how three different methods of modeling the photoelectron spectrum of $CDCl_2^-$ compare with what we measure experimentally. The three method attempted include progressively more sophisticated and system-specific treatments of the vibrational modes. Figure 6.10 compares the agreement of the experimental photoelectron spectrum of $CDCl_2^-$ with the three different simulation methods. The top panel (Figure 6.10a) is a Franck-Condon simulation using normal mode analysis in Cartesian coordinates. Because the

normal mode method for modeling photoelectron spectra has proven so powerful in the past and works well for the dihalocarbenes,[38, 69, 70] we first employ a Franck-Condon analysis using normal modes based in Cartesian coordinates to interpret the photoelectron spectra of the dihalomethyl anions. This method completely fails to reproduce the spectral envelope of the observed $CDCl_2^-$ spectrum. The simulations for the other dihalomethyl anions suffer from the same broad progressions shown in Figure 6.10a.

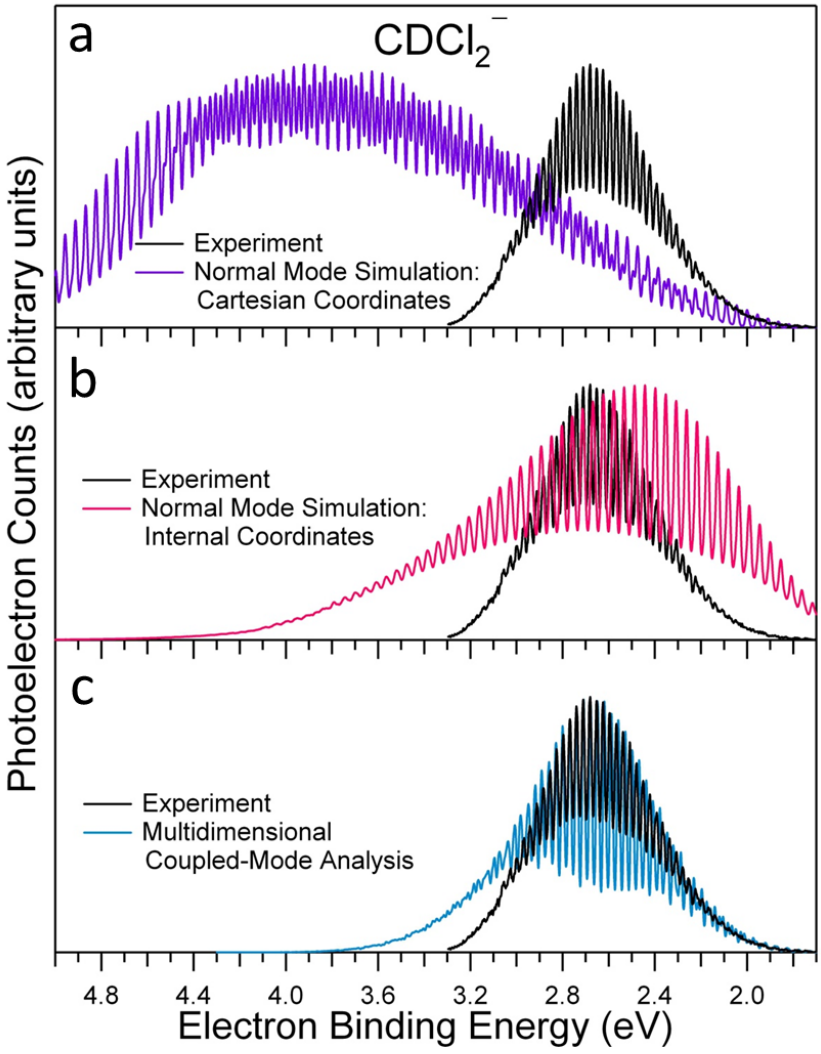

Figure 6.10 Comparison between theory and experiment for $CDCl_2^-$. (a) The photoelectron spectrum of $CDCl_2^-$ (150 K) and its simulation using normal mode analysis in Cartesian coordinates, which fails to reproduce the width of the spectral envelope. (b) Improvement in the agreement between experiment and the normal mode simulation is achieved by using an internal coordinate representation. (c) The width of the calculated spectral envelope is further reduced by using (2 + 1) – dimensional anharmonic coupled-mode analysis. All $CDCl_2^-$ calculated and simulated spectra were calculated at 150 K and were shifted to match the experimental EA of 1.3 eV.

After examining the Franck-Condon simulation and the corresponding Franck-Condon factors, the disparity in the width of the spectral envelope is due to strong false activity of the CH (CD) stretch vibrational mode. Based on our calculations, the CH stretch should have limited

activity as there is a very small change in the C–H bond length from $CDCl_2^-$ to neutral $CDCl_2$. It appears that the only manner in which the rectilinear Cartesian coordinates can reproduce the large geometry change is by erroneous displacement in the CH stretch normal mode coordinate, in combination with other modes. This type of mode mixing has been observed previously with other molecules undergoing large geometry changes upon photodetachement (including *c*-C_4F_8 in this thesis) .[71-75] In particular, a large geometry displacement in one Cartesian coordinate is partially projected (or mixed) onto the other coordinates, resulting in the appearance of vibrational progressions in the computed spectrum that are not experimentally observed.

In order to better represent the vibrational displacement between the anion and the neutral in the CHX_2 system, we next simulate the photoelectron spectrum based on a normal mode analysis using internal displacement coordinates (bond lengths and angles). Internal coordinates more naturally represent the vibrational potential energy surfaces and are less prone to induce artificial mixing between modes. The simulation using internal coordinates is shown in Figure 6.10b. The calculated spectral width has been substantially reduced compared to the simulation using Cartesian coordinates. However, the spectral envelopes from the simulation using internal coordinates still inadequately model the experimental spectrum. A lingering issue is that the large difference in the equilibrium geometries and bonding between the anion and the neutral cause the normal modes of the neutral to be characteristically different than those of the anion. When we express the normal modes of the neutral in terms of the harmonic normal mode vibrations of the anion, the orthogonality of the neutral normal modes is lost causing mode mixing. Additionally, this method still fails to address the issue of mode coupling which we know is present in the dihalomethyl systems from Figure 6.9.

In order to properly address the issues of anharmonicity of the vibrational potentials and coupling between vibrational modes in one electronic state, we take a multidimensional anharmonic coupled-mode approach.[39] The plots in Figure 6.8 and Figure 6.9 help to determine which vibrational modes needed to be included in the coupled-mode analysis ($\theta_{HCCl,}$ $\tau_{ClCHCl'}$, and r_{CCl}) and which modes are have negligible contribution experimental photoelectron spectrum (r_{CH}). Therefore, we explicitly couple the two bend modes (θ_{HCCl} and $\tau_{ClCHCl'}$) and convolute the resulting spectrum with the spectrum obtained from a one-dimensional treatment of the ClCCl stretch for an overall (2 + 1)-dimensional coupled mode analysis. Figure 6.10c compares the results of the coupled-mode analysis with the experimental spectrum for $CDCl_2^-$. The improvement between the calculated photoelectron spectrum and experimental observations is quite improved compared to the Franck-Condon simulations using either Cartesian or internal coordinate systems. The vibrational structure (peak spacing and intensity) is reproduced, as is the spectral width.

6.6 Conclusion

We have carried out studies of the photoelectron spectra of a series of dihalocarbene anions CX_2^- and the corresponding dihalomethyl anions CHX_2^-, where X= Cl, Br, or I. The present results provide a definitive explanation for the incorrect conclusions drawn in the earlier publication from our group: there was an undetected dihalomethyl anion contamination in the CX_2^- ion beams.[28] In all three dihalocarbene systems, significant contamination from the related dihalomethyl radical is present and must be subtracted. A contribution from dihalomethyl radicals was present but not identified in previous photoelectron studies, which resulted in the incorrect assignment of the triplet features in all three dihalocarbene systems.

We clearly observe both the $X\ ^1A_1$ and the $a\ ^3B_1$ electronic states of the CCl_2 carbene in our current photoelectron spectra. All major peaks in the singlet state are assigned and are consistent with previous experimental spectroscopic parameters for neutral CCl_2. The electron affinity of $X\ ^1A_1$ CCl_2 is 1.593(6) eV. The triplet state of CCl_2 is more complicated, and it is difficult to extract any parameters because of the large changes in geometry between the $X\ ^2B_1$ state of the anion and the $a\ ^3B_1$ state of the neutral. However, simulations of the resolved vibrational spectra at large vibrational quantum numbers yield $a\ ^3B_1$ CCl_2 symmetric stretch and bending frequencies of ~600 cm^{-1} and ~300 cm^{-1}, respectively. Based on our experimental observations and simulations, we estimate ΔE_{ST} to be 0.9(2) eV, consistent with recent high-level theoretical calculations. The photoelectron spectra of CBr_2^- and CI_2^- are much more difficult to interpret quantitatively due to the large overlap of the CHX_2^- photoelectron spectrum with that of the singlet and triplet states of the carbene radicals. This contamination, as well as the large geometry differences between the anion and the neutral dihalocarbenes, hinder accurate photoelectron spectroscopic determinations of the ΔE_{ST} values for these heavier dihalocarbenes.

The present studies unequivocally resolve the discrepancy between our earlier CCl_2 singlet-triplet splitting measurements[28] and numerous subsequent calculations,[31, 35, 57, 76] showing that the previously reported CCl_2, CBr_2 and CI_2 singlet-triplet splittings and EA(CI_2) were in error.

Finally, the photoelectron spectra of the dihalomethyl anions are investigated to reveal the difficulties in our typical normal mode analysis due to the large geometry change between CHX_2^- and CHX_2. The pyramidal dihalomethyl anions become nearly planar upon photodetachment, resulting in photoelectron spectra that display extended vibrational progressions with negligible intensity at the origin transition. The absence of experimentally

observable origins in the spectra and the inability to accurately reproduce the spectral envelopes preclude the direct determination of EAs or vibrational frequencies of the dihalomethyl anions in this study. While normal mode analysis accurately simulates the spectra of molecules that experience small displacements of equilibrium nuclear configurations upon photodetachment, false activity of the CH stretch is predicted in the dihalomethyl radicals when a Cartesian displacement coordinate system is employed. Therefore, more sophisticated analysis is required which accounts for mode coupling and the anharmonic nature of the anion and neutral potential energy surfaces. This work illustrates that we cannot treat the vibrational normal modes in the CHX_2 class of molecules as separable, nor can we compute the Franck-Condon factors as a product of harmonic oscillators.

6.7 References

1. Kirmse, W., *Carbene Chemistry*1971, New York: Academic Press.

2. Moss, R.A. and M. Jones, eds. *Carbenes*. ed. R.A. Moss and M. Jones. Vol. 2. 1975, Wiley: New York.

3. Moss, R.A. and M. Jones, eds. *Reactive Intermediates*. 1978, Wiley: New York.

4. Borden, W.T., ed. *Diradicals*. 1982, Wiley: New York.

5. Carl Lineberger, W. and W. Thatcher Borden, *The synergy between qualitative theory, quantitative calculations, and direct experiments in understanding, calculating, and measuring the energy differences between the lowest singlet and triplet states of organic diradicals.* Physical Chemistry Chemical Physics, 2011. **13**(25): p. 11792-11813.

6. Andrews, L., *Infrared Spectrum of Dichlorocarbene in Solid Argon.* J. Chem. Phys., 1968. **48**(3): p. 979.

7. Clouthier, D.J. and J. Karolczak, *Pyrolysis Jet Spectroscopy - Rotationally Resolved Electronic-Spectrum of Dichlorocarbene.* J. Phys. Chem., 1989. **93**(22): p. 7542-7544.

8. Tevault, D.E. and L. Andrews, *Laser-Induced Fluorescence-Spectrum of Argon Matrix-Isolated Dichlorocarbene.* J. Mol. Spec., 1975. **54**(1): p. 110-120.

9. Bondybey, V.E. and J.H. English, *Laser Excitation-Spectra and Lifetimes of CBrCl and CBr_2 in Solid Ar.* J. Mol. Spec., 1980. **79**(2): p. 416-423.

10. Choe, J.I., S.R. Tanner, and M.D. Harmony, *Laser-Excitation Spectrum and Structure of CCl_2 in a Free-Jet Expansion from a Heated Nozzle.* J. Mol. Spec., 1989. **138**(2): p. 319-331.

11. Fujitake, M. and E. Hirota, *The Millimeter-Wave and Submillimeter-Wave Spectrum of Dichlorocarbene CCl_2 - Electronic-Structure Estimated from the Nuclear-Quadrupole Coupling-Constants.* J. Chem. Phys., 1989. **91**(6): p. 3426-3430.

12. Xu, S.L. and M.D. Harmony, *Halocarbene Production in Free-Jet Expansions from a Hot Nozzle.* Chem. Phys. Lett., 1993. **205**(6): p. 502-507.

13. Ivey, R.C., et al., *Electron-Diffraction Study of Structure of Dibromomethylene Radical.* J. Chem. Phys., 1974. **60**(8): p. 3174-3177.

14. Bondybey, V.E., *Emission and Excitation-Spectra of CCl_2 in Solid Argon.* J. Mol. Spec., 1977. **64**(2): p. 180-183.

15. Zhou, S.K., et al., *Gas-Phase Spectrum of Dibromocarbene Studied by Laser-Induced Fluorescence.* Chem. Phys. Lett., 1990. **166**(5-6): p. 547-550.

16. Schlachta, R., et al., *Laser-Induced Fluorescence Excitation Spectrum of Supersonically Cooled Bromochlorocarbene in the Gas-Phase.* J. Phys. Chem., 1991. **95**(19): p. 7132-7134.

17. Xu, S.L. and M.D. Harmony, *LIF Excitation Spectrum of Dibromocarbene in a Supersonic Free-Jet Expansion.* J. Phys. Chem., 1993. **97**(29): p. 7465-7470.

18. Clouthier, D.J. and J. Karolczak, *A Pyrolysis Jet Spectroscopic Study of the Rotationally Resolved Electronic-Spectrum of Dichlorocarbene.* J. Chem. Phys., 1991. **94**(1): p. 1-10.

19. Carter, E.A. and W.A. Goddard, *Relation between Singlet Triplet Gaps and Bond-Energies.* J. Phys. Chem., 1986. **90**(6): p. 998-1001.

20. Carter, E.A. and W.A. Goddard, *New Predictions for Singlet Triplet Gaps of Substituted Carbenes.* J. Phys. Chem., 1987. **91**(18): p. 4651-4652.

21. Carter, E.A. and W.A. Goddard, *Correlation-Consistent Singlet Triplet Gaps in Substituted Carbenes.* J. Chem. Phys., 1988. **88**(3): p. 1752-1763.

22. Gutsev, G.L. and T. Ziegler, *Theoretical-Study on Neutral and Anionic Halocarbynes and Halocarbenes.* J. Phys. Chem., 1991. **95**(19): p. 7220-7228.

23. Russo, N., E. Sicilia, and M. Toscano, *Geometries, Singlet-Triplet Separations, Dipole-Moments, Ionization-Potentials, and Vibrational Frequencies in Methylene (CH_2) and Halocarbenes (CHF, CF_2, CCl_2, CBr_2, and CI_2).* J. Chem. Phys., 1992. **97**(7): p. 5031-5036.

24. Garcia, V.M., et al., *Singlet-triplet energy gap in halogen-substituted carbenes and silylenes: A difference-dedicated configuration interaction calculation.* Mol. Phys., 1996. **87**(6): p. 1395-1404.

25. Gobbi, A. and G. Frenking, *The Singlet-Triplet Gap of the Halonitrenium Ions NHX^+, NX_2^+ and the Halocarbenes CHX, CX_2 (X=F, Cl, Br, I).* J. Chem. Soc.-Chem. Communications, 1993(14): p. 1162-1164.

26. Wenthold, P.G. and W.C. Lineberger, *Negative ion photoelectron spectroscopy studies of organic reactive intermediates.* Accts. Chem. Research, 1999. **32**(7): p. 597-604.

27. Zittel, P.F., et al., *Laser photoelectron spectrometry of CH_2^-- Singlet-triplet splitting and electron-affinity of CH_2.* Journal of the American Chemical Society, 1976. **98**(12): p. 3731-3732.

28. Schwartz, R.L., et al., *Singlet-triplet splittings in CX_2 (X = F, Cl, Br, I) dihalocarbenes via negative ion photoelectron spectroscopy.* J. Phys. Chem. A, 1999. **103**(41): p. 8213-8221.

29. Chau, F.T., et al., *The singlet-triplet separation in CF_2: State-of-the-art ab initio calculations and Franck-Condon simulations including anharmonicity.* ChemPhysChem, 2005. **6**(10): p. 2037-2045.

30. Sendt, K. and G.B. Bacskay, *Spectroscopic constants of the (X)over-tilde((1)A(1)), (a)over-tilde(B-3(1)), and (A)over-tilde(B-1(1)) states of CF_2, CCl_2, and CBr_2 and heats of formation of selected halocarbenes: An ab initio quantum chemical study.* J. Chem. Phys., 2000. **112**(5): p. 2227-2238.

31. Lee, E.P.F., J.M. Dyke, and T.G. Wright, *The lowest singlet-triplet gap in CCl_2, CBr_2 and CI_2.* Chem. Phys. Lett., 2000. **326**(1-2): p. 143-150.

32. Drake, S.A., J.M. Standard, and R.W. Quandt, *An ab initio investigation of the ground and excited electronic state properties of a series of bromine- and iodine-containing singlet carbenes.* J. Phys. Chem. A, 2002. **106**(7): p. 1357-1364.

33. McKee, M.L. and J. Michl, *A possible reinterpretation of the photoelectron spectra of CCl_2, CBr_2, and CI_2: A role for quartet isodihalocarbene or dihalocarbene radical anions?* J. Phys. Chem. A, 2002. **106**(37): p. 8495-8497.

34. Liang, J., et al., *Geometries of the Halocarbene anions HCF^- and CF_2^-: ab initio calculation and Franck-Condon analysis.* J. Mol. Structure-Theochem, 2004. **672**(1-3): p. 133-139.

35. Dyke, J.M., et al., *A combined ab initio/Franck-Condon study of the A-X single-vibronic-level emission spectrum of CCl_2 and the photodetachment spectrum of CCl.* ChemPhysChem, 2005. **6**(10): p. 2046-2059.

36. Tarczay, G., et al., *Accurate ab initio determination of spectroscopic and thermochemical properties of mono- and dichlorocarbenes.* Phys. Chem. Chem. Phys., 2005. **7**(15): p. 2881-2893.

37. Seal, P. and S. Chakrabarti, *Explicit role of dynamical and nondynamical electron correlation on singlet-triplet splitting in carbenes.* Chem. Phys., 2007. **332**(2-3): p. 232-242.

38. Wren, S.W., et al., *The photoelectron spectrum of CCl_2^-: the convergence of theory and experiment after a decade of debate.* Physical Chemistry Chemical Physics, 2009. **11**(23): p. 4745-4753.

39. Vogelhuber, K.M., et al., *Photoelectron spectra of dihalomethyl anions: Testing the limits of normal mode analysis.* The Journal of Chemical Physics, 2011. **134**(18): p. 184306-13.

40. Ervin, K.M. and W.C. Lineberger, in *Advances in Gas Phase Ion Chemistry*, N.G. Adams and L.M. Babcock, Editors. 1992, JAI: Greenwich. p. 121.

41. Frisch, M.J., et al., *Gaussian 03, Revision B.05*2003, Pittsburgh: Gaussian, Inc.

42. Pople, J.A., M. Headgordon, and K. Raghavachari, *Quadratic Configuration-Interaction - a General Technique for Determining Electron Correlation Energies.* Journal of Chemical Physics, 1987. **87**(10): p. 5968-5975.

43. Dunning, T.H., *Gaussian-basis sets for use in correlated molecular calculations. 1. The atoms boron through neon and hydrogen.* Journal of Chemical Physics, 1989. **90**(2): p. 1007-1023.

44. Woon, D.E. and T.H. Dunning, *Gaussian-Basis Sets for Use in Correlated Molecular Calculations .3. the Atoms Aluminum through Argon.* Journal of Chemical Physics, 1993. **98**(2): p. 1358-1371.

45. Becke, A.D., *Density-functional thermochemistry. III. The role of exact exchange.* Journal of Chemical Physics, 1993. **98**(7): p. 5648-5652.

46. Lee, C.T., W.T. Yang, and R.G. Parr, *Development of the colle-salvetti correlation-energy formula into a functional of the electron density.* Physical Review B, 1988. **37**(2): p. 785-789.

47. Ervin, K.M., *PESCAL, Fortran program*, 2008.

48. Liu, M.L., et al., *Dispersed fluorescence spectra of the CCl2 (A)over-tilde-(X)over-tilde vibronic bands.* Phys. Chem. Chem. Phys., 2003. **5**(7): p. 1352-1358.

49. Tao, C., C. Mukarakate, and S.A. Reid, *Single vibronic level emission spectroscopy of the (A)over-tilde(1)A ''-> X(1)A ' system of bromochlorocarbene.* J. Mol. Spec., 2007. **246**(2): p. 113-117.

50. Ho, J., K.M. Ervin, and W.C. Lineberger, *Photoelectron-Spectroscopy of Metal Cluster Anions - Cu_n^-, Ag_n^-, and Au_n^-.* Journal of Chemical Physics, 1990. **93**(10): p. 6987-7002.

51. Chen, P., ed. *Unimolecular and Bimolecular Ion-Molecule Reaction Dynamics*. ed. C.-Y. Ng, T. Baer, and I. Powis1994, Wiley & Sons Chichester. 371.

52. Ervin, K.M., et al., *Naphthyl radical: Negative ion photoelectron spectroscopy, Franck-Condon simulation, and thermochemistry.* J. Phys. Chem. A, 2001. **105**(48): p. 10822.

53. Lee, J. and J.J. Grabowski, *Reactions of the Atomic Oxygen Radical Anion and the Synthesis of Organic Reactive Intermediates.* Chem. Rev., 1992. **92**(7): p. 1611.

54. Murray, K.K., et al., *Photoelectron-Spectroscopy of the Halocarbene Anions HCF^-, $HCCI^-$, $HCBr^-$, HCI^-, CF_2^-, and CCl_2^-.* J. Chem. Phys., 1988. **89**(9): p. 5442-5453.

55. Mukarakate, C., et al., *Probing spin-orbit mixing and the singlet-triplet gap in dichloromethylene via K-a-sorted emission spectra.* Phys. Chem. Chem. Phys., 2006. **8**(37): p. 4320-4326.

56. Bopp, J.C., et al., *Spectroscopic characterization of the isolated SF_6^- and $C_4F_8^-$ anions: Observation of very long harmonic progressions in symmetric deformation modes upon photodetachment.* Journal of Physical Chemistry A, 2007. **111**(7): p. 1214-1221.

57. Barden, C.J. and H.F. Schaefer, *The singlet-triplet separation in dichlorocarbene: A surprising difference between theory and experiment.* J. Chem. Phys., 2000. **112**(15): p. 6515-6516.

58. Frisch, M.J., et al., *Gaussian 03, Revision B.01*2004, Wallingford, CT: Gaussian, Inc.

59. Bauschlicher, C.W., *Singlet-Triplet Separation in CBr_2.* J. Am. Chem. Soc., 1980. **102**(17): p. 5492-5493.

60. Hanstorp, D. and M. Gustafsson, *Determination of the Electron-Affinity of Iodine.* J. Phys. B, 1992. **25**(8): p. 1773-1783.

61. Novick, S.E., et al., *Laser Photoelectron, Photodetachment, and Photodestruction Spectra of O-3.* J. Chem. Phys., 1979. **70**(6): p. 2652-2662.

62. Ervin, K.M., J. Ho, and W.C. Lineberger, *Electronic and vibrational structure of transition metal trimers: photoelectron spectra of Ni_3^-, Pd_3^-, and Pt_3^-.* Journal of Chemical Physics, 1988. **89**(8): p. 4514-21.

63. Martin, J.D.D. and J.W. Hepburn, *Determination of bond dissociation energies by threshold ion-pair production spectroscopy: An improved D-0(HCl).* J. Chem. Phys., 1998. **109**: p. 8139.

64. Blondel, C., et al., *High Resolution Determination of the Electron Affinity of Fluorine and Bromine using Crossed Ion and Laser Beams.* Phys. Rev. A, 1989. **40**: p. 3698.

65. Li, Q.S., et al., *Electron affinities, molecular structures, and thermochemistry of the fluorine, chlorine and bromine substituted methyl radicals.* Mol. Phys., 2002. **100**(23): p. 3615.

66. Born, M., S. Ingemann, and N.M.M. Nibbering, *Thermochemical properties of halogen-substituted methanes, methyl radicals, and carbenes in the gas phase.* Int. J. Mass Spectrom., 2000. **194**(2-3): p. 103.

67. Stoll, H., B. Metz, and M. Dolg, *Relativistic energy-consistent pseudopotentials - Recent developments.* J. Comput. Chem., 2002. **23**(8): p. 767.

68. Thompson, M.A., et al., *A combined experimental/theoretical investigation of the near-infrared photodissociation of IBr-(CO2)(n).* J. Chem. Phys., 2008. **129**(22).

69. Ichino, T., et al., *Structure of the vinyldiazomethyl anion and energetic comparison to the cyclic isomers.* Journal of Physical Chemistry A, 2007. **111**(34): p. 8374-8383.

70. Vogelhuber, K.M., et al., *The C-H bond dissociation energy of furan: Photoelectron spectroscopy of the furanide anion.* Journal of Chemical Physics, 2011. **134**(6).

71. Borrelli, R. and A. Peluso, *The vibrational progressions of the N -> V electronic transition of ethylene: A test case for the computation of Franck-Condon factors of highly flexible photoexcited molecules.* J. Chem. Phys., 2006. **125**(19).

72. Borrelli, R. and A. Peluso, *The electron photodetachment spectrum of c-C_4F_8-: A test case for the computation of Franck-Condon factors of highly flexible molecules.* J. Chem. Phys., 2008. **128**(4).

73. Kikuchi, H., et al., *Computational method for calculating multidimensional Franck-Condon factors: Based on Sharp-Rosenstock's method.* J. Chem. Phys., 2003. **119**(2): p. 729.

74. Reimers, J.R., *A practical method for the use of curvilinear coordinates in calculations of normal-mode-projected displacements and Duschinsky rotation matrices for large molecules.* J. Chem. Phys., 2001. **115**(20): p. 9103.

75. Wilson, E.B., J.C. Decius, and P.C. Cross, *Molecular Vibrations*1980, New York: Dover.

76. Hajgato, B., et al., *Triplet-singlet energy gaps in iodo-carbenes (I-C-X): Remarkable discrepancy between theory and experiment.* Phys. Chem. Chem. Phys., 2000. **2**(22): p. 5041-5045.

7 Photoelectron Spectroscopy of SF_6^- and *c*-$C_4F_8^-$

7.1 Introduction

Both SF_6 and *c*-C_4F_8 have industrial applications in etching plasmas as well as insulating gasses for high voltages. In addition, both molecules have long lifetimes in the upper atmosphere and are considered greenhouse gasses.[1] These two perfluorinated molecules are of fundamental interest and share the unique propensity to non-dissociatively attach low energy electrons, indicating that the corresponding anions have a very long lifetime with respect to autodetachment.[2] One of the reasons for this slow autodetachment undoubtedly results from the change in structure of the molecular framework upon anion formation. For these reasons, both molecules have been the subject of many studies which have focused on the characterization of the neutral and the formation and reactivity of the anion[3-9]; however very few spectroscopic studies have addressed the structural aspects of the ions.

Of particular interest, SF_6 has been the focus of intense study for the past thirty years.[10-20] The neutral structure has been well characterized by several Raman and Infrared studies[21, 22], however only two reports address the structural aspects of the ion through spectroscopy.[23, 24] An early study commented only on the lack of observed photodetachment in the near ultraviolet[23], far above the adiabatic threshold, while a matrix isolation study identified a single weak vibrational transition near 600 cm^{-1}.[24]

Several theoretical studies have also have investigated the properties of SF_6 and SF_6^-. Computational results predict that the O_h symmetry of SF_6 is retained upon attachment of an electron; however the S–F bond lengths are elongated by about 0.2 Å.[25] The electron affinity of neutral SF_6 has been calculated by a variety of electronic structure methods ranging from modest

density functional to the more sophisticated coupled-cluster theories, resulting in a wide range of values.[20, 22, 26-29] The most reliable EA calculations use highly correlated methods (MP2, CCSD) and have converged on a generally accepted value of 0.9 eV.[22] Additionally, after publication of the work which this Chapter is based,[30] two groups have calculated the photoelectron spectrum of SF_6^-, in an attempt to reproduce the experimental results presented in this Chapter.[26, 28] The results of these calculations and their implications are discussed in some detail in the results section.

C-C_4F_8, like SF_6, is expected to have a large geometry change upon attachment of an electron. It is known from spectroscopic studies that the geometry of the neutral is bent (D_{2d} symmetry) with the majority of the 23 vibrational mode frequencies having been measured.[31-38] Recent high-level theoretical calculation (CCSD(T)/CBS) have mapped out the anharmonic double-well potential energy surface in the ring-puckering coordinate in *c*-C_4F_8; a 132 cm^{-1} barrier was determined for this low-frequency puckering motion. However, far less is known about the anion structure and vibrational frequencies. Recent ESR studies have shown that the anion is planar with D_{4h} symmetry[39] and computational results predict that the added electron is delocalized in a 'p-like' orbital extending over the entire molecule. This strengthens the four C–C bonds via π-bonding interactions, and weakening the eight C–F bonds by σ-antibonding interactions.[39, 40]

The present study investigates what happens when an electron is attached to a closed shell perfluorinated molecule, SF_6 and *c*-C_4F_8. Photoelectron spectroscopy is uniquely able to provide experimental insight into the structural changes between the anion and neutral species as well as possible determination of the adiabatic electron affinity. The photoelectron spectra of both *c*-$C_4F_8^-$ and , SF_6^- are measured and reported in this Chapter. This work was performed in

collaboration with Professor Mark A. Johnson at Yale University and Thomas M. Miller and A. A. Viggiano at Hanscom Air Force Research Laboratory. In addition to independently measuring the SF_6^- photoelectron spectrum, our collaborators at Yale University also recorded the argon-tagged photoelectron spectrum of SF_6^-, which limits the amount of internal energy available to the SF_6^-•Ar complex. The experimental findings are compared to recent theoretical calculated results, which provide additional insight into the structure of the energetics of both systems studied in this work.

7.2 Experimental Method

The photoelectron spectra for both *c*-$C_4F_8^-$ and SF_6^- anions used the negative ion photoelectron spectrometer described in Chapter 2. Negative ions are formed in a flowing afterglow ion source. Specifically, target anions were formed by seeding the helium buffer gas with trace amounts of either SF_6 or *c*-C_4F_8 gas prior to the microwave discharge. The photoelectron spectrum of SF_6^- was recorded with ions cooled to ~ 150 K using a liquid nitrogen jacket surrounding the flow tube. The mass resolution of the Wien velocity filter for these experiments was $m/\Delta m$ ~ 40. Typical mass-selected ion beam currents were ~ 500 pA. The ~ 0.5 W output from a single-mode continuous-wave argon ion laser operating at 351 nm (3.531 eV) is built up to approximately 50 W of circulating power in the interaction region. The energy resolution of the hemispherical analyzer is approximately 8 meV under the experimental conditions used here.

Calculated optimized geometries and unscaled harmonic vibrational frequencies for anions and corresponding neutral molecules are determined with density functional theory (B3LYP/6-31+G(3df)) using the Gaussian 03 program.[25]

7.3 Results and Discussion

7.3.1 Photoelectron Spectrum of *c*-$C_4F_8^-$

It is known from electron diffraction and infrared studies that neutral *c*-C_4F_8 in its ground state has a bent D_{2d} symmetry with the four carbon atoms forming a dihedral angle of ~ 17°.[31-38] However, ESR studies have shown that this dihedral angle in the anion is approximately 0° resulting in a planar ring with D_{4h} symmetry.[39] Figure 7.1 illustrates the geometries of the anion and neutral calculated using density functional theory, which illustrates this geometry change from the anion to the neutral. Detachment of an electron elongates the C–C bonds, shortens the C–F bonds, and increases the nonbonded F–F distance. This increase in symmetry has been predicted by computations that also show that the negative charge in the anion is a 'p-like' orbital that is delocalized over the entire molecule.[39, 40] Therefore, we would expect to observe a broad vibrational envelope in the photoelectron spectra due to the large geometry changes expected when an electron is removed from the anion.

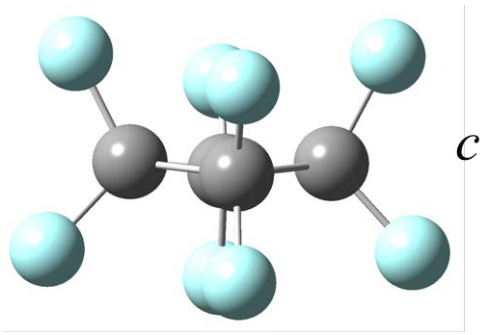

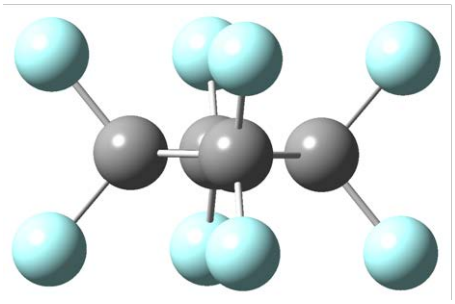

Figure 7.1 Calculated structures (B3LYP/6-31+G(3df)) of *c*-C_4F_8 neutral (top) and anion (bottom).

The 351 nm photoelectron spectrum of *c*-$C_4F_8^-$ is shown in Figure 7.2. As expected, a very broad vibrational progression is observed. What is very unusual is that the progression has over 50 resolved peaks that are spaced by 355(4) cm^{-1} and extend 2 eV into the vibrational manifold of the ground electronic state of *c*-C_4F_8. With this large geometry change, the Franck-Condon overlap between the lowest vibrational wavefunctions of the anion and the neutrals is essentially zero. This will result in the origin transition be unobservable, as was found in the photoelectron spectra of CHX_2^- (Chapter 6). With such an extended vibrational progression that has vanishing intensity at its onset, we cannot identify the origin peak or determine the electron affinity.

There have been several previous experimental studies which have reported EA values for *c*-C_4F_8. The arrow in Figure 7.2 corresponds to a flowing afterglow Langmuir probe study

which measured an EA(*c*-C_4F_8) of 0.63(5) eV, and is indicated with an arrow in Figure 7.2.[8] Two other EA values have been reported[18, 41], but as we will elaborate below, we believe the flowing afterglow determination to the most reliable measurement of EA(*c*-C_4F_8).

The vibrational structure in Figure 7.2 is both unexpected and challenging to interpret. On the basis of the size of the molecule and the large geometry change between the anion and neutral, one might expect to see an extended Franck-Condon profile with virtually no resolved features. However, what is so striking is that the spectrum is rather 'diatomic-like' and remains harmonic across the entire spectrum. As mentioned above, when the electron is photodetached from *c*-$C_4F_8^-$, the C–C bond elongate and the C–F bonds shorten. This change in geometry is mirrored in the totally symmetric ring-breathing ν_5 vibrational mode, calculated to be 370 cm^{-1} at the MP2/TZVPP level of theory (Table 7.1).[42] We expect this mode to be active and will likely contribute significantly to the photoelectron spectrum. Based only on the experimental observation of a regular peak spacing of 355 cm^{-1} in the vibrational progression, it is very tempting to attribute the vibration structure solely to the ν_5 mode. However, this simple explanation requires this ring-breathing mode to behave like a harmonic oscillator even at very high excitation energies of more than 2 eV. Additionally, excitation of more than fifty quanta of the ν_5 mode would require a large, physically unrealistic displacement from the equilibrium geometry. These issues motivated a deeper investigation into the origin of the vibrational structure observed in the *c*-$C_4F_8^-$ photoelectron spectrum.

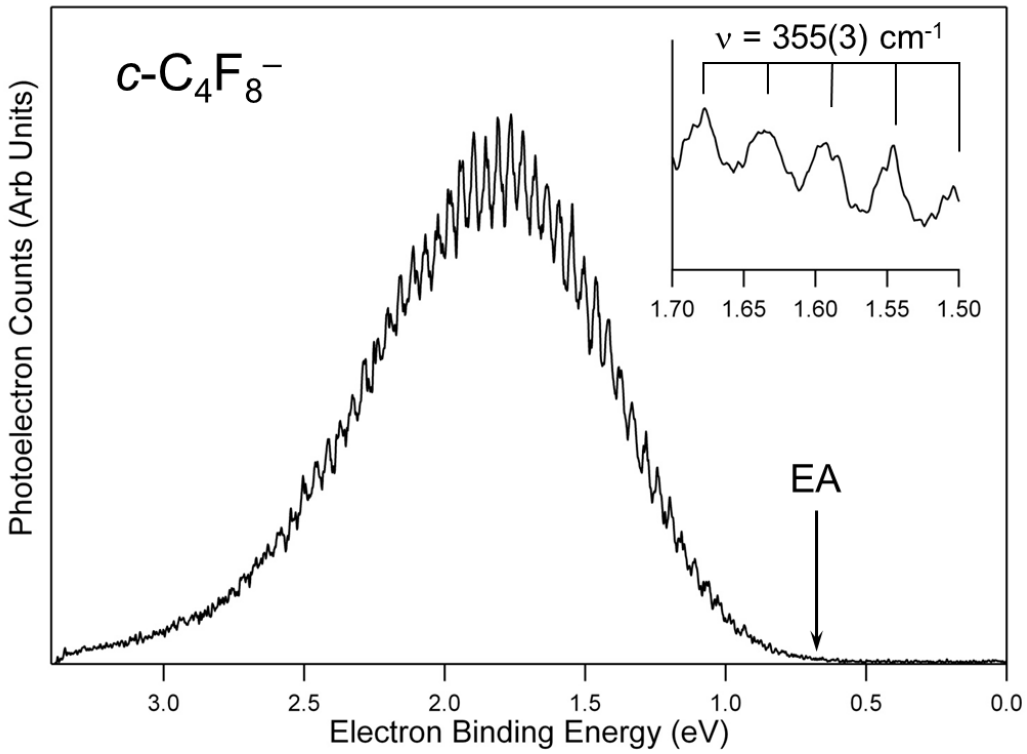

Figure 7.2 The 351 nm photoelectron spectrum of *c*-$C_4F_8^-$ taken at the magic angle using a flowing afterglow photoelectron spectrometer. A regular harmonic progression is present with spacing corresponding to a frequency of 355(3) cm^{-1}, shown in the inset. The EA determined by Miller et al. is depicted on the graph by a vertical arrow at 0.63 eV.[8]

After the photoelectron spectrum in Figure 7.2 was published[30], Borrelli and Peluso[42] performed a Franck-Condon analysis using curvilinear internal coordinate representation to model the photoelectron spectrum. Due to the large change of geometry between the anion and neutral, internal coordinates where used to represent the normal modes of the both the anion and the neutral. As was shown for CHX_2, using mass-weighted Cartesian coordinate representation for molecules undergoing large geometry changes upon photodetachment can lead to false activity in vibrational modes resulting in a much larger vibrational progression than observed experimentally. The low-frequency ring-puckering mode (ν_6), which is calculated to be very

anharmonic, was also treated independent of the other active modes when evaluating the overlap integrals in the Franck-Condon calculations.

Their calculations indicated that, when only ν_5 vibrational mode is active, the simulated photoelectron spectrum should exhibit a progression that spans less than 1 eV, much narrower than the measured spectrum. However, when an additional higher-frequency ring-breathing mode (ν_5) is included in the simulation, the resulting spectral profile qualitatively agrees with the experimental spectrum. This simulation, shown in Figure 7.3, has ~ 60 peaks that are spaced by approximately 370 cm^{-1}. It appears that the equally spaced peaks in the photoelectron spectrum are due to accidental resonances of several quasidegenerate transitions; namely $1_0^m 5_0^n$ and $1_0^{m-1} 5_0^{n+4}$ where m and n are integers. The underlying continuum, which is not replicated when only two modes are included in the simulation, is reproduced with the inclusion of the ring-puckering vibrational mode. Figure 7.3b shows the final simulation achieved when all modes were included in the calculation, which agrees very well with the experimental photoelectron spectrum.

Table 7.1 Theoretical normal mode frequencies (cm^{-1}), calculated at the MP2/TZVPP level of theory, for both *c*-C_4F_8 and *c*-$C_4F_8^-$ with the corresponding experimental values for *c*-C_4F_8.

Vibrational Mode	*c*-C_4F_8			*c*-$C_4F_8^-$	
	D_{2d}	Theory[42]	Expt.	D_{4h}	TheoryX [42]
ν_1	a_1	1448	1443[a]	a_{1g}	1499
ν_2	a_1	1315	1413[a]	b_{2u}	963
ν_3	a_1	715	700[a]	a_{1g}	668
ν_4	a_1	618	607[a]	a_{1g}	489
ν_5	a_1	370	359[a]	b_{2u}	391
ν_6	a_1	58		b_{2u}	47
ν_7	a_2	893		a_{2g}	889
ν_8	a_2	220		b_{1u}	216
ν_9	b_1	1047	1010[a]	b_{2g}	1203
ν_{10}	b_1	283		b_{2g}	253
ν_{11}	b_1	251		a_{1u}	206
ν_{12}	b_2	1323	1292[b]	a_{2u}	872
ν_{13}	b_2	1264	1240[b]	b_{1g}	1042
ν_{14}	b_2	669	659[b]	b_{1g}	631
ν_{15}	b_2	360	348[b]	b_{1g}	358
ν_{16}	b_2	197	195[b]	a_{2u}	190
ν_{17}	e	1380	1343[b]	e_g	1249
ν_{18}	e	1246	1223[b]	e_u	847
ν_{19}	e	987	964[b]	e_u	835
ν_{20}	e	581	569[b]	e_u	559
ν_{21}	e	444	437[b]	e_g	425
ν_{22}	e	289	283[b]	e_g	271
ν_{23}	e	190		e_u	200

[a] From Miller et al.[37] (Miller 1971)
[b] From Blake et al.[38] (Blake 2007)
[42] From Borrelli et al.

As previously mentioned, other EA values have been reported in the literature.[18, 41] Although the photoelectron spectrum of *c*-$C_4F_8^-$ does not give a direct determination of this value, it does allow for an upper bound of ~0.75 eV. We therefore can give a brief assessment of one reported value. Hiraoka and coworkers measured EA(*c*-C_4F_8) relative to that of SF_6, using a pulsed electron beam high-pressure mass spectrometer.[41] They reported a value of 1.05 eV, incompatible with the photoelectron spectrum reported in this Chapter. Hiraoka interpreted his

observations to suggest the presence of an excited $C_4F_8^-$ isomer, which would form at elevated temperatures (above 350 K) and undergo electron detachment. The EA of this other isomer was reported to be 0.5 eV, based upon electron-transfer equilibrium with O_2. The coexistence of a second anionic isomer is not supported by the photoelectron angular distribution measurements, which give a smooth progression of the anisotropy parameter, β, across the spectrum. Furthermore, the Franck-Condon calculations effectively reproduce the experimental spectrum by considering only one $C_4F_8^-$ isomer. While our results do not provide a definitive EA determination, they do indicate which prior measurements are most reliable. Thus we conclude that the EA value of 0.63 eV[8] is both consistent with our data, and the most reliable value available. A detailed discussion of all the earlier EA determinations for C_4F_8 has recently been reported by Miller et al.[8]

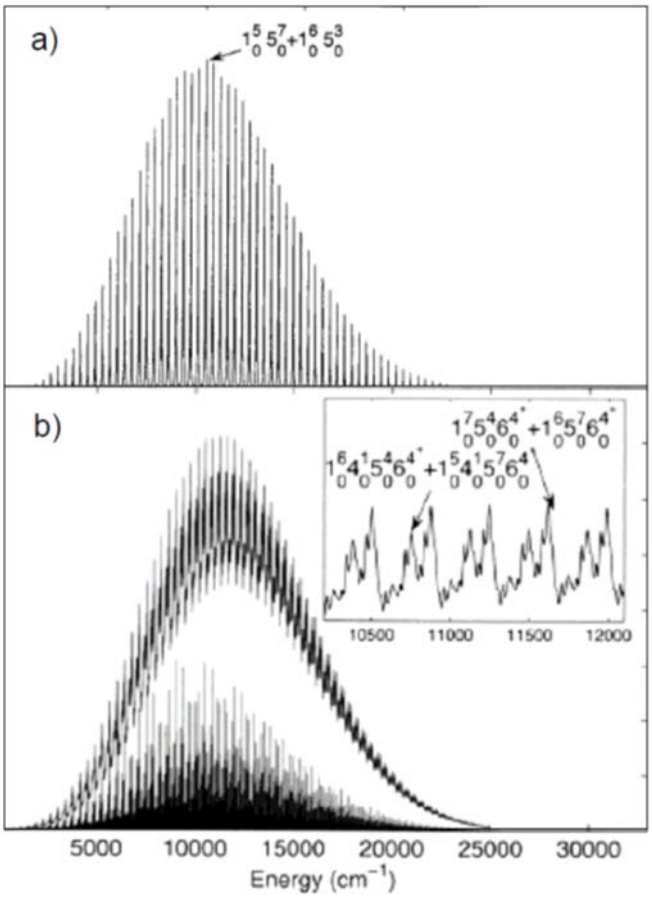

Figure 7.3 Calculated photoelectron spectrum of *c*-$C_4F_8^-$ reproduced from Borrelli et al.[42] Only two modes are included in the simulations (ν_1 and ν_5) in a) while all modes were included in the simulation in b). The Franck-Condon factors are convoluted with a 25 cm^{-1} Gaussian.

7.3.2 Photoelectron Spectrum of SF_6^-

Similar challenges encountered with *c*-C_4F_8 are present in SF_6 where a large geometry change occurs between the anion and the neutral. The photoelectron spectrum of SF_6 is shown in Figure 7.4. The most striking aspect of this spectrum is that, in spite of the fact that the EA is reported to lie in the 1 eV range,[43] significant photoelectron intensity does not begin until almost 2 eV. The vertical detachment energy (band maximum) at 3 eV is qualitatively consistent with

previous CCSD calculations. The global minimum for the SF_6^- anion is calculated to have considerably elongated S–F bonds (~ 0.2 Å), but retain the O_h symmetry of the neutral molecule.[22] The photoelectron spectrum contains two regular vibrational progressions, highlighted in the inset of Figure 7.4, which are labeled with solid and dashed lines.

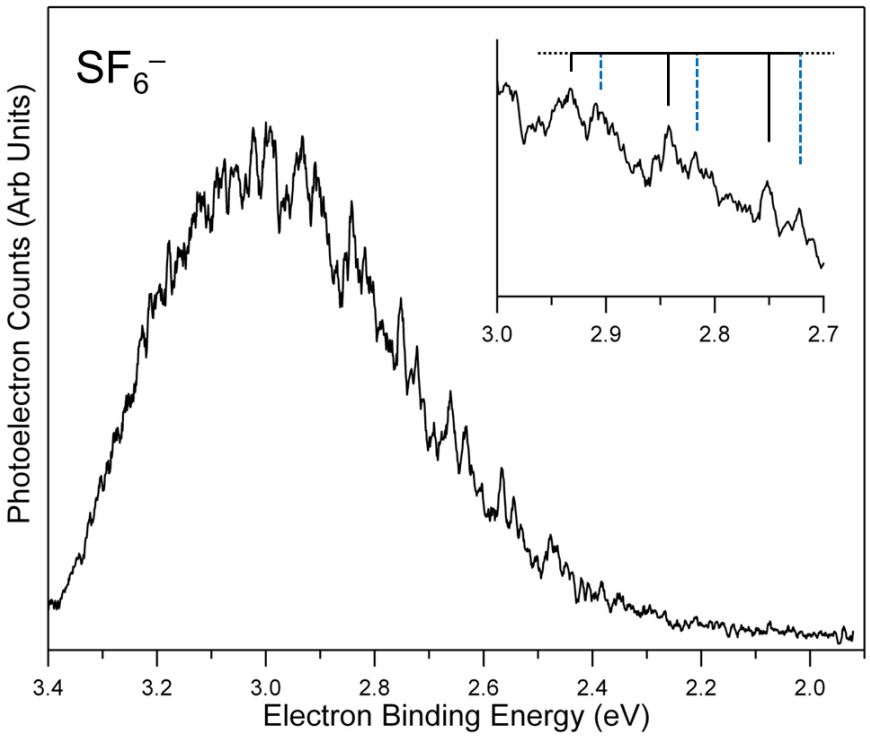

Figure 7.4 The magic angle 351 nm photoelectron spectrum of SF_6^- measured using ions cooled to ~ 150 K. The inset highlights the regular peak spacing corresponding to a vibrational frequency of 750(20) cm^{-1} (black line) in the neutral. An additional set of interloping peaks is also present (dashed blue lines) which has the same characteristic spacing but is offset from the main progression by 440(10) cm^{-1}.

In an effort to better understand the origin of the vibrational progression in the photoelectron spectrum, SF_6^- was produced using a pulsed source and the photoelectron

spectrum was measured using a double focusing tandem time-of-flight pulsed spectrometer at Yale University.[44] This spectrum, shown in Figure 7.5, is compared with the photoelectron spectrum from Figure 7.4. The spectrum in trace b was obtained using the Yale instrument, where SF_6^- was generated by entraining trace amounts of SF_6 in an expansion of N_2 at a stagnation pressure of 5 atm. The spectra both show the same discernible vibrational fine structure with similar depths of modulation and location of the band maxima, thus reflecting a robust property of the anion that is independent of the method of preparation. To further limit the internal energy of the SF_6^- anion, photoelectron spectra of SF_6^-•Ar was measured and is plotted in trace a of Figure 7.4. The spectrum of SF_6^-•Ar has noticeably sharper peaks than traces in b) or c), though all the peaks are uniformly shifted by ~ 52 cm^{-1} to higher binding energy due to the effect of the additional argon atom. Again, the same vibrational structure is observed and the tagged spectrum clearly displays the second series of interloping peaks. We can conclude that the Ar atom does not appear to significantly perturb the structure, but more likely it further quenches the SF_6^- internal excitation. Furthermore, it also appears that heterogeneous broadening arising from vibrational hot bands does not contribute significantly to the spectrum, since the spectra change little under both source conditions, which have different characteristic ion temperatures.

The main vibrational progression observed in all the photoelectron spectra in Figure 7.5 is remarkably harmonic and has a constant spacing of 750(20) cm^{-1}. Table 7.2 lists the calculated and experimental vibrational modes for SF_6 and the calculated modes for SF_6^-. The 750 cm^{-1} progression can be confidently assigned to the a_{1g} S–F symmetric stretching mode (ν_1) in SF_6, which correlates well with the geometry changes calculated between the anion and neutral. However, the assignment of the second interloping progression is not so obvious. First,

the interloper spacing remains constant throughout the spectrum, so that we can rule out a situation where two different modes are independently contributing to the Gaussian-like progression originating from the same initial state of the anion. Furthermore, the measured 440 cm^{-1} peak spacing does not correspond to any of the fundamental frequencies in neutral SF_6. The modes which are the closest frequencies are ν_5 (524 cm^{-1}) and ν_6 (348 cm^{-1}), both do not correspond to the measured peak spacing. Thus, the second progression is not likely due to a combination band involving ν_1 and another quantum of a second vibrational mode.

A remaining possibility is that the second progression could be due to a combination/overtone band. This has been investigated in great deal in two recent theoretical studies which focus specifically on reproducing the photoelectron spectrum of SF_6^-.[26, 28] In a similar manner to that used to calculate the photoelectron spectrum of *c*-$C_4F_8^-$, Borrelli performed a straightforward Franck-Condon analysis on SF_6^-. This work suggests that the observed experimental spectrum is due to an extended progression in ν_1 (1_0^1) in conjunction with a progression from simultaneous excitation of the ν_1 mode and of the triply degenerate ν_4 mode ($1_0^n 4_0^2$). Since ν_4 is a non-totally symmetric mode, the only allowed transitions are of the type $\Delta\nu = \pm 2$ ($0 \rightarrow 2$, $0 \rightarrow 4$, etc.), however any transitions with more than two quanta in ν_1 has insufficient intensity to be experimentally observed. This analysis seemed to provide a satisfactory explanation for the experimental spectra. However, a more recent high-level theoretical study recently published has added even more complexity to this already difficult problem.

In the Franck-Condon analysis by Borrelli, the symmetry of the SF_6^- anion and neutral were both assumed to be O_h. Using high-level electronic structure calculations [RCCSD(T)/ AVQZ+d], Eisfeld concluded that though the neutral does have O_h symmetry, the anion in fact

has C_{4v} symmetry. Furthermore, the potential energy surface of the anion was shown to be strongly anharmonic which causes the anion to distorting to C_{4v} symmetry. Therefore, accurately describing the initial state of the anion is critical to reproducing the experimental photoelectron spectrum. This was done by identifying and treating the four normal modes which lead to intensity in the photoelectron spectrum. A four-dimensional potential energy surface was then calculated to directly account for the anharmonicity in the system. The computed photoelectron spectrum is a broad, unstructured Gaussian-shaped band which spans 5 eV (2.5 – 7.5 eV). This result differs significantly from both the spectrum calculated by Borrelli and the measured spectrum. The photon energy for both the measured photoelectron spectra in this Chapter was 3.5 eV, with the result that we cannot confirm or repute these new calculations with employing the new ultraviolet imaging photoelectron spectrometer in our laboratory. This may become a beginning project for a new graduate student in our group. In any event, it appears that both experimental spectra have a VDE at ~ 3 eV, but low energy electrons (0.2 eV or less) are not collected very efficiently in either apparatus. This could give rise to an artificial drop in photoelectron intensity. However, this concern could be easy tested by using higher energy photons when measuring the photoelectron spectrum. Though the new theoretical calculations shed light on the photoelectron spectrum of SF_6^-, the definitive assignments and clear understanding of the experimental spectra remains elusive.

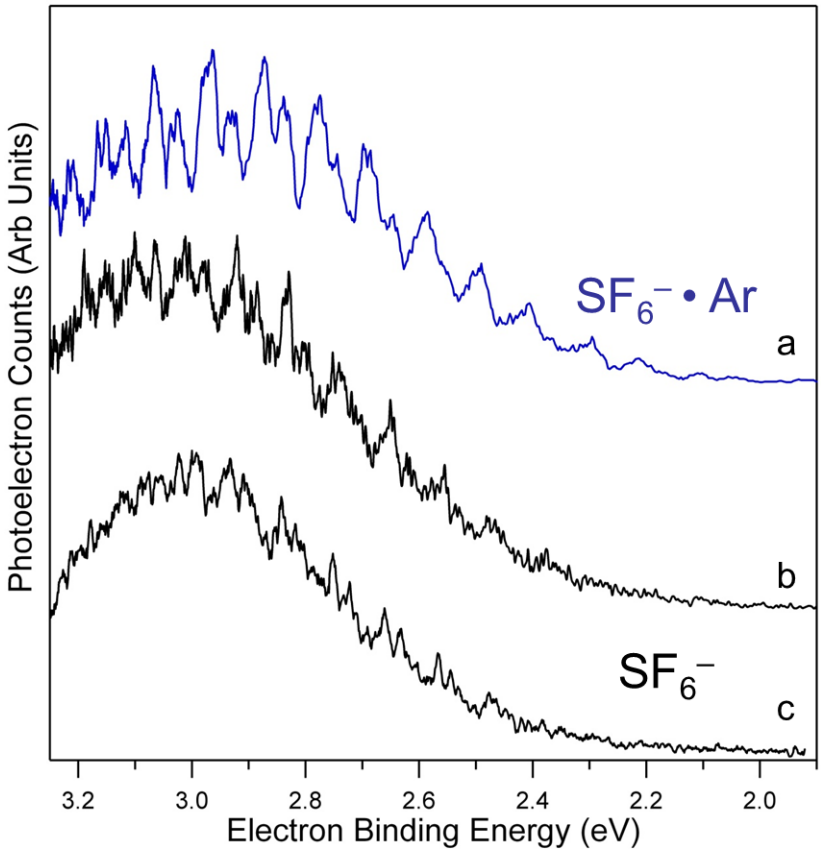

Figure 7.5 Comparison of the (c) 351 nm photoelectron spectrum of SF_6^- reproduced from Figure 7.4, and (a and c) spectra taken at Yale University using a double focusing tandem time-of-flight pulsed spectrometer. The photoelectron spectrum in trace b is of bare SF_6^- and trace a is of the SF_6^-•Ar complex.

Table 7.2 Theoretical normal mode frequencies (cm^{-1}), calculated at the MBPT(2) level of theory, for both SF_6 and SF_6^- with the corresponding experimental values for SF_6.

Vibrational Mode	SF_6			SF_6^-	
	O_h	Theory[2]	Expt.[45]	O_h	Theory[22]
ν_1	a_{1g}	779	775	a_{1g}	626
ν_2	t_g	655	643	t_g	447
ν_3	t_{1u}	965	948	t_{1u}	722
ν_4	t_{1u}	611	615	t_{1u}	306
ν_5	t_{2g}	519	524	t_{2g}	336
ν_6	t_{2u}	346	348	t_{2u}	237

From McDowell et al.[45]
From Gutsev et al.[22]

7.4 Conclusion

The photoelectron spectra of *c*-$C_4F_8^-$ and SF_6^- both exhibit extended vibrational progressions which have regular spaced peaks. Due to the large geometry change between the anion and the neutral species, the photoelectron intensity at the origin is far too small to be detected, and a direct EA cannot be measured. Our results agree with previous experimental EA determinations and provide an upper limit for the electron affinities of both *c*-C_4F_8 and SF_6. The vibrational structure in the photoelectron spectrum of *c*-C_4F_8 is primarily due to the combination bands of the two symmetric ring-breathing vibrational modes (ν_1 and ν_5). The accidental degeneracy of these two modes results in the long sequence of regularly spaced peaks in the spectrum. Understanding the underlying vibrational structure in the photoelectron spectrum of SF_6^- is more challenging. It is clear that the main progression is due to the symmetric C–F stretching mode (ν_1); the interloping regularly spaced peaks are more difficult to explain. At this

point, the Franck-Condon analysis by Borrelli, which suggests the structure originates from combination/overtone bands, appears to be the most reasonable. The high-level theoretical calculations by Eisfeld are intriguing, but the resulting predictions differ significantly from the experimental spectrum. Both these systems provide clear cases where large geometry changes between the anion and neutral molecule result in photoelectron spectra which are difficult to analyze without the assistance of high-level electronic structure calculations.

7.5 References

1. Morris, R.A., et al., *Effects of Electron and Ion Reactions on Atmospheric Lifetimes of Fully Fluorinated Compounds.* Journal of Geophysical Research, [Atmospheres], 1995. **100**(D1): p. 1287-1294.
2. Compton, R.N., et al., *Nondissociative Electron Capture in Complex Molecules and Negative-Ion Lifetimes.* Journal of Chemical Physics, 1966. **45**(12): p. 4634.
3. Dehmer, J.L., J. Siegel, and D. Dill, *Shape Resonances in E-SF_6 Scattering.* Journal of Chemical Physics, 1978. **69**(11): p. 5205-5206.
4. Field, D., N.C. Jones, and J.P. Ziesel, *Cold electron scattering in SF_6 and C_6F_6: Bound and virtual state channels.* Physical Review A, 2004. **69**(5): p. 057216.
5. Ferch, J., W. Raith, and K. Schroder, *Total Cross-Section Measurement for E-Sf_6 Scattering down to 0.036 Ev.* Journal of Physics B: Atomic, Molecular and Optical Physics, 1982. **15**(5): p. L175-L178.
6. Christophorou, L.G. and J.K. Olthoff, *Electron interactions with SF_6.* Journal of Physical and Chemical Reference Data, 2000. **29**(3): p. 267-330.
7. Christophorou, L.G. and J.K. Olthoff, *Electron interactions with c-C_4F_8.* Journal of Physical and Chemical Reference Data, 2001. **30**(2): p. 449-473.
8. Miller, T.M., J.F. Friedman, and A.A. Viggiano, *Electron attachment and detachment and the electron affinity of cyclo-C_4F_8.* Journal of Chemical Physics, 2004. **120**(15): p. 7024-7028.
9. Braum, M., et al., *IR photon enhanced dissociative electron attachment to SF_6: Dependence on photon, vibrational, and electron energy.* Journal of Chemical Physics, 2006.
10. Gianturco, F.A. and R.R. Lucchese, *Electron scattering from gaseous SF_6: Comparing calculations with experiments.* Journal of Chemical Physics, 2001. **114**(8): p. 3429-3439.
11. Chen, E.C.M., et al., *The Negative-Ion States of Sulfur-Hexafluoride.* Journal of Chemical Physics, 1988. **88**(8): p. 4711-4719.
12. Babcock, L.M. and G.E. Streit, *Ion-Molecule Reactions of SF_6 - Determination of Ip(SF_5), Ap(SF_5+-SF_6), and D(SF_5-F).* Journal of Chemical Physics, 1981. **74**(10): p. 5700-5706.
13. Compton, R.N., P.W. Reinhardt, and C.D. Cooper, *Collisional Ionization between Fast Alkali Atoms and Selected Hexafluoride Molecules.* Journal of Chemical Physics, 1978. **68**(5): p. 2023-2036.
14. Christophorou, L.G., *Electron-Molecule interactions and their applications* 1984, New York: Ed.; Academic.

15. Mock, R.S. and E.P. Grimsrud, *Electron Photodetachment of the Molecular Anions of SF_6 and Several Perfluorinated Hydrocarbons.* Chemical Physics Letters, 1991. **184**(1-3): p. 99-101.

16. Hay, P.J., *The Relative Energies of SF_6- and SF_6 as a Function of Geometry.* Journal of Chemical Physics, 1982. **76**(1): p. 502-504.

17. Streit, G.E., *Gas-Phase Reactions of O^- and O_2^- with a Variety of Halogenated Compounds.* Journal of Physical Chemistry, 1982. **86**(13): p. 2321-2324.

18. Lifshitz, C., T.O. Tiernan, and B.M. Hughes, *Electron Affinities from Endothermic Negative-Ion Charge-Transfer Reactions .4. SF_6, Selected Fluorocarbons and Other Polyatomic-Molecules.* Journal of Chemical Physics, 1973. **59**(6): p. 3182-3192.

19. Datskos, P.G., J.G. Carter, and L.G. Christophorou, *Photodetachment of SF_6-.* Chemical Physics Letters, 1995. **239**(1-3): p. 38-43.

20. Klobukowski, M., et al., *Towards Hf Scf Value of Electron-Affinity of SF_6.* Journal of Chemical Physics, 1987. **86**(3): p. 1637-1638.

21. Mcdowell, R.S. and B.J. Krohn, *Vibrational Levels and Anharmonicity in SF_6 .2. Anharmonic and Potential Constants.* Spectrochimica Acta, Part A: Molecular Spectroscopy, 1986. **42**(2-3): p. 371-385.

22. Gutsev, G.L. and R.J. Bartlett, *Adiabatic electron affinities of PF_5 and SF_6: a coupled-cluster study.* Molecular Physics, 1998. **94**(1): p. 121-125.

23. Drzaic, P.S. and J.I. Brauman, *Electron Photodetachment Study of Sulfur-Hexafluoride Anion - Comments on the Structure of SF_6-.* Journal of the American Chemical Society, 1982. **104**(1): p. 13-19.

24. Lugez, C.L., et al., *Experimental and ab initio study of the infrared spectra of ionic species derived from SF_6 and SF_4 and trapped in solid neon.* Journal of Chemical Physics, 1998. **108**(23): p. 9639-9650.

25. Frisch, M.J., et al., *Gaussian 03, Revision B.05*2003, Pittsburgh: Gaussian, Inc.

26. Borrelli, R., *Franck-Condon analysis of the SF_6^- electron photodetachment spectrum.* Chemical Physics Letters, 2007. **445**(4-6): p. 84-88.

27. Brinkmann, N.R. and H.F. Schaefer, *The SF_6^- enigma for density functional theory: is the KMLYP functional a reasonable solution for this problematic anion?* Chemical Physics Letters, 2003. **381**(1-2): p. 123-128.

28. Eisfeld, W., *Highly accurate determination of the electron affinity of SF_6 and analysis of structure and photodetachment spectrum of SF_6.* Journal of Chemical Physics, 2011. **134**(5).

29. Gutsev, G.L. and T. Ziegler, *Theoretical-Study on Neutral and Anionic Halocarbynes and Halocarbenes.* J. Phys. Chem., 1991. **95**(19): p. 7220-7228.

30. Bopp, J.C., et al., *Spectroscopic characterization of the isolated SF_6^- and $C_4F_8^-$ anions: Observation of very long harmonic progressions in symmetric deformation modes upon photodetachment.* Journal of Physical Chemistry A, 2007. **111**(7): p. 1214-1221.

31. Fischer, G., R.L. Purchase, and D.M. Smith, *The ring-puckering motion in perfluorocyclobutane.* Journal of Molecular Structure, 1997. **405**(2-3): p. 159-167.

32. Bauman, R.P. and B.J. Bulkin, *Spectra and Structure of Perfluorocyclobutane.* Journal of Chemical Physics, 1966. **45**(2): p. 496.

33. Mao, C., C.S. Nie, and Z.Y. Zhu, *Normal Coordinate Analyses of C4-C6 Perfluorocycloparaffins.* Spectrochimica Acta, Part A: Molecular Spectroscopy, 1988. **44**(11): p. 1093-1098.

34. Beagley, B., et al., *The Molecular-Structure of Perfluoro-Thiirane in the Presence of Perfluoro-Cyclobutane - a Gas-Phase Electron-Diffraction Study.* Journal of Molecular Structure, 1987. **158**: p. 309-314.

35. Chang, C.H., R.F. Porter, and S.H. Bauer, *Molecular Structures of Perfluorocyclobutane and Perfluorocyclobutene, Determined by Electron Diffraction.* Journal of Molecular Structure, 1971. **7**(1-2): p. 89.

36. Lemaire, H.P. and R.L. Livingston, *The Molecular Structures of Octafluorocyclobutane and of Methylcyclobutane.* Journal of the American Chemical Society, 1952. **74**: p. 5732.

37. Miller, F.A. and R.J. Capwell, *Infrared and Raman Spectra of Octachloroxycyclobutane, Octafluoroxycyclobutane, and Octahydroxycyclobutane.* Spectrochimica Acta, Part A: Molecular Spectroscopy, 1971. **A 27**(7): p. 1113.

38. Blake, T.A., et al., *High-resolution infrared Spectroscopy in the 1200-1300 cm-1 region and accurate theoretical estimates for the structure and ring-puckering barrier of perfluorocyclobutane.* Journal of Physical Chemistry A, 2007. **111**(44): p. 11328-11341.

39. ElSohly, A.M., et al., *Computational and ESR studies of electron attachment to decafluorocyclopentane, octafluorocyclobutane, and hexafluorocyclopropane: Electron affinities of the molecules and the structures of their stable negative ions as determined from C-13 and F-19 hyperfine coupling constants.* Journal of the American Chemical Society, 2005. **127**(30): p. 10573-10583.

40. Gallup, G.A., *The structures of c-C_4F_8 and c-$C_4F_{8^-}$ and the adiabatic electron affinity of c-C_4F_8.* Chemical Physics Letters, 2004. **399**(1-3): p. 206-209.

41. Hiraoka, K., et al., *Gas-phase ion/molecule reactions in octafluorocyclobutane.* Journal of Chemical Physics, 2002. **116**(17): p. 7574-7582.

42. Borrelli, R. and A. Peluso, *The electron photodetachment spectrum of c-$C_4F_8^-$: A test case for the computation of Franck-Condon factors of highly flexible molecules.* J. Chem. Phys., 2008. **128**(4).

43. Grimsrud, E.P., S. Chowdhury, and P. Kebarle, *Electron-Affinity of SF_6 and Perfluoromethylcyclohexane - the Unusual Kinetics of Electron-Transfer Reactions a-+B=a+B-, Where a=SF_6 or Perfluorinated Cyclo-Alkanes.* Journal of Chemical Physics, 1985. **83**(3): p. 1059-1068.

44. Johnson, M.A. and W.C. Lineberger, *Pulsed Methods for Cluster Ion Spectroscopy*, in *Techniques for the Study of Ion Molecule Reactions*, J.M. Farrar and J.W. Saunders, Editors. 1988, Wiley: New York. p. 591-635.

45. Mcdowell, R.S., et al., *Vibrational Levels and Anharmonicity in SF_6 .1. Vibrational Band Analysis.* Spectrochimica Acta, Part A: Molecular Spectroscopy, 1986. **42**(2-3): p. 351-369.

8 Bibliography

Aberth, W. (1986). "High mass analysis capability of a Wien spectrometer." International Journal of Mass Spectrometry and Ion Processes **68**(1-2): 209-212.

Adamo, C., R. Subra, A. Di Matteo and V. Barone (1998). "Structure and magnetic properties of benzyl, anilino, and phenoxyl radicals by density functional computations." Journal of Chemical Physics **109**(23): 10244-10254.

Andersen, T., H. K. Haugen and H. Hotop (1999). "Binding energies in atomic negative ions: III." Journal of Physical and Chemical Reference Data **28**(6): 1511-1533.

Andrews, L. (1968). "Infrared Spectrum of Dichlorocarbene in Solid Argon." J. Chem. Phys. **48**(3): 979-&.

Axworthy, A. E., V. H. Dayan and G. B. Martin (1978). "Reactions of fuel-nitrogen compounds under conditions of inert pyrolysis." Fuel **57**(1): 29-35.

Babcock, L. M. and G. E. Streit (1981). "Ion-Molecule Reactions of SF_6^- Determination of Ip(SF_5), Ap(SF_5+-SF_6), and D(SF_5-F)." Journal of Chemical Physics **74**(10): 5700-5706.

Barckholtz, C., T. A. Barckholtz and C. M. Hadad (1999). "C-H and N-H bond dissociation energies of small aromatic hydrocarbons." J. Am. Chem. Soc. **121**(3): 491.

Barden, C. J. and H. F. Schaefer (2000). "The singlet-triplet separation in dichlorocarbene: A surprising difference between theory and experiment." J. Chem. Phys. **112**(15): 6515-6516.

Bartmess, J. E., J. A. Scott and R. T. McIver (1979). "Scale of acidities in the gas phase from methanol to phenol." Journal of the American Chemical Society **101**(20): 6046-6056.

Bauman, R. P. and B. J. Bulkin (1966). "Spectra and Structure of Perfluorocyclobutane." Journal of Chemical Physics **45**(2): 496.

Bauschlicher, C. W. (1980). "Singlet-Triplet Separation in CBr_2." J. Am. Chem. Soc. **102**(17): 5492-5493.

Beagley, B., R. Calladine, R. G. Pritchard and S. F. Taylor (1987). "The Molecular-Structure of Perfluoro-Thiirane in the Presence of Perfluoro-Cyclobutane - a Gas-Phase Electron-Diffraction Study." Journal of Molecular Structure **158**: 309-314.

Becke, A. D. (1993). "Density-functional thermochemistry. III. The role of exact exchange." Journal of Chemical Physics **98**(7): 5648-5652.

Berkowitz, J., G. B. Ellison and D. Gutman (1994). "3 methods to measure RH bond-energies." Journal of Physical Chemistry **98**(11): 2744-2765.

Bierbaum, V. M. (2003). Theory and Ion Chemistry. Encyclopedia of Mass Spectrometry. M. L. Gross and R. Caprioli. Amsterdam, Elsevier. **1:** 276.

Blake, T. A., E. A. Glendening, R. L. Sams, S. W. Sharpe and S. S. Xantheas (2007). "High-resolution infrared Spectroscopy in the 1200-1300 cm-1 region and accurate theoretical estimates for the structure and ring-puckering barrier of perfluorocyclobutane." Journal of Physical Chemistry A **111**(44): 11328-11341.

Blondel, C., P. Cacciani, C. Delsart and R. Trainham (1989). "High Resolution Determination of the Electron Affinity of Fluorine and Bromine using Crossed Ion and Laser Beams." Phys. Rev. A **40**: 3698.

Bondybey, V. E. (1977). "Emission and Excitation-Spectra of Ccl2 in Solid Argon." J. Mol. Spec. **64**(2): 180-183.

Bondybey, V. E. and J. H. English (1980). "Laser Excitation-Spectra and Lifetimes of CBrCl and CBr_2 in Solid Ar." J. Mol. Spec. **79**(2): 416-423.

Bopp, J. C., J. R. Roscioli, et al. (2007). "Spectroscopic characterization of the isolated SF_6^- and $C_4F_8^-$ anions: Observation of very long harmonic progressions in symmetric deformation modes upon photodetachment." Journal of Physical Chemistry A **111**(7): 1214-1221.

Borden, W. T., Ed. (1982). Diradicals. New York, Wiley.

Born, M., S. Ingemann and N. M. M. Nibbering (2000). "Thermochemical properties of halogen-substituted methanes, methyl radicals, and carbenes in the gas phase." Int. J. Mass Spectrom. **194**(2-3): 103.

Borrelli, R. (2007). "Franck-Condon analysis of the SF_6^- electron photodetachment spectrum." Chemical Physics Letters **445**(4-6): 84-88.

Borrelli, R. and A. Peluso (2006). "The vibrational progressions of the N -> V electronic transition of ethylene: A test case for the computation of Franck-Condon factors of highly flexible photoexcited molecules." J. Chem. Phys. **125**(19).

Borrelli, R. and A. Peluso (2008). "The electron photodetachment spectrum of c-$C_4F_8^-$: A test case for the computation of Franck-Condon factors of highly flexible molecules." J. Chem. Phys. **128**(4).

Braum, M., F. Gruber, et al. (2006). "IR photon enhanced dissociative electron attachment to SF_6: Dependence on photon, vibrational, and electron energy." Journal of Chemical Physics

Brauman, J. I. and L. K. Blair (1970). "Gas-phase acidities of alcohols." Journal of the American Chemical Society **92**(20): 5986

Brehm, B., M. A. Gusinow and J. L. Hall (1967). "Electron affinity of helium via laser photodetachment of its negative ion." Physical Review Letters **19**(13): 737.

Brinkmann, N. R. and H. F. Schaefer (2003). "The SF_6^- enigma for density functional theory: is the KMLYP functional a reasonable solution for this problematic anion?" Chemical Physics Letters **381**(1-2): 123-128.

Carl Lineberger, W. and W. Thatcher Borden (2011). "The synergy between qualitative theory, quantitative calculations, and direct experiments in understanding, calculating, and measuring the energy differences between the lowest singlet and triplet states of organic diradicals." Physical Chemistry Chemical Physics **13**(25): 11792-11813.

Carter, E. A. and W. A. Goddard (1986). "Relation between Singlet Triplet Gaps and Bond-Energies." J. Phys. Chem. **90**(6): 998-1001.

Carter, E. A. and W. A. Goddard (1987). "New Predictions for Singlet Triplet Gaps of Substituted Carbenes." J. Phys. Chem. **91**(18): 4651-4652.

Carter, E. A. and W. A. Goddard (1988). "Correlation-Consistent Singlet Triplet Gaps in Substituted Carbenes." J. Chem. Phys. **88**(3): 1752-1763.

Chang, C. H., R. F. Porter and S. H. Bauer (1971). "Molecular Structures of Perfluorocyclobutane and Perfluorocyclobutene, Determined by Electron Diffraction." Journal of Molecular Structure **7**(1-2): 89.

Chau, F. T., D. K. W. Mok, E. P. F. Lee and J. M. Dyke (2005). "The singlet-triplet separation in CF_2: State-of-the-art ab initio calculations and Franck-Condon simulations including anharmonicity." ChemPhysChem **6**(10): 2037-2045.

Chen, E. C. M., L. R. Shuie, E. D. Dsa, C. F. Batten and W. E. Wentworth (1988). "The Negative-Ion States of Sulfur-Hexafluoride." Journal of Chemical Physics **88**(8): 4711-4719.

Chen, P., Ed. (1994). Unimolecular and Bimolecular Ion-Molecule Reaction Dynamics. Chichester, Wiley & Sons

Choe, J. I., S. R. Tanner and M. D. Harmony (1989). "Laser-Excitation Spectrum and Structure of CCl_2 in a Free-Jet Expansion from a Heated Nozzle." J. Mol. Spec. **138**(2): 319-331.

Christophorou, L. G. (1984). Electron-Molecule interactions and their applications. New York, Ed.; Academic.

Christophorou, L. G. and J. K. Olthoff (2000). "Electron interactions with SF_6." Journal of Physical and Chemical Reference Data **29**(3): 267-330.

Christophorou, L. G. and J. K. Olthoff (2001). "Electron interactions with c-C_4F_8." Journal of Physical and Chemical Reference Data **30**(2): 449-473.

Clouthier, D. J. and J. Karolczak (1989). "Pyrolysis Jet Spectroscopy - Rotationally Resolved Electronic-Spectrum of Dichlorocarbene." J. Phys. Chem. **93**(22): 7542-7544.

Clouthier, D. J. and J. Karolczak (1991). "A Pyrolysis Jet Spectroscopic Study of the Rotationally Resolved Electronic-Spectrum of Dichlorocarbene." J. Chem. Phys. **94**(1): 1-10.

Compton, R. N., Christop.Lg, G. S. Hurst and Reinhard.Pw (1966). "Nondissociative Electron Capture in Complex Molecules and Negative-Ion Lifetimes." Journal of Chemical Physics **45**(12): 4634.

Compton, R. N., P. W. Reinhardt and C. D. Cooper (1978). "Collisional Ionization between Fast Alkali Atoms and Selected Hexafluoride Molecules." Journal of Chemical Physics **68**(5): 2023-2036.

Continetti, R. E. (2001). "Coincidence Spectroscopy." Annual Review of Physical Chemistry **52**(1): 165-192.

Cooper, J. and R. N. Zare (1968). "Angular Distribution Of Photoelectrons." J. Chem. Phys. **48**(2): 942.

Datskos, P. G., J. G. Carter and L. G. Christophorou (1995). "Photodetachment of SF_6^-." Chemical Physics Letters **239**(1-3): 38-43.

Davico, G. E., V. M. Bierbaum, C. H. DePuy, G. B. Ellison and R. R. Squires (1995). "The C-H bond-energy of benzene." Journal of the American Chemical Society **117**(9): 2590-2599.

Dehmer, J. L., J. Siegel and D. Dill (1978). "Shape Resonances in E-SF_6 Scattering." Journal of Chemical Physics **69**(11): 5205-5206.

DePuy, C. H., V. M. Bierbaum and R. Damrauer (1984). "Relative gas-phase acidities of the alkanes." Journal of the American Chemical Society **106**(14): 4051-4053.

DePuy, C. H., S. R. Kass and G. P. Bean (1988). "Formation and Reactions of Heteroaromatic Anions in the Gas-Phase." J. Org. Chem. **53**(19): 4427.

Doughty, A. and J. C. Mackie (1994). "Kinetics of thermal-decompotion of the diazines – shock-tube pyrolysis of pyrimidine." Journal of the Chemical Society-Faraday Transactions **90**(4): 541-548.

Drake, S. A., J. M. Standard and R. W. Quandt (2002). "An ab initio investigation of the ground and excited electronic state properties of a series of bromine- and iodine-containing singlet carbenes." J. Phys. Chem. A **106**(7): 1357-1364.

Drzaic, P. S. and J. I. Brauman (1982). "Electron Photodetachment Study of Sulfur-Hexafluoride Anion - Comments on the Structure of SF_6^-." Journal of the American Chemical Society **104**(1): 13-19.

Drzaic, P. S. and J. I. Brauman (1984). "Electron photodetachment from phenylnitrene, anilide, and benzyl anions - Electron-affinities of the anilino and benzyl radicals and phenylnitrene." Journal of Physical Chemistry **88**(22): 5285-5290.

Dunning, T. H. (1989). "Gaussian-basis sets for use in correlated molecular calculations. 1. The atoms boron through neon and hydrogen." Journal of Chemical Physics **90**(2): 1007-1023.

Duschinsky, F. (1937). "The importance of the electron spectrum in multi atomic molecules. concerning the Franck-Condon principle." Acta Physicochimica Urss **7**(4): 551-566.

Dyke, J. M., E. P. F. Lee, D. K. W. Mok and F. T. Chau (2005). "A combined ab initio/Franck-Condon study of the A-X single-vibronic-level emission spectrum of CCl_2 and the photodetachment spectrum of CCl." ChemPhysChem **6**(10): 2046-2059.

Eisfeld, W. (2011). "Highly accurate determination of the electron affinity of SF_6 and analysis of structure and photodetachment spectrum of SF_6." Journal of Chemical Physics **134**(5).

Ellis, A. M., M. Feher and T. G. Wright (2005). Electronic and Photoelectron Spectroscopy. Cambridge, Cambridge University Press.

Ellison, G. B., G. E. Davico, V. M. Bierbaum and C. H. DePuy (1996). "Thermochemistry of the benzyl and allyl radicals and ions." International Journal of Mass Spectrometry and Ion Processes **156**(1-2): 109-131.

ElSohly, A. M., G. S. Tschumper, R. A. Crocombe, J. T. Wang and F. Williams (2005). "Computational and ESR studies of electron attachment to decafluorocyclopentane, octafluorocyclobutane, and hexafluorocyclopropane: Electron affinities of the molecules

and the structures of their stable negative ions as determined from C-13 and F-19 hyperfine coupling constants." Journal of the American Chemical Society **127**(30): 10573-10583.

Ervin, K. M. (2008). PESCAL, Fortran program.

Ervin, K. M. (2010). "PESCAL, Fortran program." PESCAL, Fortran program.

Ervin, K. M., W. Anusiewicz, P. Skurski, J. Simons and W. C. Lineberger (2003). "The Only Stable State of O_2^- Is the X $^2\Pi_g$ Ground State and It (Still!) Has an Adiabatic Electron Detachment Energy of 0.45 eV." J. Phys. Chem. A **107**(41): 8521.

Ervin, K. M. and V. F. DeTuro (2002). "Anchoring the gas-phase acidity scale." Journal of Physical Chemistry A **106**(42): 9947-9956.

Ervin, K. M., J. Ho and W. C. Lineberger (1988). "Electronic and vibrational structure of transition metal trimers: photoelectron spectra of Ni_3^-, Pd_3^-, and Pt_3^-." Journal of Chemical Physics **89**(8): 4514-4521.

Ervin, K. M., J. Ho and W. C. Lineberger (1988). "Ultraviolet Photoelectron-Spectrum of No2." J. Phys. Chem. **92**(19): 5405-5412.

Ervin, K. M., J. Ho and W. C. Lineberger (1989). "A Study of the Singlet and Triplet-States of Vinylidene by Photoelectron-Spectroscopy of $H_2C=C^-$, $D_2C=C^-$, and $HDC=C^-$ - Vinylidene Acetylene Isomerization." J. Chem. Phys. **91**(10): 5974-5992.

Ervin, K. M. and W. C. Lineberger (1992). Advances in Gas Phase Ion Chemistry. Advances in Gas Phase Ion Chemistry. N. G. Adams and L. M. Babcock. Greenwich, JAI. **1:** 121.

Ervin, K. M., T. M. Ramond, et al. (2001). "Naphthyl radical: Negative ion photoelectron spectroscopy, Franck-Condon simulation, and thermochemistry." J. Phys. Chem. A **105**(48): 10822.

Eyet, N., S. M. Villano and V. M. Bierbaum (2009). "Anchoring the gas-phase acidity scale: From formic acid to methanethiol." International Journal of Mass Spectrometry **283**(1-3): 26-29.

Fehsenfe.Fc, K. M. Evenson and H. P. Broida (1965). "Microwave discharge cavities operating at 2450 MHz." Review of Scientific Instruments **36**(3): 294

Feigerle, C. S. (1983). Ph.D. Thesis, University of Colorado.

Ferch, J., W. Raith and K. Schroder (1982). "Total Cross-Section Measurement for E-SF_6 Scattering down to 0.036 Ev." Journal of Physics B: Atomic, Molecular and Optical Physics **15**(5): L175-L178.

Field, D., N. C. Jones and J. P. Ziesel (2004). "Cold electron scattering in SF_6 and C_6F_6: Bound and virtual state channels." Physical Review A **69**(5): 057216.

FinlaysonPitts, B. J. and J. N. Pitts (1997). "Tropospheric air pollution: Ozone, airborne toxics, polycyclic aromatic hydrocarbons, and particles." Science **276**(5315): 1045-1052.

Fischer, G., R. L. Purchase and D. M. Smith (1997). "The ring-puckering motion in perfluorocyclobutane." Journal of Molecular Structure **405**(2-3): 159-167.

Fried, L. E., M. R. Manaa, P. F. Pagoria and R. L. Simpson (2001). "Design and synthesis of energetic materials." Annual Review of Materials Research **31**(1): 291-321.

Frisch, M. J., G. W. Trucks, et al. (2003). Gaussian 03, Revision B.05. Pittsburgh, Gaussian, Inc.

Frisch, M. J., G. W. Trucks, et al. (2004). Gaussian 03, Revision B.01. Wallingford, CT, Gaussian, Inc.

Fujitake, M. and E. Hirota (1989). "The Millimeter-Wave and Submillimeter-Wave Spectrum of Dichlorocarbene CCl_2 - Electronic-Structure Estimated from the Nuclear-Quadrupole Coupling-Constants." J. Chem. Phys. **91**(6): 3426-3430.

Gallup, G. A. (2004). "The structures of c-C_4F_8 and c-$C_4F_8^-$ and the adiabatic electron affinity of c-C_4F_8." Chemical Physics Letters **399**(1-3): 206-209.

Garcia, V. M., O. Castell, M. Reguero and R. Caballol (1996). "Singlet-triplet energy gap in halogen-substituted carbenes and silylenes: A difference-dedicated configuration interaction calculation." Mol. Phys. **87**(6): 1395-1404.

Garver, J., Z. Yang, et al. (2011). "Gas Phase Reactions of 1,3,5-Triazine: Proton Transfer, Hydride Transfer, and Anionic σ-Adduct Formation." Journal of the American Society for Mass Spectrometry **22**(7): 1260-1272.

Gianola, A. J., T. Ichino, S. Kato, V. M. Bierbaum and W. C. Lineberger (2006). "Thermochemical studies of pyrazolide." J. Phys. Chem. A **110**(27): 8457.

Gianturco, F. A. and R. R. Lucchese (2001). "Electron scattering from gaseous SF_6: Comparing calculations with experiments." Journal of Chemical Physics **114**(8): 3429-3439.

Gobbi, A. and G. Frenking (1993). "The Singlet-Triplet Gap of the Halonitrenium Ions NHX^+, NX_2^+ and the Halocarbenes CHX, CX_2 (X= F, Cl, Br, I)." J. Chem. Soc.-Chem. Communications(14): 1162-1164.

Grimsrud, E. P., S. Chowdhury and P. Kebarle (1985). "Electron-Affinity of SF_6 and Perfluoromethylcyclohexane - the Unusual Kinetics of Electron-Transfer Reactions a-+B=a+B-, Where a=SF_6 or Perfluorinated Cyclo-Alkanes." Journal of Chemical Physics **83**(3): 1059-1068.

Gunion, R. F. (1995). Ultraviolet Photoelectron Spectroscopy of Molecular Anions. Doctor of Philosophy, Boulder.

Gunion, R. F., M. K. Gilles, M. L. Polak and W. C. Lineberger (1992). Int. J. Mass Spectrom. Ion Processes **117**: 601.

Gunion, R. F., M. K. Gilles, M. L. Polak and W. C. Lineberger (1992). "Ultraviolet photoelectron-spectroscopy of the phenide, benzyl and phenoxide anions, with ab initio calculations." International Journal of Mass Spectrometry and Ion Processes **117**(1-3): 601-620.

Gutsev, G. L. and R. J. Bartlett (1998). "Adiabatic electron affinities of PF_5 and SF_6: a coupled-cluster study." Molecular Physics **94**(1): 121-125.

Gutsev, G. L. and T. Ziegler (1991). "Theoretical-Study on Neutral and Anionic Halocarbynes and Halocarbenes." J. Phys. Chem. **95**(19): 7220-7228.

Hajgato, B., H. M. T. Nguyen, T. Veszpremi and M. T. Nguyen (2000). "Triplet-singlet energy gaps in iodo-carbenes (I-C-X): Remarkable discrepancy between theory and experiment." Phys. Chem. Chem. Phys. **2**(22): 5041-5045.

Halls, M. D., J. Velkovski and H. B. Schlegel (2001). "Harmonic frequency scaling factors for Hartree-Fock, S-VWN, B-LYP, B3-LYP, B3-PW91 and MP2 with the Sadlej pVTZ electric property basis set." Theoretical Chemistry Accounts **105**(6): 413-421.

Hanstorp, D., C. Bengtsson and D. J. Larson (1989). "Angular-distributions in photodetachment from O." Physical Review A **40**(2): 670-675.

Hanstorp, D. and M. Gustafsson (1992). "Determination of the Electron-Affinity of Iodine." J. Phys. B **25**(8): 1773-1783.

Hay, P. J. (1982). "The Relative Energies of SF_6^- and SF_6 as a Function of Geometry." Journal of Chemical Physics **76**(1): 502-504.

Herzberg, G. (1966). Electronic Spectra and Electronic Structure of Polyatomic Molecules. New York, Van Nostrand Reinhold.

Hiraoka, K., T. Mizuno, et al. (2002). "Gas-phase ion/molecule reactions in octafluorocyclobutane." Journal of Chemical Physics **116**(17): 7574-7582.

Ho, J. (1992). University of Colorado.

Ho, J., K. M. Ervin and W. C. Lineberger (1990). "Photoelectron-Spectroscopy of Metal Cluster Anions - Cun-, Agn-, and Aun." Journal of Chemical Physics **93**(10): 6987-7002.

Hore, N. R. and D. K. Russell (1998). "Radical pathways in the thermal decomposition of pyridine and diazines: a laser pyrolysis and semi-empirical study." Journal of the Chemical Society-Perkin Transactions 2(2): 269-275.

Ichino, T., A. J. Gianola, S. Kato, V. M. Bierbaum and W. C. Lineberger (2007). "Structure of the vinyldiazomethyl anion and energetic comparison to the cyclic isomers." Journal of Physical Chemistry A **111**(34): 8374-8383.

Ichino, T., S. W. Wren, et al. (2008). "The vibronic level structure of the cyclopentadienyl radical." Journal of Chemical Physics **129**(8).

Ivey, R. C., P. D. Schulze, T. L. Leggett and D. A. Kohl (1974). "Electron-Diffraction Study of Structure of Dibromomethylene Radical." J. Chem. Phys. **60**(8): 3174-3177.

Jennings, K. R. (1979). "Negative Ions." Philosophical Transactions of the Royal Society of London. Series A, Mathematical and Physical Sciences **293**(1400): 125-133.

Jensen, K. and E. Veje (1974). "Construction of a Wien filter heavy-ion accelerator." Nuclear Instruments & Methods **122**(3): 511-515.

Johnson, M. A. and W. C. Lineberger (1988). Pulsed Methods for Cluster Ion Spectroscopy. Techniques for the Study of Ion-Molecule Reactions. J. M. Farrar and J. W. H. Saunders. New York, Wiley. **20:** 591-635.

Johnson, M. A. and W. C. Lineberger (1988). Pulsed Methods for Cluster Ion Spectroscopy. Techniques for the Study of Ion Molecule Reactions. J. M. Farrar and J. W. Saunders. New York, Wiley**:** 591-635.

Jones, J., G. B. Bacskay, J. C. Mackie and A. Doughty (1995). "Ab-initio studies of the thermal-decomposition of azaaromatics- Free-radical versus intermolecular mechanism." Journal of the Chemical Society-Faraday Transactions **91**(11): 1587-1592.

Kelleher, D. E., W. C. Martin, et al. (1999). "The new NIST Atomic Spectra Database." Physica Scripta **T83**: 158-161.

Kemister, G., A. Pross, L. Radom and R. W. Taft (1980). "A theoretical approach to substituent effects. Examination of phenoxides and anilides as models for benzyl anions." The Journal of Organic Chemistry **45**(6): 1056-1060.

Kiefer, J. H., Q. Zhang, R. D. Kern, J. Yao and B. Jursic (1997). "Pyrolyses of aromatic azines: Pyrazine, pyrimidine, and pyridine." Journal of Physical Chemistry A **101**(38): 7061-7073.

Kikuchi, H., M. Kubo, N. Watanabe and H. Suzuki (2003). "Computational method for calculating multidimensional Franck-Condon factors: Based on Sharp-Rosenstock's method." J. Chem. Phys. **119**(2): 729.

Kikuchi, O., Y. Hondo, K. Morihashi and M. Nakayama (1988). "An ab initio molecular-orbital study of pyridyl radicals." Bulletin of the Chemical Society of Japan **61**(1): 291-292.

King, G. A., T. A. A. Oliver and M. N. R. Ashfold (2010). "Dynamical insights into (1)pi sigma* state mediated photodissociation of aniline." Journal of Chemical Physics **132**(21).

Kirmse, W. (1971). Carbene Chemistry. New York, Academic Press.

Klobukowski, M., Z. Barandiaran, L. Seijo and S. Huzinaga (1987). "Towards Hf Scf Value of Electron-Affinity of SF_6." Journal of Chemical Physics **86**(3): 1637-1638.

Kogelnik, H. and T. Li (1966). "Laser beams and resonators." Applied Optics **5**(10): 1550-&.

Lee, C. T., W. T. Yang and R. G. Parr (1988). "Development of the colle-salvetti correlation-energy formula into a functional of the electron-density." Physical Review B **37**(2): 785-789.

Lee, E. P. F., J. M. Dyke and T. G. Wright (2000). "The lowest singlet-triplet gap in CCl_2, CBr_2 and CI_2." Chem. Phys. Lett. **326**(1-2): 143-150.

Lee, J. and J. J. Grabowski (1992). "Reactions of the Atomic Oxygen Radical Anion and the Synthesis of Organic Reactive Intermediates." Chem. Rev. **92**(7): 1611.

Lemaire, H. P. and R. L. Livingston (1952). "The Molecular Structures of Octafluorocyclobutane and of Methylcyclobutane." Journal of the American Chemical Society **74**: 5732.

Leopold, D. G., K. K. Murray, A. E. S. Miller and W. C. Lineberger (1985). "Methylene: A study of the $X\,^3B_1$ and $a\,^1A_1$ states by photoelectron spectroscopy of CH_2^- and CD_2^-." J. Chem. Phys. **83**(10): 4849.

Li, Q. S., J. F. Zhao, Y. M. Xie and H. F. Schaefer (2002). "Electron affinities, molecular structures, and thermochemistry of the fluorine, chlorine and bromine substituted methyl radicals." Mol. Phys. **100**(23): 3615.

Liang, J., X. L. Kong, X. Y. Zhang and H. Y. Li (2004). "Geometries of the Halocarbene anions HCF- and CF2-: ab initio calculation and Franck-Condon analysis." J. Mol. Structure-Theochem **672**(1-3): 133-139.

Lifshitz, C., T. O. Tiernan and B. M. Hughes (1973). "Electron Affinities from Endothermic Negative-Ion Charge-Transfer Reactions .4. SF_6, Selected Fluorocarbons and Other Polyatomic-Molecules." Journal of Chemical Physics **59**(6): 3182-3192.

Liu, M. L., C. L. Lee, et al. (2003). "Dispersed fluorescence spectra of the CCl_2 (A) - (X) vibronic bands." Phys. Chem. Chem. Phys. **5**(7): 1352-1358.

Lugez, C. L., M. E. Jacox, R. A. King and H. F. Schaefer (1998). "Experimental and ab initio study of the infrared spectra of ionic species derived from SF_6 and SF_4 and trapped in solid neon." Journal of Chemical Physics **108**(23): 9639-9650.

Mabbs, R., E. R. Grumbling, K. Pichugin and A. Sanov (2009). "Photoelectron imaging: an experimental window into electronic structure." Chemical Society Reviews **38**(8): 2169-2177.

Mackie, J. C., M. B. Colket and P. F. Nelson (1990). "Shock-tube pyrolysis of pyridine." Journal of Physical Chemistry **94**(10): 4099-4106.

Mackie, J. C., M. B. Colket, P. F. Nelson and M. Esler (1991). "Shock-tube Pyrolysis of Pyrrole and Kinetic Modeling." Int. J. Chem. Kinet. **23**(8): 733.

Mao, C., C. S. Nie and Z. Y. Zhu (1988). "Normal Coordinate Analyses of C4-C6 Perfluorocycloparaffins." Spectrochimica Acta, Part A: Molecular Spectroscopy **44**(11): 1093-1098.

Martin, J. D. D. and J. W. Hepburn (1998). "Determination of bond dissociation energies by threshold ion-pair production spectroscopy: An improved D-0(HCl)." J. Chem. Phys. **109**: 8139.

Marynowski, M., W. Franzen and M. Elbatanouny (1994). "Analysis of the properties of an electrostatic triplet quadrupole lens used as an electron-beam transport device." Review of Scientific Instruments **65**(12): 3718-3723.

Mcdowell, R. S. and B. J. Krohn (1986). "Vibrational Levels and Anharmonicity in SF_6 .2. Anharmonic and Potential Constants." Spectrochimica Acta, Part A: Molecular Spectroscopy **42**(2-3): 371-385.

Mcdowell, R. S., B. J. Krohn, H. Flicker and M. C. Vasquez (1986). "Vibrational Levels and Anharmonicity in SF_6 .1. Vibrational Band Analysis." Spectrochimica Acta, Part A: Molecular Spectroscopy **42**(2-3): 351-369.

McKee, M. L. and J. Michl (2002). "A possible reinterpretation of the photoelectron spectra of CCl_2, CBr_2, and CI_2: A role for quartet isodihalocarbene or dihalocarbene radical anions?" J. Phys. Chem. A **106**(37): 8495-8497.

Meotner, M. and S. A. Kafafi (1988). "Carbon acidities of aromatic-compounds." Journal of the American Chemical Society **110**(19): 6297-6303.

Miller, F. A. and R. J. Capwell (1971). "Infrared and Raman Spectra of Octachloroxycyclobutane, Octafluoroxycyclobutane, and Octahydroxycyclobutane." Spectrochimica Acta, Part A: Molecular Spectroscopy **A 27**(7): 1113-&.

Miller, T. M., J. F. Friedman and A. A. Viggiano (2004). "Electron attachment and detachment and the electron affinity of cyclo-C_4F_8." Journal of Chemical Physics **120**(15): 7024-7028.

Mock, R. S. and E. P. Grimsrud (1991). "Electron Photodetachment of the Molecular Anions of SF_6 and Several Perfluorinated Hydrocarbons." Chemical Physics Letters **184**(1-3): 99-101.

Moore, J. H., C. C. Davis and M. A. Coplan (2003). Building Scientific Apparatus. Boulder, Westview Press.

Morris, R. A., T. M. Miller, et al. (1995). "Effects of Electron and Ion Reactions on Atmospheric Lifetimes of Fully Fluorinated Compounds." Journal of Geophysical Research, [Atmospheres] **100**(D1): 1287-1294.

Moss, R. A. and M. Jones, Eds. (1975). Carbenes. New York, Wiley.

Moss, R. A. and M. Jones, Eds. (1978). Reactive Intermediates. New York, Wiley.

Mukarakate, C., Y. Mishchenko, D. Brusse, C. Tao and S. A. Reid (2006). "Probing spin-orbit mixing and the singlet-triplet gap in dichloromethylene via K-a-sorted emission spectra." Phys. Chem. Chem. Phys. **8**(37): 4320-4326.

Muller, C. W., J. J. Newby, C. P. Liu, C. P. Rodrigo and T. S. Zwier (2010). "Duschinsky mixing between four non-totally symmetric normal coordinates in the S-1-S-0 vibronic structure of (E)-phenylvinylacetylene: a quantitative analysis." Physical Chemistry Chemical Physics **12**(10): 2331-2343.

Murray, K. K., D. G. Leopold, T. M. Miller and W. C. Lineberger (1988). "Photoelectron-Spectroscopy of the Halocarbene Anions HCF^-, $HCCI^-$, $HCBr^-$, HCI^-, CF_2^-, and CCI_2." J. Chem. Phys. **89**(9): 5442-5453.

Neumark, D. M., K. R. Lykke, T. Andersen and W. C. Lineberger (1985). "Laser photodetachment measurement of the electron-affinity of atomic oxygen." Phys. Rev. A **32**(3): 1890.

Novick, S. E., P. C. Engelking, P. L. Jones, J. H. Futrell and W. C. Lineberger (1979). "Laser Photoelectron, Photodetachment, and Photodestruction Spectra of O-3." J. Chem. Phys. **70**(6): 2652-2662.

Parker, N. W. (1988). Wien Filter Design, MicroBeam Inc.

Pohl, J. H. and A. F. Sarofim (1977). "Devolatilization and oxidation of coal nitrogen." Symposium (International) on Combustion **16**(1): 491-501.

Pople, J. A., M. Headgordon and K. Raghavachari (1987). "Quadratic Configuration-Interaction - a General Technique for Determining Electron Correlation Energies." Journal of Chemical Physics **87**(10): 5968-5975.

Ramond, T. M. (2001). Negative Ion Photoelectron Spectroscopy of Alkyl Peroxides, Alkoxides, and Group VIII Transition Metal Oxides, University of Colorado.

Rappoport, Z. Z., Ed. (2007). The Chemistry of Anilines, Part 1.

Reimers, J. R. (2001). "A practical method for the use of curvilinear coordinates in calculations of normal-mode-projected displacements and Duschinsky rotation matrices for large molecules." J. Chem. Phys. **115**(20): 9103.

Robinson, M. S., M. L. Polak, V. M. Bierbaum, C. H. Depuy and W. C. Lineberger (1995). "Experimental studies of allene, methylacetylene, and the propargyl radical- Bond-dissociation energies, gas-phase acidities, and ion-molecule chemistry." Journal of the American Chemical Society **117**(25): 6766-6778.

Russo, N., E. Sicilia and M. Toscano (1992). "Geometries, Singlet-Triplet Separations, Dipole-Moments, Ionization-Potentials, and Vibrational Frequencies in Methylene (CH_2) and Halocarbenes (CHF, CF_2, CCl_2, CBr_2, and CI_2)." J. Chem. Phys. **97**(7): 5031-5036.

Schafman, B. S. and P. G. Wenthold (2007). "Regioselectivity of pyridine deprotonation in the gas phase." Journal of Organic Chemistry **72**(5): 1645-1651.

Schlachta, R., G. Lask, A. Stangassinger and V. E. Bondybey (1991). "Laser-Induced Fluorescence Excitation Spectrum of Supersonically Cooled Bromochlorocarbene in the Gas-Phase." J. Phys. Chem. **95**(19): 7132-7134.

Schwartz, R. L., G. E. Davico, T. M. Ramond and W. C. Lineberger (1999). "Singlet-triplet splittings in CX_2 (X = F, Cl, Br, I) dihalocarbenes via negative ion photoelectron spectroscopy." J. Phys. Chem. A **103**(41): 8213-8221.

Seal, P. and S. Chakrabarti (2007). "Explicit role of dynamical and nondynamical electron correlation on singlet-triplet splitting in carbenes." Chem. Phys. **332**(2-3): 232-242.

Seliger, R. L. (1972). "E X B mass-separator design." Journal of Applied Physics **43**(5): 2352.

Sendt, K. and G. B. Bacskay (2000). "Spectroscopic constants of CF_2, CCl_2, and CBr_2 and heats of formation of selected halocarbenes: An ab initio quantum chemical study." J. Chem. Phys. **112**(5): 2227-2238.

Sharp, T. E. and H. M. Rosenstock (1964). "Franck-condon factors for polyatomic molecules." Journal of Chemical Physics **41**(11): 3453.

Smith, K. L., L. D. Smoot, T. H. Fletcher and R. J. Pugmire, Eds. (1994). The Structure and Reaction Processes of Coal. New York, Plenum Press.

Stoll, H., B. Metz and M. Dolg (2002). "Relativistic energy-consistent pseudopotentials - Recent developments." J. Comput. Chem. **23**(8): 767.

Streit, G. E. (1982). "Gas-Phase Reactions of O- and O-2- with a Variety of Halogenated Compounds." Journal of Physical Chemistry **86**(13): 2321-2324.

Surber, E., R. Mabbs and A. Sanov (2003). "Probing the Electronic Structure of Small Molecular Anions by Photoelectron Imaging†." The Journal of Physical Chemistry A **107**(40): 8215-8224.

Tao, C., C. Mukarakate and S. A. Reid (2007). "Single vibronic level emission spectroscopy of the (A)over-tilde(1)A "-> X(1)A ' system of bromochlorocarbene." J. Mol. Spec. **246**(2): 113-117.

Tarczay, G., T. A. Miller, G. Czako and A. G. Csaszar (2005). "Accurate ab initio determination of spectroscopic and thermochemical properties of mono- and dichlorocarbenes." Phys. Chem. Chem. Phys. **7**(15): 2881-2893.

Tevault, D. E. and L. Andrews (1975). "Laser-Induced Fluorescence-Spectrum of Argon Matrix-Isolated Dichlorocarbene." J. Mol. Spec. **54**(1): 110-120.

Thompson, M. A., J. P. Martin, J. P. Darr, W. C. Lineberger and R. Parson (2008). "A combined experimental/theoretical investigation of the near-infrared photodissociation of IBr-(CO2)(n)." J. Chem. Phys. **129**(22).

Tripathi, G. N. R. and R. H. Schuler (1987). "Time resolved resonance raman- Spectra of anilino radical and aniline radical cation." Journal of Chemical Physics **86**(7): 3795-3800.

Turker, L., S. Gumus and T. Atalar (2010). "A DFT Study on Nitro Derivatives of Pyridine." Journal of Energetic Materials **28**(2): 139-171.

Van Doren, J. M., S. E. Barlow, C. H. DePuy and V. M. Bierbaum (1987). "The tandem flowing afterglow-sift-drift." International Journal of Mass Spectrometry and Ion Processes **81**: 85-100.

Villano, S. M., N. Eyet, et al. (2010). "Photoelectron spectroscopy and thermochemistry of the peroxyacetate anion." European Journal of Mass Spectrometry **16**(3): 255-268.

Villano, S. M., N. Eyet, et al. (2010). "Photoelectron Spectroscopy and Thermochemistry of the Peroxyformate Anion." Journal of Physical Chemistry A **114**(1): 191-200.

Vogelhuber, K. M., S. W. Wren, A. B. McCoy, K. M. Ervin and W. C. Lineberger (2011). "Photoelectron spectra of dihalomethyl anions: Testing the limits of normal mode analysis." The Journal of Chemical Physics **134**(18): 184306-184313.

Vogelhuber, K. M., S. W. Wren, L. Sheps and W. C. Lineberger (2011). "The C-H bond dissociation energy of furan: Photoelectron spectroscopy of the furanide anion." Journal of Chemical Physics **134**(6).

Wahlin, L. (1964). "The Colutron, a zero deflection isotope separator." Nuclear Instruments & Methods **27**(1): 55-60.

Wallace, S., K. D. Bartle and D. L. Perry (1989). "Quantification of nitrogen functional groups in coal and coal derived products." Fuel **68**(11): 1450-1455.

WebBook, N. C. NIST Standard Reference Database. **Number 69**.

Wenthold, P. G., D. A. Hrovat, W. T. Borden and W. C. Lineberger (1996). "Transition-state spectroscopy of cyclooctatetraene." Science **272**(5267): 1456-1459.

Wenthold, P. G. and W. C. Lineberger (1999). "Negative ion photoelectron spectroscopy studies of organic reactive intermediates." Accts. Chem. Research **32**(7): 597-604.

Wilson, E. B., J. C. Decius and P. C. Cross (1980). Molecular Vibrations. New York, Dover.

Wong, M. W. (1996). "Vibrational frequency prediction using density functional theory." Chemical Physics Letters **256**(4-5): 391-399.

Woon, D. E. and T. H. Dunning (1993). "Gaussian-Basis Sets for Use in Correlated Molecular Calculations .3. the Atoms Aluminum through Argon." Journal of Chemical Physics **98**(2): 1358-1371.

Wren, S. W., K. M. Vogelhuber, K. M. Ervin and W. C. Lineberger (2009). "The photoelectron spectrum of CCl2-: the convergence of theory and experiment after a decade of debate." Physical Chemistry Chemical Physics **11**(23): 4745-4753.

Wren, S. W., K. M. Vogelhuber, et al. (In Preparation). "Nitrogen Proximity Effects in Azines: How Nitrogen Atoms Affect C–H Bond Strengths and Anion Stability."

Xu, H. and J. H. Kiefer (2010). "Shock Tube Study of 1,3,5-Triazine Dissociation and Relaxation and Relaxation of Pyrazine." International Journal of Chemical Kinetics **42**(4): 211-220.

Xu, S. L. and M. D. Harmony (1993). "Halocarbene Production in Free-Jet Expansions from a Hot Nozzle." Chem. Phys. Lett. **205**(6): 502-507.

Xu, S. L. and M. D. Harmony (1993). "Lif Excitation Spectrum of Dibromocarbene in a Supersonic Free-Jet Expansion." J. Phys. Chem. **97**(29): 7465-7470.

Xu, W. and A. Gao (2005). "Structures, Electron Affinities, and Harmonic Vibrational Frequencies of $C_6H_5X/C_6H_5X^-$ (X = N, S, NH, PH, CH_2, and SiH_2)." The Journal of Physical Chemistry A **110**(3): 997-1004.

Zhou, S. K., M. S. Zhan, J. L. Shi and C. X. Wang (1990). "Gas-Phase Spectrum of Dibromocarbene Studied by Laser-Induced Fluorescence." Chem. Phys. Lett. **166**(5-6): 547-550.

Zittel, P. F., G. B. Ellison, et al. (1976). "Laser photoelectron spectrometry of CH_2^-- Singlet-triplet splitting and electron-affinity of CH_2." Journal of the American Chemical Society **98**(12): 3731-3732.